

Investigation of the effect of ultrasonic cavitation in small gaps on surface properties

Von der Fakultät für Maschinenbau
der Gottfried Wilhelm Leibniz Universität Hannover
zur Erlangung des akademischen Grades
Doktor-Ingenieur
genehmigte

Dissertation

von

M.Sc. Fushi Bai

geb. am 04. Mai 1986 in Gansu

2019

1. Referent: Prof. Dr.-Ing. Jörg Wallaschek
2. Referent: Prof. Dr.-Ing. Walter Sextro
3. Referent: Prof. Dr. Matthias Becker

Tag der Promotion: 21. Januar 2019

Acknowledgement

The present thesis summarized the conclusions during my time at the Institute of Dynamics and Vibration Research (IDS) of the Leibniz University Hannover, Germany, between October 2014 and January 2019.

Time flies. I already spent four years at IDS. These four years are the most important and unforgotten journey in my life. During this period, I learned a lot, met many friends and finished my PhD thesis. Here I want to show my deep attitude to all those who helped and supported me.

My deepest gratitude goes first and foremost to my supervisor Prof. Wallaschek. I can only use the word "lucky" to express the encounter between me and him. He gave me full support to allow me to think and complete my thesis independently. Thank you for your support and help in working, studying and living in Germany. I also would like to thank Prof. Sextro and Prof. Becker, for being a part of the review committee and taking time to review my thesis. Special thanks to Prof. Bo Fu in Sichuan University. Without him I do not have an opportunity to know Prof. Wallaschek and my dear colleagues. Also, I am indebted to associate Prof. Xianglong Li in Sichuan University for supporting my PhD application.

I would like to thank all my colleague at IDS. The days of working together are happy and memorable! Thank you for your help to me all the time. I am very grateful to all the members of my "Piezo-und Ultraschalltechnologie" group. In particular, I would like to thank my group leader Dr.-Ing Jens Twiefel. I benefited from his support and valuable advices. I am also thankful to Kai for his constant guidance in experiments and the review of my draft thesis. I also thank Yangyang, Liang, Gabriel, Andreas, Micheal, Jian, Henning and so on for helping me to develop my research.

I would like to thank all my friends in Hannover. I am deeply appreciated for all of your help and memorable gathering time in these four years.

I owe my deepest gratitude to my family for their constant support and understanding to allow me to pursue my dream aboard. Special thanks to my wife Rui for all her love, support, encouragement and patience. I would also like to thank our cat for making our home warmer and sweeter.

Fushi Bai

Hannover, January 2019

Contents

List of Symbols	VI
Kurzfassung	VIII
Abstract	IX
1 Motivation	1
2 State of the art	5
2.1 Metal surface enhancement technologies	5
2.2 Peening processes	6
2.2.1 Shot peening	7
2.2.2 Shotless peening	7
2.2.3 Machine impact peening	9
2.2.4 Ultrasonic cavitation peening	9
2.3 Cavitation phenomenon and its effects on metal surfaces	11
2.3.1 Basic theory on cavitation	11
2.3.1.1 Ultrasonic cavitation near a rigid wall	12
2.3.1.2 Cavitation bubbles in a small gap	15
2.3.1.3 Primary and Secondary Bjerknes Forces	16
2.3.2 Distribution and intensity of cavitation bubbles	17
2.3.2.1 Experimental methods	17
2.3.2.2 Theoretical prediction	20
2.3.3 Cavitation on metal surfaces	23
2.3.3.1 Micro structures of modified metal surface and cavitation pits	23
2.3.3.2 Phases of cavitation erosion and incubation period	24
2.4 Development of ultrasonic cavitation peening	27
3 Research objective	32
3.1 Analysis of the state of the art	32
3.2 Aims of thesis	33
3.3 Structure of the thesis	33
4 Ultrasonic fields in thin bubbly liquid layers	35
4.1 Modeling the sound field in bubbly liquids	35

4.2	Simulation of sound field in thin bubbly liquid layers	38
4.3	Experimental determination of the cavitation distribution utilizing sono-chemiluminescence	44
4.3.1	Experiments	44
4.3.2	The mean distribution of cavitation bubbles	48
4.3.3	The local distribution of cavitation bubbles	50
5	Investigation of the impact loads caused by cavitation bubbles in small gaps	54
5.1	Numerical investigation of the bubble characteristics	54
5.1.1	Different cavitation bubble sizes in a small gap	55
5.1.2	Impacts from cavitation bubbles at different driving currents	56
5.2	Experimental investigation of surface volume change	61
5.3	Experimental investigation of the impacts on workpiece surfaces utilizing the piezoelectric effect	66
5.3.1	Experiment setup for the detection of impact signals	66
5.3.2	Impact force caused by cavitation bubbles	67
5.3.3	Impact analysis in frequency domain	72
5.3.4	Efficiency of the cavitation process	73
6	Phases of the ultrasonic cavitation process and variations of surface properties	76
6.1	Detection of the process phases by plastic deformation measurements	76
6.1.1	Experimental procedures	76
6.1.2	Micro-structure in different phases	78
6.1.3	Evaluation of different phases during ultrasonic cavitation peening	81
6.2	Investigations of the relationship between surface properties and cavitation process time	88
6.2.1	Surface topographies and roughness at different process phases	88
6.2.2	Micro-hardness at different process phases	89
7	Discussion	92
8	Conclusions and outlook	94
8.1	Conclusions	94
8.2	Outlook	95
	Appendix	97
	A Measurement of hardness	97
	Bibliography	98

List of Symbols

The used symbols and different meanings are explained in the text. Vectors and matrices are generally printed in bold.

Latin notation

a	Instantaneous bubble radius
A	Projected contact area for hardness measurement
b	Damping constant of a cavitation bubble
C_p	Parallel capacitance
c_m	Speed of sound in a bubbly liquid
c_t	Mechanical stiffness of the transducer
D_f	Gas thermal diffusivity
d	Modal damping
h_{max}	Maximum indentation depth
I_0	Potential from the surrounding bubbles
I	Driving current
K	Polytropic exponent
k_t	Complex wave number for bubble interactions
m	Mass
m_{loss}	Mass loss after treatment
P	Ambient pressure
P_i	Initial inner pressure of a bubble
P_0	Constant hydrostatic pressure
P_s	Amplitude of the acoustic sound pressure
p_{ge}	Initial gas pressure of a bubble
R	Time-dependent radius of the bubble
R_0	Initial bubble radius
R_s	Radius of the sonotrode tip
S	Slope at the tangent line of the beginning of the unloading curve
U	Driving voltage
u_0	Peak amplitude of the sound source
V_{change}	Total change of the volume
V_p	Plastic deformation volume
X	Compressibility of a bubbly liquid

Z_L Liquid load impedance

Greek notation

α Electromechanical coupling coefficient
 β Bubble volume fraction
 γ Ratio of specific heats
 μ Coefficient of viscosity
 ρ_l Density of liquid
 ρ_m Density of a bubbly liquid
 ρ_w Density of the specimen
 σ Surface tension coefficient
 σ_B Standard deviation of the cavitation bubble size distribution
 Φ Complex dimensionless parameter
 ω Angular frequency of a sound source
 ω_0 Natural frequency of a cavitation bubble
 ε Surface strain

Vector

\mathbf{r}_M Position vector of the point M in space
 \mathbf{r}'_M Position vector of the plate active element and S'

Kurzfassung

Untersuchung des Einflusses der Ultraschall-Kavitation in kleinen Spalten auf die Oberflächeneigenschaften

Die Ultraschall-Kavitation kann zur Verbesserung der Oberflächeneigenschaften von Werkstücken in industriellen Anwendungen genutzt werden. Während dieses Oberflächenveredelungsprozesses ist ein kleiner Spalt erforderlich, um hohe Stoßkräfte auf die Werkstückoberflächen zu erzeugen. Die Verteilung der Kavitationsblasen, die optimale Spaltbreite und die Prozesszeit beeinflussen die behandelten Oberflächeneigenschaften stark. In dieser Arbeit werden die Verteilung der Schallfelder in der Kavitationsflüssigkeit und die optimale Spaltbreite unter Berücksichtigung von Blasenwechselwirkungen modelliert. Danach werden Sonochemilumineszenz- und Oberflächenvolumenvariationsexperimente durchgeführt. Zusätzlich ist ein piezoelektrischer Kraftsensor zur Messung der Aufprallkräfte entwickelt worden. Schließlich wird das plastische Verformungsvolumen untersucht, um die optimale Prozesszeit genauer zu identifizieren. Die numerischen Modelle zeigen eine Übereinstimmung mit den experimentellen Ergebnissen.

Schlagwörter: Ultraschall-Kavitation, Spaltbreite, Prozesszeit, Oberflächeneigenschaften

Abstract

Ultrasonic cavitation can be used to improve surface properties of workpieces in industrial applications. During this surface enhancement process, a small gap is required to generate high impact forces on the workpiece surfaces. The distribution of cavitation bubbles, the optimal gap width and the process time highly affect the treated surface properties. In this thesis, the distribution of sound fields in the small gaps and the optimal standoff distance are simulated with the consideration of bubble interactions. Then, sonochemiluminescence and surface volume variation experiments are carried out. Additionally, a piezoelectric force sensor is designed to detect impact forces. Finally, plastic deformation volume is studied to more accurately identify the optimal process time. The simulation and experimental results show good agreements.

Key words: Ultrasonic cavitation, gap width, process time, surface properties

1 Motivation

After an automobile is manufactured, even if it is never used, rubber parts and plastic products in the automobile will gradually fail. Metal parts and components will be corroded or rust as well. If the automobile is utilized for a long time, the surfaces of metal parts that contact and move with each other, such as gears and axles, will be worn out. Sometimes fatigue breaks of those parts even occur. The failures and breaks often start from the surfaces of those parts. Thus, delaying and controlling the surface failure can improve the component performance.

Mechanical surface treatments are often used to improve the surfaces of the cyclic loaded components in the automotive and aerospace industries. After treatment, the resistance against wear, fatigue and corrosion increases due to plastic deformation of the component surfaces. The treatment methods are differentiated by whether the interaction between the tool and the workpiece is static or impulsive. The static treatment processes include rolling, spinning and stressing. The impulsive processes are divided into shot peening and shotless peening. The shots are usually round metallic, glass or ceramic particles.

Klumpp et al. [1] defined shot peening as "the process for cold working surfaces by bombarding the product with shot of solid and spherical nature propelled at a relatively high velocity". Traditional shot peening, which is widely used, is a process during which small and spherical shots are shot on the workpiece surface utilizing pneumatic, centrifugal, or vapor blast machines.

Through a shot peening treatment, the hardness and compressive residual stress on the treated surface can be effectively enhanced, resulting in the improvement of fatigue life and the prevention of failure mechanisms. Furthermore, it is possible to improve the strength and corrosion resistance of the treated surfaces. Thus, high performance of the treated metal component surface can be achieved. However, it is difficult to treat complex geometries and sometimes unacceptable surface roughness might result from the deteriorated shots.

To overcome those disadvantages, shotless peening processes have been developed recently. Laser shock peening is commonly used. It requires expensive equipment and a specially protected environment for treatment. Water jet peening is another peening process in which high velocity water droplets continuously impinge over the treated surface. However, a continuous and substantial supply of clean water is required, which leads

to high running cost. It is therefore of great interest to find other methods for shotless peening to resolve these problems.

Ultrasonic cavitation peening has been found to be a promising alternative solution. It has shown great potential to overcome some of the disadvantages of the existing peening methods [2] and it has attracted great attention in recent ten years. Ultrasonic cavitation peening is usually based on impacts caused by the collapse of cavitation bubbles in water. Compared to other peening equipment, using a piezoelectric transducer to generate cavitation has many advantages: it is easy to control, has a compact structure and a high output power. Since there are no solid objects bombarding the workpiece, the increase of surface roughness is obviously smaller compared to other conventional peening process. At the end of ultrasonic cavitation peening, water only contains metal and metal oxide, which can be easily collected and recycled. Additionally, this surface treatment process is not expensive to perform.

The most commonly used sonotrodes have flat surfaces at the end. In order to achieve high impacts on the treated surface, a large vibration amplitude is necessary, since a higher amplitude generates more energy when the sonotrode is partly immersed in a liquid. In this process, due to the high attenuation caused by cavitation bubbles, a small gap between the tip end of sonotrode and the treated surface is required, usually less than 1 mm. The gap width is named as standoff distance in this thesis. At small standoff distance, the dynamics (growths and collapses) of cavitation bubbles greatly disturb the sound field and the bubble sizes depend on the sound pressure. Apart from the dynamics of bubbles, there are interaction forces between cavitation bubbles, disturbing sound field as well. The interaction forces are defined as Bjerknes forces [3] which are introduced in Chapter 2 in detail. In order to more accurately simulate the distribution of the sound pressure in a bubbly liquid, the interactions of cavitation bubbles have to be considered. In this thesis, the sound field distribution in bubbly liquid is examined for the first time considering bubble interactions.

Furthermore, the small gaps limit the dynamics of cavitation bubbles, leading to the change of impacts on the treated surfaces compared to the collapse of bubbles near a rigid wall. When the standoff distance becomes smaller, the cavitation bubble is no longer spherical if other operation conditions are not changed. Due to this limitation, the impact amplitude on the treated surfaces is reduced. On the other hand, with a large standoff distance the sound pressure on the treated surface is small, which leads to a decrease of impact forces from the collapse of cavitation bubbles due to the high attenuation of the bubble liquid on the sound propagation. The properties of the treated surface greatly depend on the impacts caused by cavitation bubbles. Thus, it is deduced that w^* (the ratio of the standoff distance to the bubble diameter) has major influence on the ultrasonic cavitation peening results. Therefore, the optimal standoff distance can be predicted once the operation conditions (vibration amplitude, driving frequency) are determinate. The optimal standoff distance can also be validated by analyzing the variations of the impact (including the amplitude, pulse time and number).

Process time is another key parameter to improve the specimen surface properties during ultrasonic cavitation peening. At the beginning of this process, plastic deformation occurs on the metal workpiece surface. The plastic deformation means the surface volume loss without the mass loss. With the continuous impacts, cavitation erosion occurs and mass loss is produced. In this period, both the volume loss and the mass loss occur at the same time. The plastic deformation induces the compressive residual stress and prevents the cracks on the treated surface, but the erosion and the mass loss deteriorate the surface. Obviously, the plastic deformation is beneficial for mechanical surface properties instead of mass loss. Thus, it is necessary to detect an optimal process time during which much plastic deformation and only small mass loss are generated on the workpiece surface.

The cavitation bubbles lead to a slowdown of the sound propagation and can generate impacts on the treated surface. As a result, surface plastic deformation is formed due to these impacts. Besides, the characteristics of cavitation bubbles in a small gap are different from that without limitation. Therefore, two interesting phenomena about cavitation bubbles during ultrasonic cavitation peening will be paid a special attention:

- The distributions of cavitation bubbles in a small gap.
- The effects of standoff distances and processing time on treated surfaces during ultrasonic cavitation peening.

To more completely understand these two phenomena, relevant background knowledge is required and introduced in Chapter 2. In this chapter, first the different peening processes are illustrated and then the peening effects are compared. Next, the advantages of ultrasonic cavitation peening with respected to classical processes are described. Then, the background of cavitation is introduced in detail. This introduction mainly focuses on the cavitation bubbles near a rigid wall and the bubbles limited in a small gap. The sound propagation in a bubbly liquid is also introduced. Finally, the response of metal surface to the impact of cavitation bubbles is described. Through analyzing the state of the art, the key issues in this thesis are listed in Chapter 3, such as the distribution of cavitation bubbles in a small gap, the impact effects under different operation conditions, the surface micro-structure after treatment and so on.

In Chapter 4, a model of sound propagation is introduced which takes the interaction of cavitation bubbles into consideration. This is the first step to understanding the ultrasonic cavitation peening process. The model with interactions is compared with the model without interactions. Using the model with bubble interactions, the distributions of sound pressure in different conditions are calculated and plotted. In order to validate the calculated result, sonochemiluminescence (SCL) experiments were carried out. Using the comparison of the calculated results and the experimental results, the distribution of sound fields in bubbly liquid is investigated. However, the impact effects on the workpiece surface caused by the cavitation bubbles are still unknown from this model and SCL experiments.

In Chapter 5, the impact effects on the treated surface are investigated. The influences of the standoff distance on the treated surface are first investigated. To reduce the energy loss during ultrasonic cavitation peening, a small standoff distance is necessary. However, this limitation affects the peening results. The impact effects of the cavitation bubbles at different standoff distances are evaluated by the change in volume. The change in volume refers to the volume of pits that are caused by the impacts after treatment. To further study the amplitudes and impulse time of the impacts, a piezoelectric sensor was used to evaluate the variations of impact loads during ultrasonic cavitation peening. The signals are analyzed in both time and frequency domain to reveal the underlying rules.

Ultrasonic cavitation peening takes advantage of plastic deformation on the treated surface. Apart from the impact effects, process time has a significant influence on the volume of plastic deformation. In order to obtain an optimal process time, in Chapter 6 a new method is developed to evaluate the volume of plastic deformation. In this method, by analyzing the relationship between volume change and mass loss, the plastic deformation can finally be deduced. Then, the micro-structures in different stages of the cavitation erosion were observed. Lastly, the surface properties (roughness and microhardness) were measured to evaluate the optimal operation conditions during ultrasonic cavitation peening.

2 State of the art

In this chapter, the background of the main research methods and results presented in the thesis is briefly provided. As this thesis mainly deals with the effects of ultrasonic cavitation on the enhancement of metal surfaces, the commonly used metal surface enhancement technologies are introduced in Section 2.1. Since peening processes are widely used to improve manufactured parts, different peening processes are presented in detail in Section 2.2. The use of acoustic cavitation to improve metal surface properties has been developed in recent years. In Section 2.3 the dynamics of cavitation bubbles near a solid surface and in a small gap are discussed from both theoretical and engineering perspectives. The methods used to evaluate the distribution of cavitation bubbles and the impact caused by the collapse of cavitation bubbles are also introduced. By repetitive impacts on the workpiece surface, the surface properties can be improved. The improvement process of the surface properties by the impacts is briefly explained. Finally, the development of the surface enhancement technology using ultrasonic cavitation is described.

2.1 Metal surface enhancement technologies

Surface enhancement technologies (SET) are necessary to improve the surfaces of components which suffer from heavy cyclic loads in industrial applications. It is because that the detrimental effects of metal component surfaces can occur after turning, milling, drilling or welding, especially for the highly stressed components [4]. Through SET, a layer of residual compressive stress can be induced to prevent failure in metallic materials, and mechanical properties of metals can be modified. Figure 2.1 shows the mechanism behind the mechanical surface enhancement technologies [5].

When the material surface is impacted by high pressure, plastic deformation occurs in the contacted region. Thus, the compression pressure occurs around the deformation region, leading to the generation of the compressive stresses in the impact region. Since the first surface enhancement process, the sand blast process that has been proposed in 1871, a great variety of metal surface enhancement processes have been developed and utilized in industrial applications. An overview of mechanical metal surface treatment is given in Table 2.1. According to the relative movement between the manufacturing tool and the specimen, the surface enhancement technologies can be divided into two groups.

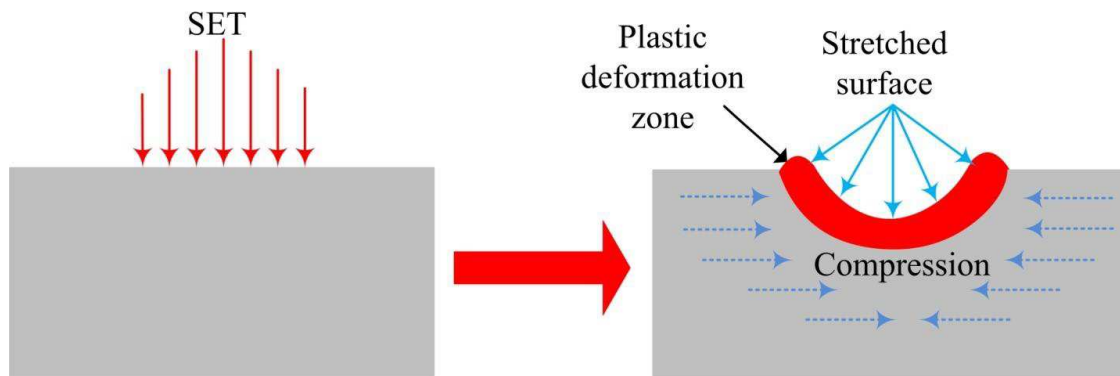


Figure 2.1: Mechanism of surface enhancement methods [5].

Tool mean something that acts directly on the workpiece surface and causes deformation. The processes without relative movement include embossing process, peening process while the processes with relative movement include rolling, spinning, fretting and so on. The process can also be divided by whether the tool contact is static or impulsive. The processes with impulsive tool contact mainly refer to peening processes.

Table 2.1: Processes of mechanical metal surface treatments [1].

		Plastic deformation without relative movement between workpiece and tool	Plastic deformation with relative movement between workpiece and tool			
			Rolling		Sliding	
					Solid tool	Liquid tool
Static		Embossing	Deep rolling, finish rolling, size rolling	Spinning, diamond finishing	Autofretting, stressing	
	Regular	Machine hammer peening, laser shock treatment, high pressure water peening				
Impulsive	Irregular	Shot peening, variants of shot peening				

Among the mechanical surface treatment processes, peening processes are widely used in industrial applications due to their conveniences and the favorable effects [6]. The peening processes can be divided by shot peening, shotless peening and mechanical hammer peening. They all have advantages and disadvantages and will be described in the following.

2.2 Peening processes

Peening processes are cold working processes and can be divided into three types depending on different ways to generate impact forces: shot peening, shotless peening and

machine impact peening. Shot peening and mechanical hammer peening are used for industrial applications due to easy operation and inexpensiveness. However, the surface deterioration and the high surface roughness are produced after shot peening treatment. In recent years, the shotless peening has been developed to overcome this disadvantage.

2.2.1 Shot peening

Conventional shot peening

The most commonly used mechanical SET is shot peening. During the process the small and spherical shots are shot out from a nozzle using pneumatic, centrifugal, or vapor blast machines. As shown in figure 2.2 (a), a high speed shot stream impacts on the metal surface to generate plastic deformation. The impact produces a dimple on the material surface, its depth is in the range of 0.5 mm to 3 mm. This method not only improves the properties of peened components but also causes less material removal compared to other conventional processes, such as fretting. However, it is difficult to use to treat complex geometries and unacceptable surface roughness is often caused by deteriorated shots [7].

Ultrasonic shot peening

A typical setup of ultrasonic shot peening is shown in figure 2.2 (b). During this process, the tip of the sonotrode vibrates with high frequency and displacement and propels the shots to the sample surface with high speed [8]. The shots move towards the surface of the sample with different incident angles due to the shot collision with each other. Therefore, the directions and speed of the shots are random. As a result, the surface of the sample is treated uniformly. Compared to the conventional peening process, higher residual compressive stress is produced by ultrasonic shot peening due to the high speed of the shots. Additionally, nanometer sized grains are obtained on the surface layer. The dense grains change the micro-structure of the material, resulting in an increase in the surface hardness of the material.

2.2.2 Shotless peening

Laser shock peening

Figure 2.2 (d) shows the mechanism of laser shock peening. During this process an opaque layer is placed on the workpiece surface. On this opaque layer there is a layer of water. The surface of the opaque layer is hit by a high-energy laser beam, which generates plasma on the surface. This plasma causes a high amplitude shock wave which propagates towards the workpiece, generating a plastic deformation layer on the workpiece. The thicker the plastic deformation layer, the deeper the residual compressive pressure. Thus, different thicknesses of the plastic deformation layers result in different depths of

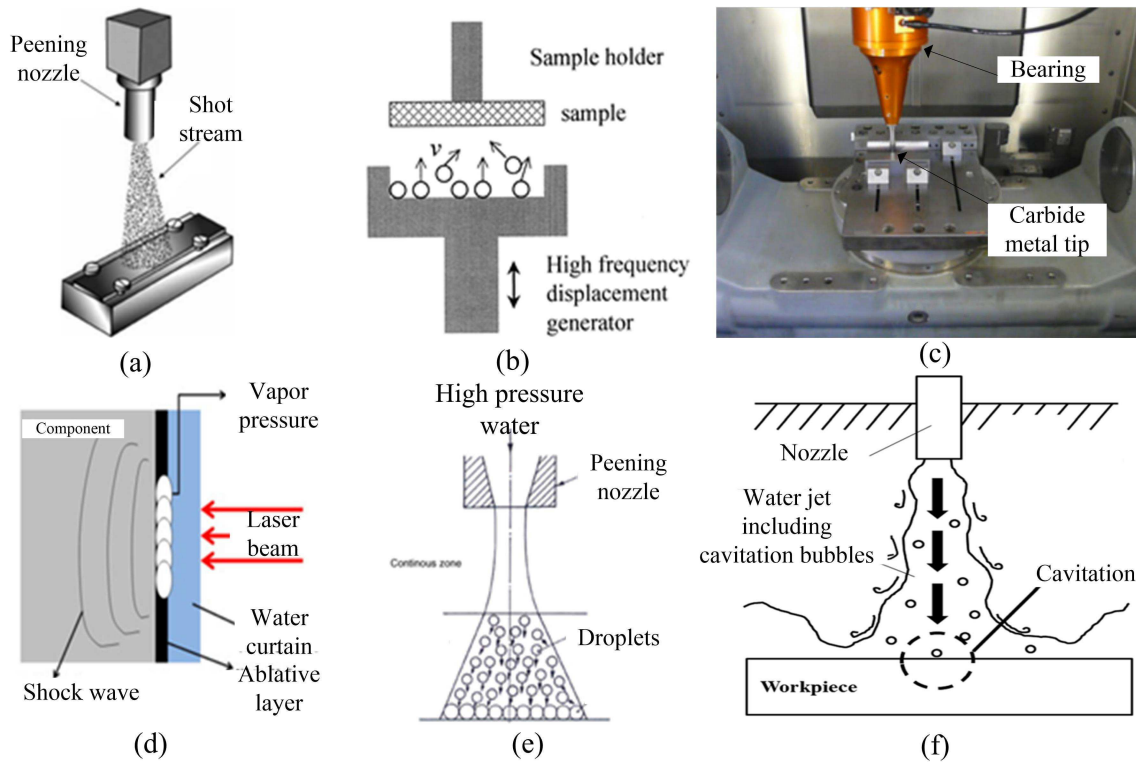


Figure 2.2: (a) Conventional shot peening [7]; (b) Ultrasonic shot peening [8]; (c) Machine hammer peening [9]; (c) Laser shock peening [10]; (d) Water jet peening [11]; (e) Water cavitation jet peening [12]

the residual stress. The depth of the residual stress can be measured by X-Ray method and the results show that the depth of the residual stresses after laser peening is more than that after shot peening. The drawbacks of laser shock peening are the requirements of the special protected environment and expensive equipment for treatment. Further, skilled operators are required during the whole process. Additionally, this process results in high surface roughness and may have thermal effects due to direct ablation [10].

Water jet peening

As shown in figure 2.2 (e), water jet goes through a peening nozzle with high speed. When the water jet is close to the workpiece, the jet disperses and forms many droplets. Therefore, the metal surface is continually impinged by the droplets with a high velocity [13]. The high impacts caused by the droplets leads to local plastic deformation on the workpiece surface. When the peening process is completed, the compressive residual stress is generated on the surface without much modification of the surface roughness. Compared to shot peening, water jet peening is relatively easy to operate because the speed of the water jet can be controlled. Although this process simplifies the procedures and can treat the entire surface uniformly, high pressure is required to insure that the droplets impact the surface with a high velocity.

Water cavitation jet peening

After the collapses of cavitation bubbles, shock waves and micro-jets are generated. When the bubbles are injected with a flow on a metal workpiece surface, the plastic deformation can be caused. Water cavitation jet peening takes this advantages. As shown in figure 2.2 (f), the water jet with high speed is injected from a nozzle to the workpiece surface [11]. Due to the pressure difference cavitation bubbles are generated and delivered together with the flow, by which cavitation bubbles are generated and collapse on the workpiece surface. Therefore, the residual compressive stress is introduced and surface properties are improved. Components with complicate part geometry can be peened with water cavitation jet peening, and there is no heat-affected zone. However, a complicated design of the nozzle and a water supply system are needed to ensure the sufficient generation of cavitation bubbles [14].

2.2.3 Machine impact peening

Apart from the shot peening and shotless peening, a machine tool can also be utilized to enhance metal surfaces. The most commonly used types are machine hammer peening and ultrasonic needle peening. During machine hammer peening, as shown in figure 2.2 (c), a tool with a spherical carbide tip directly impinges the workpiece surface [9]. An actuator is used to generate oscillation, which leads to a relative movement between the tool and the surface. Thus, residual compressive stress as well as the hardness of the upper surface layer is improved. Apart from this, the surface roughness on workpiece can be strongly improved by well-directed impacts with a controlled distance between each impact. Ultrasonic needle peening is similar to the machine hammer peening. The differences are that the impactors are excited with a high frequency (more than 20 kHz) and the sonotrode directly impacts the workpiece surface [15].

Compared to the shot peening and machine impact peening, the mentioned shotless peening methods require skilled operators and expensive and complicated equipment. In order to achieve good surface properties with simple equipment, ultrasonic cavitation peening has been developed in recent decades. This novel peening technology is described in detail in the next paragraphs.

2.2.4 Ultrasonic cavitation peening

Ultrasonic cavitation peening can improve the metal surface properties in the same way as other traditional peening methods. The phenomenon that the metal surfaces can be enhanced by ultrasonic cavitation bubbles was invented in the 1990s [16] and the scientific and technological terms of ultrasonic cavitation peening were first proposed in 2007 [17], in which a piezoelectric transducer is utilized and the sonotrode is partially immersed in a liquid. Using a piezoelectric transducer has many advantages: simple equipment, compact structure as well as a high output power. Due to the vibration of the transducer

sonotrode, cavitation bubbles are generated in a small gap. The gap which is between the end of the sonotrode and the treated surface is usually less than 1 mm. When the cavitation bubbles collapse, shock waves and micro jets are generated, which introduces plastic deformations onto the impacted surface. The schematic of the ultrasonic cavitation peening process is shown in figure 2.3. With the surface plastic deformation, the surface properties such as compressive residual stress, hardness, are improved. The increase of surface roughness is smaller compared to other conventional peening processes. When the ultrasonic cavitation peening is completed, the remaining material in water, such as metal and metal oxide particles, can easily be collected and recycled. In addition to this advantage, this surface treatment process is inexpensive.

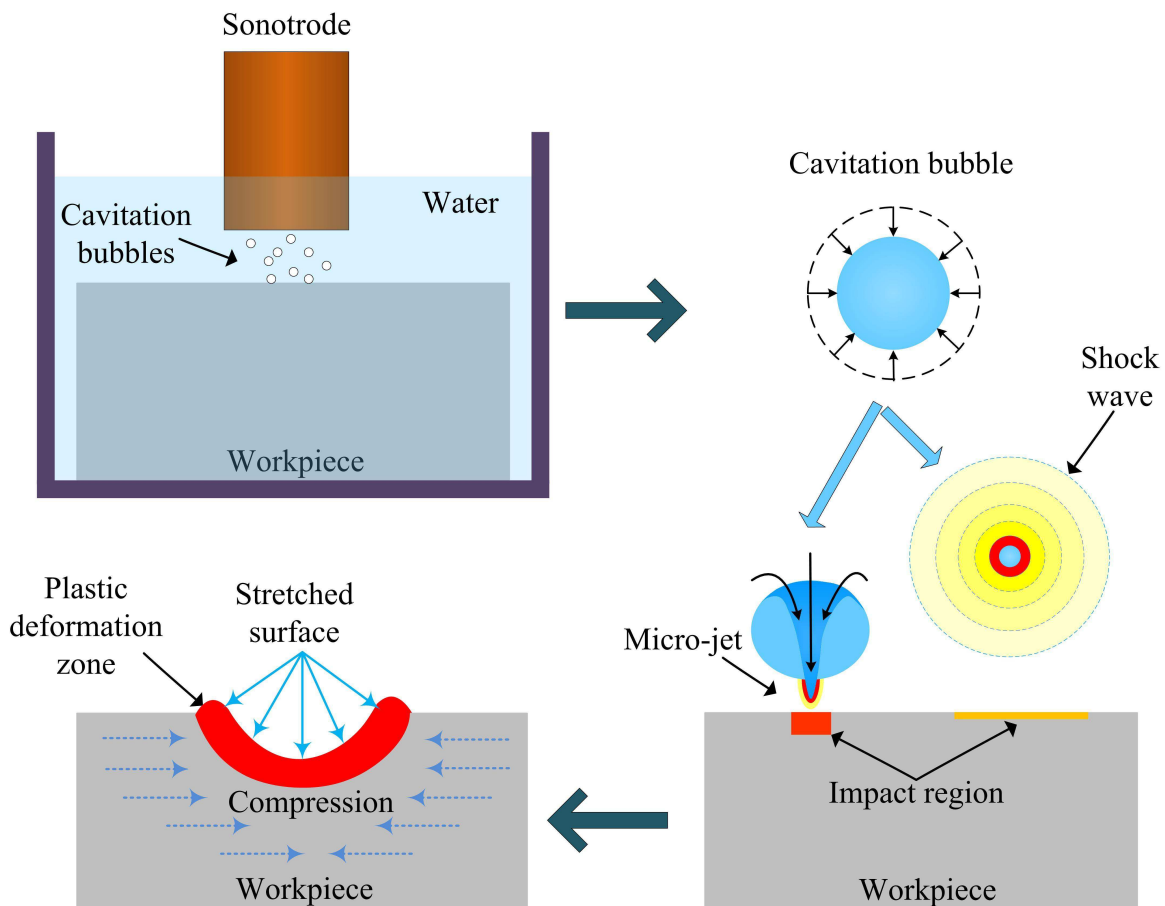


Figure 2.3: Schematic of the ultrasonic cavitation peening process.

Ultrasonic cavitation peening utilizes the initial stage of cavitation erosion on the metal surface. During cavitation erosion processes there are four successive stages: incubation period, acceleration period, deceleration period and steady-state period [18]. The initial stage is called incubation period when plastic deformation is generated while mass loss is negligible. As the process time continues, the second stage of cavitation erosion occurs and the erosion reaches the maximum rate whereas the rate of the plastic deformation decreases. In deceleration and steady-state periods, the erosion rate decreases and then stays steady. Therefore, the process time should not be significantly longer than the incubation period to obtain the best result. The third and fourth period should never appear in

the ultrasonic cavitation peening process.

2.3 Cavitation phenomenon and its effects on metal surfaces

In this section, the background of cavitation and the related equations are briefly introduced. The cavitation bubbles near a rigid wall and in a small gap are described in detail. The measurement methods of cavitation intensity and distribution are described as well. Finally, the modifications of metal surfaces caused by cavitation bubbles are presented.

2.3.1 Basic theory on cavitation

The common physical phenomenon of formation of a vapor cavity in a liquid is defined as cavitation. It was first mentioned by Lord Rayleigh in the late 19th century [19]. At the initial stage, some regions which suffered from transient low pressure become vapor, generating small bubbles. Those bubbles grow and then collapse. The collapses of bubbles are so violent that high pressure (can be as high as 6000 MPa [20]) and temperature (can reach to 2000 K [21]) are generated. The mechanism of cavitation is illustrated by figure 2.4. The phase diagram of water is shown with the temperature of the triple point T_r (273.16 K, 6×10^{-4} MPa) and the temperature of the critical point T_c (647.55 K, 22.06 MPa). These two points are connected by a solid curve which separates liquid and vapor. When the pressure is constant, vaporization by increasing temperature is defined as boiling. At the constant temperature, vaporization by decreasing pressure is defined as cavitation.

With the propagation of acoustic waves in a liquid, the pressure in the liquid consists of the static pressure and the oscillating pressure. If the sound pressure amplitude is higher than the static pressure, then the sum of static and acoustic pressure will be negative for the certain phase of each acoustic cycle. For understanding cavitation, a single bubble in an infinite domain of liquid is a basic case. By analyzing this phenomenon, some important issues in applications can be predicted and solved.

For a bubble in an infinite liquid, it is subjected to a uniform exterior pressure $P + 2\sigma/R$. P is the ambient pressure which consists of the constant hydrostatic pressure P_0 of the liquid and a various part. σ is the surface tension. R is the time-dependent radius of the bubble. According to the mass and energy conservation equations, the dynamic equation of the cavitation bubble is obtain in equation 2.1 [23].

$$R\ddot{R} + \frac{3}{2}\dot{R}^2 = \frac{1}{\rho_l}(p_i - P - \frac{2\sigma}{R}) \quad (2.1)$$

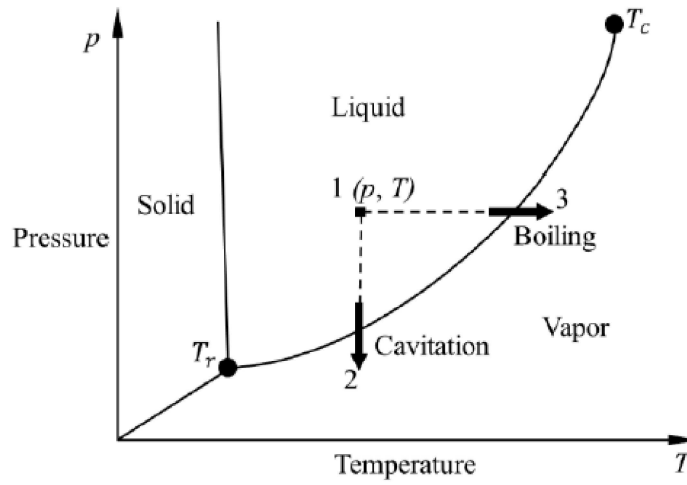


Figure 2.4: Schematic of the phase diagram of water [22].

where p_i is the initial inner pressure of a bubble, \dot{R} and \ddot{R} are first and second order time derivatives of the bubble radius. ρ_l is the density of the liquid.

In general, it is not possible to obtain full analytical solutions to these equations of motion. However, in this way, the approximate analytical solutions can be produced. From equation 2.1, the basic behavior of a single bubble is introduced in brief, but in most cases, the cavitation bubble occurs near a rigid boundary or in a small gap, which changes the dynamics of the cavitation bubble.

2.3.1.1 Ultrasonic cavitation near a rigid wall

In peening and cleaning applications the cavitation bubbles are generated near a rigid wall, so the growth and collapse of cavitation near a rigid boundary is a crucial problem to be studied. Two characteristic effects are believed to be mainly responsible for the destructive action: the emission of shock wave upon the collapse of bubble and the liquid jet towards the rigid boundary. These two phenomena will be introduced in the following paragraphs.

Single bubble near a rigid wall

When a bubble is far away from a rigid wall ($s/R_{max} > 3$, s is the distance between the rigid wall and the bubble center, R_{max} is the maximum bubble radius), only shock wave is generated at the collapse phase [24]. Lord Raleigh [19] first calculated the pressure that is caused by the shock wave and the time of bubble collapse. The collapse time means that the time from maximum bubble to the bubble collapse and is shown in equation 2.2.

$$t_{collapse} \approx 0.915R_0\sqrt{\frac{\rho_l}{P}} \quad (2.2)$$

where R_0 is the initial bubble radius.

This pioneering work was followed by many studies [25, 26, 27], which have led to a good understanding of the radial dynamics of an isolated bubble. This theory about the pressure pulse was first experimentally validated with acoustic measurements by Harrison [28]. In further investigations, Lauterborn et al. [20] simulated that the inner pressure can reach 6000 MPa based on the equation 2.1, when the bubble shrank from the maximum diameter of 3.5 mm to the minimum diameter of 50 μm . When the minimum bubble radius is reduced to less than 36 μm , the collapse pressure could be even higher [29]. Pecha et al. [30] observed the emission of a shock wave with a speed of about 4000 m/s which was produced by the last stage of the bubble collapse. Pressure in the range between 400 MPa and 600 MPa can be calculated due to the strongly nonlinear propagation. Brujan et al. [31] reported that in the surrounding of a cavitation bubble the emission pressure of the shock wave can reach 1300 MPa. Geers et al. [32] studied the internal gas and the external liquid for the dynamics of a spherical bubble. It was found that the influences of acoustic pressure are more important on the external liquid than on the internal gas.

In the case of $s/R_{max} \leq 3$, micro-jet occurs at the collapse phase [24]. A comparison between high-speed capture of a bubble motion and the calculation results of the velocity field was carried out [33] and shown in figure 2.5. After the bubble reaches the maximum size, it begins to collapse. The radial water flow is retarded by the rigid wall which is located below the bubble. As a result, the pressure at the upper bubble wall is larger than that at the lower bubble wall. The pressure difference results in the different accelerations of the lower and upper bubble wall, which leads to a larger velocity of the upper bubble wall towards the bubble center. Consequently, a liquid jet is formed and hits the lower bubble wall. At last, the micro-jet impacts the rigid wall.

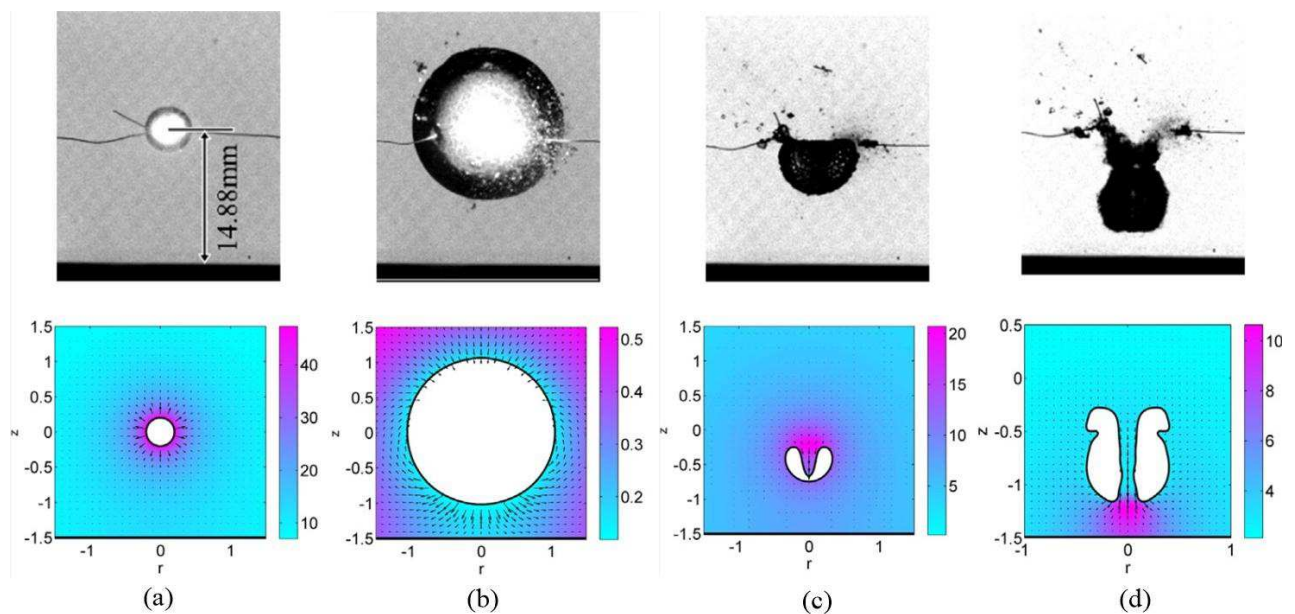


Figure 2.5: The comparison between high-speed capture of a bubble motion and the calculation results of the velocity field [33].

The liquid jet produced by the collapse of cavitation bubbles was also investigated by Kornfeld et al. [34]. They observed that the jet goes through the bubble from the center and then impinges on the boundary. This phenomenon was also photographically observed by Naude et al. [35]. Then Benjamin [36] found that the main reason for the material erosion is the liquid jet from the bubble collapse near a material boundary. Vogel et al. [20] reported that when the jet impact speed reaches 100 m/s, the pressure impacting on the rigid wall is approximately 450 MPa. To estimate the velocity of the micro-jet, Tzannkis et al. [37] recorded the relationship between the variation of bubble wall and the micro-jet utilizing a high speed camera. The results show that the velocity of the micro-jet can be described as the ratio of the maximum value of the cavitation bubble radius to the duration of bubble collapse, as shown in equation 2.3.

$$v_{microjet} \approx \frac{2R_m}{t_{collapse}} \quad (2.3)$$

where $v_{microjet}$ means the velocity of the micro-jet.

When the value of s/R_{max} becomes smaller, a double impact peak was observed by Tong et al. [38]. They considered that a toroidal cavity contributes to the special peak. Furthermore, Gonzalez Avila et al. [39] found that a second jet occurs due to the spherical convergence. The emission speed can reach as high as several hundred meters per second. The behavior of the liquid jet in a gravity-induced pressure gradient was later investigated as well [40]. Generally, the second jet is from a bubble torus which was observed and measured by a high speed camera and a hydrophone [41]. They concluded that the major erosion on a rigid wall caused by cavitation bubble is from the collapse of the bubble torus which generates the second jet. In the investigation conducted by Wang [42], the main erosion was observed in the contacted region between the bubble torus and the rigid wall. In his next study [43], the high temperature and high pressure area caused by a second explosion of the cavity on a rigid boundary was observed.

Bubble clouds near a rigid wall

In many real situations, multiple bubbles play an important role and show collective behavior due to bubble interactions. The multiple bubbles show new characteristics in chemical, optical and mechanical applications and are named as bubble cloud. The most common shape of the bubble cloud is hemispheric. The collapses of the bubble generally start from outside shell of the bubble cloud to inside [44, 45]. Each shell of the hemisphere cavity exposes towards the next inner shell, which leads to the transformation of the energy inwards. Therefore, the central energy density of the bubble cloud is much higher than that at the initial stage [46]. The hemispherical bubble cloud in non-Newtonian fluids was also investigated utilizing a high-speed photography. The results showed that the emission pressure of shock waves visibly decreases [47]. In bubble clouds, higher shock wave pressure is generated when the shock waves interact with each other [48]. If the hemispherical bubble clouds are near a rigid wall, the collapse is more violent.

2.3.1.2 Cavitation bubbles in a small gap

As already mentioned, the growth and collapse of cavitation bubbles near a rigid boundary can lead to micro-jets with high velocity and shock waves. If a cavitation bubble is generated between two parallel plates, both the dynamics of the bubble and the impact caused by bubble collapse are changed with respect to that near a rigid wall.

The dynamics of a cavitation bubble between two parallel walls was first theoretically investigated by Shima et al. [49]. They found that when the bubble oscillates in the center of the narrow gap, the spherical bubble at growth stage is converted into a prolate one. In another case, the behavior of a bubble with similar size close to one of two parallel walls looks like the situation of the bubble in the vicinity of only one rigid wall. The dynamics and impulsive pressure waves of a bubble in a narrow gap were investigated using a high-speed camera and piezo-type transducers [50]. The bubble is generated by an electric spark which can convert the local liquid into the vapor. The experiments showed that when a bubble collapses, it moves towards the near-by wall, since the influence of the near-by wall is larger. The measured impulsive pressures at two solid walls are the same order with any shape when a bubble collapses.

A cavitation bubble located in the middle of two parallel, rigid boundaries were explored experimentally [51]. At a standoff distance versus bubble size ratio $w^* = 2.2$, the cavitation bubble had a spherical shape at the stage of growth. w^* is defined as $w^* = L/R_m$. Here L is the standoff distance between the rigid wall and the tip of the sound radiator. R_m is the radius of the maximum bubble size. In a further study [52], it was found that if $w^* > 2.2$, the bubble is still spherical.

In the case of $1.61 < w^* < 2.2$, the bubble is not spherical any more but shows a ellipsoidal shape when it grows to the maximum size [53]. In the collapse stage, the bubble will be first divided into two parts towards to up wall and bottom wall and then collapse [54]. This collapse characteristic is named as the splitting collapse and shown in figure 2.6 (a). The oscillation of single bubble inside a narrow fluid-filled gap was also captured both the side and front by high-speed camera [55]. It was found that the bubble splits in the center and collapses with jet towards each of the wall. Xiong et al. [56] found that the jet velocity of a laser-induced bubble in a small gap is dependent on laser energy and inter-bubble distance.

When w^* reduces to 1.25, the bubble looks like a flattened hourglass when it reaches the maximum bubble size. At the collapse phase, first collapse occurs on the rigid walls and then liquid jets from the bubble center reach to the upper and lower walls. Thus, first and second impact are generated in this case. This kind of collapse characteristic is defined as the neutral collapse. In the study [54], the pressure peaks on the rigid walls in the cases of $w^* = 1.61$ and $w^* = 1.25$ were also investigated. The results show that the maximum amplitude of the pressure peak in the first case is much higher than that in the second case, since in the second case the impact energy is divided into two impact peaks.

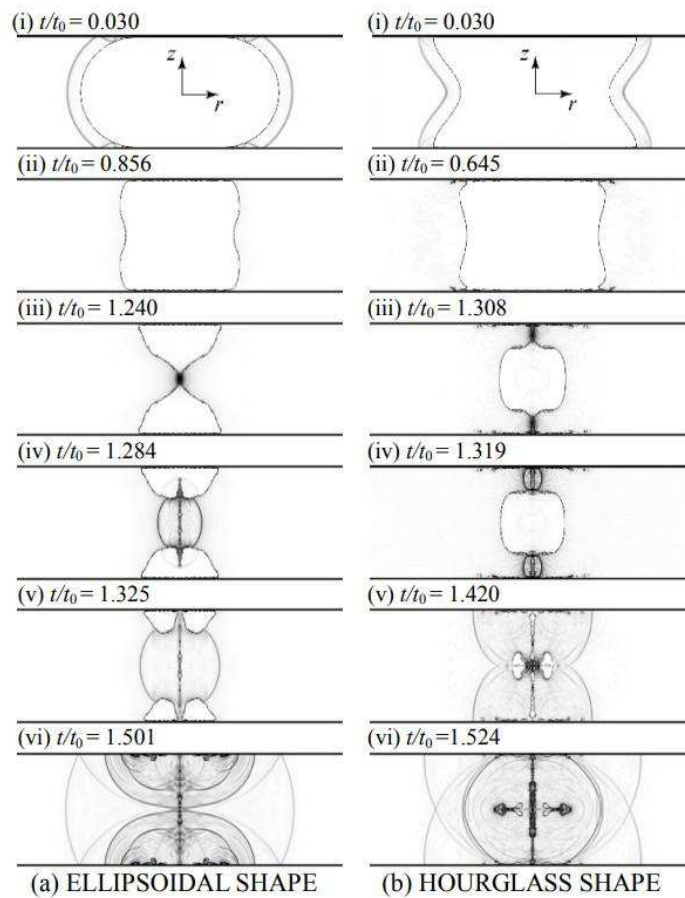


Figure 2.6: Successive images for the bubble in the case of (a) $w^* = 1.61$ and (b) $w^* = 1.25$ [57].

Apart from the single bubble, multi-bubbles have to be taken into consideration for realistic applications. In this case, the variations of the pressure peaks which are generated by cavitation bubbles are complicated, since there are acoustic radiation forces among bubbles. The change of pressure peaks with different w^* is still a gap in the previous studies. In next paragraphs, the interactions among bubbles will be introduced briefly.

2.3.1.3 Primary and Secondary Bjerknes Forces

There is a kind of acoustic radiation force among bubbles called Bjerknes force. Because of the periodic sound field, a gas bubble in liquid experiences volume pulsations. Moreover, with the pressure gradient in liquid, the bubble in the pressure field is subjected to a translational force. If the source of this gradient is the external acoustic pressure, the force is called primary Bjerknes force, which is experienced by single bubbles. In general, this force is time averaged.

The effect was first observed by Bjerknes [3]. However, the first satisfactory account of its origin was given by Blake [58]. Primary Bjerknes forces can make bubbles move in a stationary acoustic field. Regarding the movement pattern of the spherical bubble, the primary Bjerknes force makes the bubble move from the nodes in the pressure field to the

antinodes when the bubble's natural frequency is larger than the driving frequency. In contrary, if its natural frequency is less than the driving frequency, the bubbles are forced from the antinodes to the nodes [21].

Additionally, bubbles also interact with each other in a liquid under acoustic pressure. The interactions of bubbles are called the secondary Bjerknes forces [3]. The interaction forces include the attracting forces and repelling forces which can also make bubble structures in certain situations stable. The secondary Bjerknes force is generated by the radiation pressure due to the oscillation of the bubble itself. Second Bjerknes forces arise from the pressure field radiated from one pulsating bubble acting on a second bubble, regardless of whether those pulsations are the result of free or forced oscillations.

Therefore, due to the interactions of bubbles, when the bubbles are driven by acoustic pressure, the migration pattern and the dynamics of bubbles are complex, especially near a rigid boundary or in a narrow gap. However, many measurement technologies for cavitation bubbles can aid in understanding the cavitation phenomenon.

2.3.2 Distribution and intensity of cavitation bubbles

The current methods for the investigation of cavitation bubble distribution and intensity can be divided into two groups: experimental measurement and theoretical prediction. The most commonly used measurement and prediction methods are shown in figure 2.7.

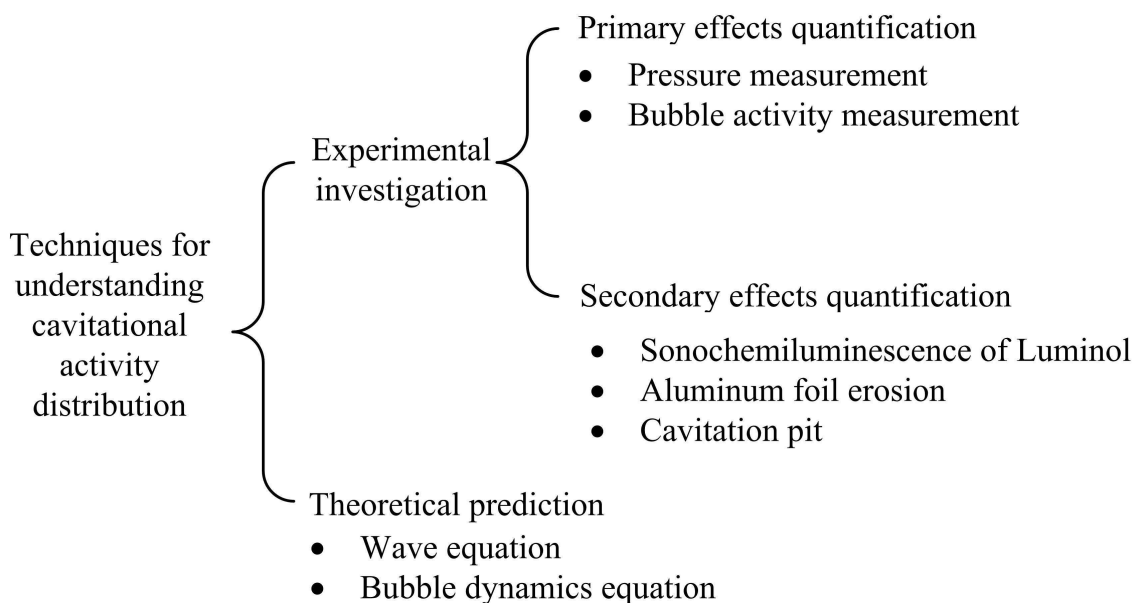


Figure 2.7: Classification of different types of investigation methods [59].

2.3.2.1 Experimental methods

In general, the experimental measurement methods for investigating the cavitation bubbles can be divided into two kinds: direct measurement and indirect measurement. The

first methods measure the effects that are produced as long as the bubble collapses, which can be considered as the primary effects of cavitation collapse, such as pressure measurement and bubble activity measurement. The other methods are based on the secondary effects of bubble collapse, in which the effects are generated after bubble collapse, such as sonochemiluminescence of Luminol and aluminum foil erosion. In the following paragraphs, the most commonly used test methods are introduced.

Pressure sensor

A pressure sensor is generally used to directly measure impact loads. Using a piezoelectric pressure sensor is the most commonly method due to the simplicity of the process. During measurement, the impact signals are converted directly into electric signals due to the piezoelectric effect. Thus, by analyzing the electric output the impacts caused by bubble collapse can be shown clearly. Franc et al. [60] used a commercial piezoelectric pressure sensor to measure the impact loads in a cavitation flow. The results of the measurements revealed a simple exponential law between a reference peak and a reference load. A PVDF (Polyvinylidene Fluoride) sensor was developed to evaluate the cavitation impact force as well. In this kind of transducer, two layers of tape were attached on the front size and an acrylic resin whose acoustic impedance is almost equal to PVDF was bonded on the back side [61]. Interestingly, when different material specimens were fixed on the top surface of the sensor, it was found that the measured results indicated that the cavitation impact energy was proportional to the material mass loss [62]. Although the pressure sensors are easy to operate and have high measurement accuracy, the sensor surfaces undergo severe erosion especially during high power cavitation.

High speed camera

Since the cavitation bubbles are small and the dynamics of bubbles are rapid, their presences can not accurately be observed by the naked eye. Cavitation bubble clouds can, as a whole ensemble, often be observed near ultrasonic horns. The dynamics of cavitation bubbles and bubble clouds can be captured by high-speed camera systems. From the captured photographs, the growth and the collapse of a cavitation bubble and of bubble clouds can be observed. Furthermore, some interactions of bubbles with the nearby surface can also be observed. The performance in which bubbles break particles by the rapid dynamics can also be observed [63]. So far, the fastest recording speed can reach 200 million frames per second and the exposure time can be even less than 5 ns [64]. In the experiments, a high-speed camera (Imacon 200) was used with the resolution of 1 $\mu\text{m}/\text{pixel}$. Although the high speed camera provides the images of bubble dynamics, the test conditions are usually difficult to achieve. For example, a high power light source and a transparent boundary are required.

Aluminum foil and cavitation pitting

As a basic method for detecting cavitation, aluminum foil can be laid inside ultrasonic containers or close to the ultrasonic horn. From the erosion pattern on the foil, the cavi-

tion intensity and distribution can be determined in relation to cavitation hot spots [65]. The method is simple for comparing the performance of ultrasonic containers on a time averaged scale by obtaining roughly estimate of the location of high pressure regions. Although this method is easy to operate and has a low price, the evidences of the erosion are very sensitive to the location of the aluminum foil, dissolved gas and liquid temperature.

Similar to the aluminum foil method, cavitation pitting is another way to evaluate the cavitation capability. Due to the hydrodynamic impact loads caused by cavitation bubble collapses, pits are generated on the treated surface. These cavitation pits can be utilized as the signal of the impact loads and reflect the material constitutive behavior [65]. The cavitation impact loads can be estimated by the pit dimensions . By analyzing the numbers of pits per unit surface region, the cavitation intensity or aggressiveness is characterized. For the pit measurement, aluminum alloy, duplex stainless steel, and Nickel-Aluminum Bronze can be used as the target material to predict the impact loads [66]. However, this method is restricted by the material characteristics and cannot be used to precisely evaluate the cavitation intensity due to the overlap of the impact loads in the same area.

Sonoluminescence

It is well known that the effects of sonochemistry are mainly induced by the collapse of cavitation bubbles. Owing to these influences, using sonochemical effects to reflect the cavitation field is an effective way. Sonoluminescence (SL) and sonochemiluminescence (SCL) are usually utilized to capture the sonochemical reaction fields [67]. During these measurements, a blue fluorescence is emitted due to the reaction between luminol ($C_8H_7N_3O_2$) [68] and hydroxyl radicals generated by acoustic cavitation. Compared to single-bubble sonoluminescence, multi-bubble sonoluminescence (MBSL) is relatively easily to make. Many researchers [69, 70, 71] studied cavitation fields by taking advantage of SL and SCL.

Both of them can show the effects of the superposition of ultrasound waves in a certain period. At higher ultrasonic power the intensity of SCL in an aqueous luminol solution is much stronger than that of SL in distilled water. With increase of the ultrasonic power, both of the SL intensity and SCL intensity increase to a maximum value and then decrease. The range of peaks is usually located in the range of 100 W/L and 200 W/L [72]. The pH value also affects MBSL. The sonoluminescence intensity from aqueous solutions is dependent on the pH value of the solution. When the pH value is larger than 7, the relative sonoluminescence intensity of n-alkyl acids is larger compared to the case when the pH value is less than 7 [73].

In this section, different cavitation measurement methods were described. Apart from the experimental investigation of cavitation bubbles, the theoretical predication is another way to more deeply understand cavitation phenomenon.

2.3.2.2 Theoretical prediction

Theoretical prediction is the other way to investigate the distribution and intensity of cavitation bubbles. Cavitation bubbles are generated by the change of sound pressure during the propagation of sound waves in a liquid. However, the bubbles in a liquid disturb the propagation of sound waves. Therefore, a basic understanding of pressure wave propagation in a bubbly liquid is important for detailed studies of the mechanism of cavitation.

The speed of sound c_m in a bubbly liquid is lower than that in a pure liquid, which can be simply explained by equation 2.4 [74].

$$c_m = \frac{1}{\sqrt{\rho_m X}} \quad (2.4)$$

where ρ is the density and X is the compressibility of the bubbly liquid. In a liquid with cavitation bubbles, the compressibility increases due to the gas bubble, but the density changes little. Therefore, the speed of sound decreases according to equation 2.4.

The sound wave propagation in one dimension bubbly liquid is also shown in figure 2.8. The solid curve and the dotted curve mean the sound propagation with the same sound source in a pure liquid and in a bubbly liquid, respectively. With the separation of Δb many bubbles are evenly distributed on a line. When a sound wave goes through the liquid with a bubble, the wavelength becomes shorter and shorter due to the influence of bubbles. Finally, the wavelength of input pressure wave λ is reduced to λ_m , resulting in the reduction of sound speed. The sudden pressure change is due to the great change of the sound propagation by the small bubble. In other words, pressure is buffered due to the high compressibility of the gas bubble.

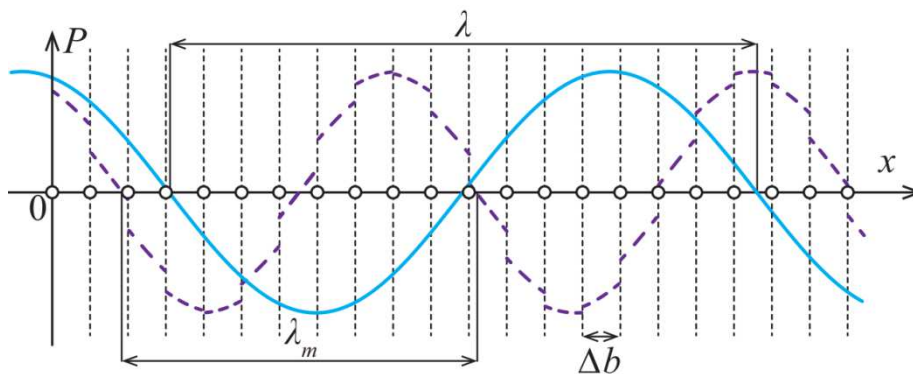


Figure 2.8: The reduction of the wavelength due to the delay distance is caused by the induced oscillation of multiple bubbles [74].

However, the bubble sizes in a cavitation bubbly liquid are different. The distributions of continuous bubble size are considered a Gaussian distribution $f(a)$. a is the instantaneous bubble radius. It is assumed that the bubble radii range from $a_1 = 5 \mu\text{m}$ to $a_2 = 3 \text{mm}$. The standard deviation of the cavitation bubble size distribution σ_B is set to 2mm . a_0 has

a value of $(a_1 + a_2)/2$. The parameters chosen above were well validated by experiments in [75].

$$f(a) = \begin{cases} \frac{1}{\sigma_B \sqrt{2\pi}} \exp[-(a - a_0)^2 / \sigma_B^2], & a_1 < a < a_2, \\ 0, & \text{otherwise} \end{cases} \quad (2.5)$$

Based on the distribution function of cavitation bubbles, Daehnke et al. [76] developed a model of sound propagation in bubbly liquids to describe the wave number k_m which is shown in equation 2.6.

$$k_m^2 = \frac{\omega^2}{c_m^2} + 4\pi\omega^2 \int_0^\infty \frac{af(a)}{\omega_0^2 - \omega^2 + 2ib\omega} da \quad (2.6)$$

where $i = \sqrt{-1}$, ω_0 and b denote the natural frequency and the damping constant of a cavitation bubble, respectively. ω is the angular frequency of the sound source. This methodology can be considered as the classical theory for linear wave propagation in bubbly liquid.

In this classical model, the interactions of bubbles are not taken into account. However, the interactions affect the sound propagation in a bubbly liquid due to the change of bubble distribution. Fuster et al. [77] considered the bubble interactions and improved the classical model. The extended resonance frequency and damping coefficient are shown in equation 2.7 and equation 2.8.

$$\omega_0^2 = \frac{P_0}{\rho_m a} \left(\text{Re}\Phi - \frac{2\sigma}{aP_0} \right) + \frac{\text{Re}I_0}{a^2} \quad (2.7)$$

$$b = \frac{2\mu}{\rho_m a^2} + \frac{P_0}{2\omega \rho_m a^2} \text{Im}\Phi + \frac{\omega^2 a}{2c} + \frac{\text{Im}I_0}{2\omega a^2} \quad (2.8)$$

where p_0 is the reference pressure of the liquid, Φ is a complex dimensionless parameter and will be given in the following, μ is the coefficient of viscosity, I_0 is the potential from the surrounding bubbles and is defined as:

$$I_0 = \frac{1}{\rho_m} \frac{3\beta}{(a\omega/c)^2} \left[1 - e^{-i\frac{2.3a\omega}{c\beta^{1/3}}} \left(1 + \frac{i\omega c \beta^{1/3}}{2.3a} \right) \right] (p_{ge}\Phi - \frac{2\sigma}{a} + 4i\mu\omega). \quad (2.9)$$

where p_{ge} is the initial gas pressure of a bubble, σ is the surface tension coefficient, β is the bubble concentration. The complex dimensionless parameter Φ is expressed as:

$$\Phi = \frac{3\gamma}{1 - 3(\gamma - 1)ix[(i/x)^{1/2} \coth(i/x)^{1/2} - 1]} \quad (2.10)$$

where

$$x = D_f / \omega R_0^2 \quad (2.11)$$

where D_f is the gas thermal diffusivity, γ is the ratio of specific heats. Thus, the wave numbers with the consideration of bubble interactions can be calculated using equation 2.6, equation 2.7 and equation 2.8. These parameters will be used in Section 4 to investigate the sound distribution in a thin bubbly liquid layer. After briefly understanding the characteristics of sound propagation in bubbly liquids, the modeling of sound field is introduced in the following paragraphs.

Any sound source can be subdivided into a collection of point sources and any one of those can be considered to radiate spherical acoustic waves independently. A typical sound source which is a flat round plate is shown in figure 2.9. The flat surface reflects the radiation into half-space with the entire acoustic energy. It is considered the contribution to the pressure at a point of observation M is from an elemental source of infinitesimal area dS' .

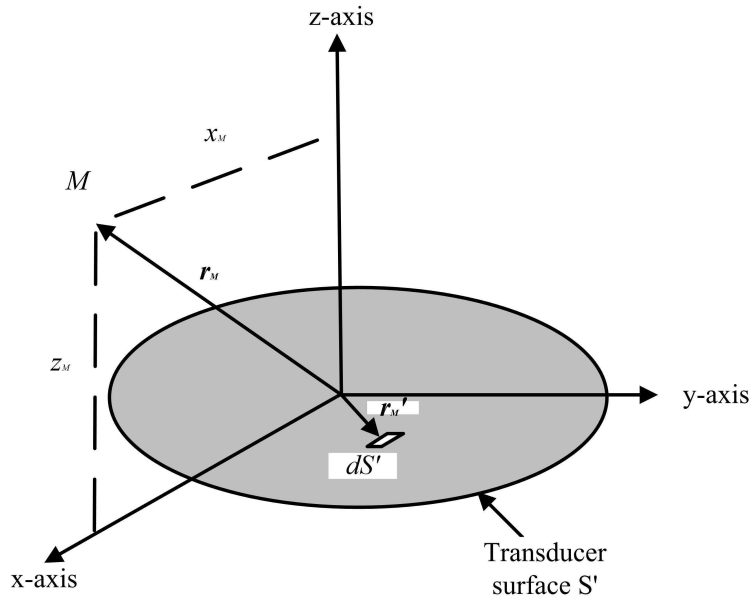


Figure 2.9: Geometry for the calculation of the pressure field at a point M [78].

Therefore, the sound pressure at any point M in front of it can be described as equation 2.12 [78].

$$p(\mathbf{r}_M) = \frac{\rho\omega}{2\pi} \cdot u_0 \cdot \iint_{S'} \frac{e^{-i(k_m |\mathbf{r}'_M - \mathbf{r}_M|)}}{|\mathbf{r}'_M - \mathbf{r}_M|} dS' \quad (2.12)$$

where u_0 is the amplitude of the plate velocity, \mathbf{r}_M is the position vector of the point M in space, \mathbf{r}'_M is the position vector of the plate active element and S' is the active plate area.

In the practical situations, the boundary conditions have to be taken into consideration. The pressure vanishes on an ideal pressure-release boundary. Regarding a rigid wall, the sound wave is totally reflected [75]. These description can be used to simulate the sound field in Chapter 4.

All the explanations of sound propagation in bubbly liquids can help to understand more comprehensively a spatial sound propagation in a liquid. With the classical model of sound propagation in a bubbly liquid, the distribution of sound pressure was investigated [75]. However, the distribution of sound pressure with the consideration of bubble interactions was not studied till now and will be investigation in this work.

2.3.3 Cavitation on metal surfaces

The previous sections provided the experimental and theoretical methods for the investigation of cavitation. This section will give another important background knowledge for the investigation of ultrasonic cavitation peening. Since ultrasonic cavitation peening is based on the impacts caused by cavitation bubbles, it is necessary to understand the interactions between surface properties and cavitation. The changes of metal surface microstructures induced by cavitation treatment and the characteristics of cavitation pits are presented since they are the fundamental elements of the formation of surface erosion. Finally, the stages of cavitation erosion are described, especially for the stage which is used for ultrasonic cavitation peening.

2.3.3.1 Micro structures of modified metal surface and cavitation pits

The impact pressure generated by the collapse of cavitation bubbles can be used to improve metal surfaces. At the initial treatment phase, the sizes of the grains become smaller takakuwa2015movement. No further modifications occur if the cavitation process time increases continuously. The modification results of metal plates by cavitation were investigated by Shchukin et al. [79]. They supposed that the jet has more influences on the lower melting point metal. The unprotected surface is modified and new oxide layer is formed simultaneously. In the macroscopic aspect, small pits are generated on the tested surface after cavitation process.

Pit formation is of paramount importance in understanding the basic mechanism of ultrasonic cavitation peening, because the treated surface is caused by thousands of small pits. However, pit formation is still subject of controversy since the test conditions are somewhat different from each other. As mentioned in Section 2.3.1, shock wave and micro-jet are formed through the collapse stage of cavitation bubbles. When the bubble collapse occurs near a solid surface, a high impact is generated onto the solid surface. The metal surface suffers from local plastic deformation due to the high impact, which leads to the formation of cavitation pits. A typical example of a stainless steel specimen with cavitation pits was investigated [18]. The pits shown in figure 2.10 are almost shallow plastic

deformations and cover the eroded area without any overlap. This because the process time is controlled to make sure that only one impact occurs at the same region. In this case, one pit is produced by only one bubble collapse. The pit size depends on the distance between bubble center and the boundary, the bubble size and pressure direction after collapse. Ahmed et al. [80] found that the shapes and the diameters of the pits do not vary with the cavitation exposure.

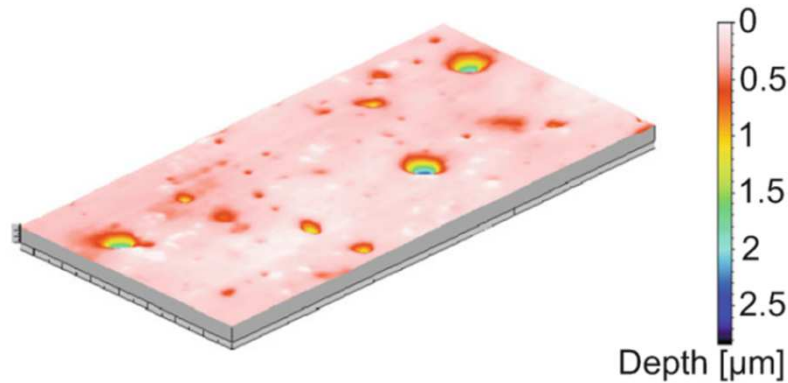


Figure 2.10: The typical treated surface with pits caused by cavitation [18].

In terms of treated material, the formation of pits is related to the material strength. Thus the determination of the properties of the material is a basis to predict the cavitation erosion. A pit is formed only when the impact load exceeds the material threshold. The threshold of metallic material is considered as the yield stress. If the yield stress of the material is greater than the impact loads, the impact loads cause no damage on the material and the elastic behavior dominates. Only when the impact load is larger than the material yield stress, a permanent pit will be produced on the treated surface. However, the impact duration is another important factor in the pit formation. Even if the impact load is high without sufficient impact duration, no pit will form on the material [81]. This is because the energy of the impact load is much smaller in an impact with short duration than in one with the same stress peak and a short duration.

2.3.3.2 Phases of cavitation erosion and incubation period

After the continuous impacts by cavitation bubbles, deformation or erosion occur on the workpiece surface. In general, the cavitation erosion process on a specimen surface can be divided into several stages. These stages can be distinguished either by mass loss or by volume loss.

Depending on the mass loss, the cavitation erosion is divided into five stages [82]: incubation stage, acceleration stage, maximum rate stage, deceleration stage and terminal stage (steady state). In the initial stage, the incubation stage, the material only undergoes plastic deformation instead of much mass loss. In the following acceleration stage, the material erosion loss rate increases due to the damage initiation and propagation and then the mass loss rate stays constant for a short period. Then, in the deceleration stage, the erosion rate decreases as the material surface topography changes dramatically and

the material interface is modified. In the final stage, the mass loss is constant.

There is another way to evaluate the cavitation erosion process by volume loss. There are four stages [18]: incubation period, acceleration period, deceleration period and steady-state period. Figure 2.11 illustrates the volume loss curve and the volume loss rate curve during cavitation erosion.

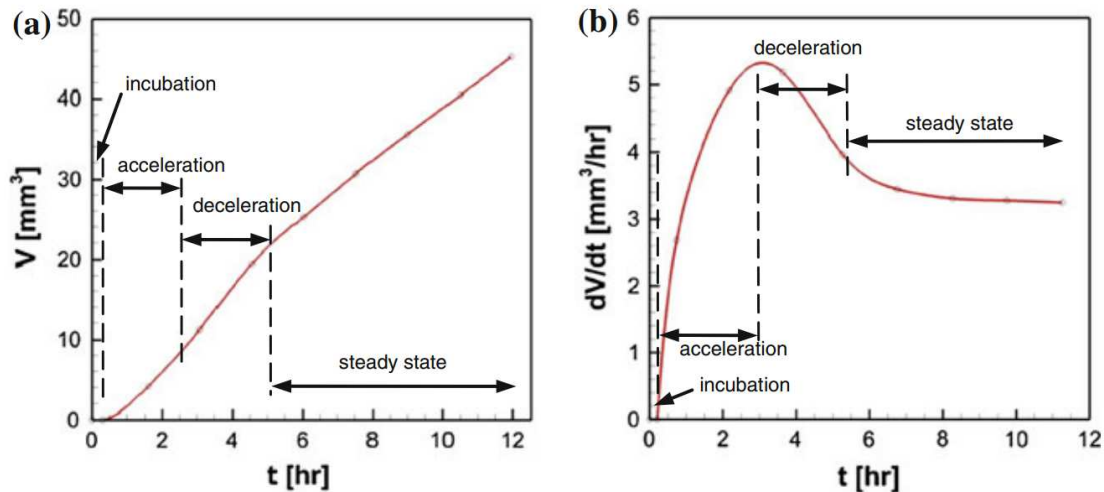


Figure 2.11: (a) Volume loss versus time curve, (b) rate of volume loss versus time curve [18].

The four stages of cavitation erosion process by volume loss are explained in detail here.

- **Incubation period:** at the beginning of the cavitation erosion process, the volume loss consists of isolated pits and many plastic deformation pits produced by the cavitation impact. The cavitation induces plastic deformation in the subsurface layers [83] which makes the material surface become hard.
- **Acceleration period:** As the processing time increases, the number of impact events increases correspondingly. Thus, erosion pits continuously overlap and the deformation is generated on the material surface. The accumulation of such localized deformations begins and an acceleration period is observed. In this period the volume loss rate increases until it reaches a maximum value, since most of the treated surface are hardened and most of the insufficient particle-matrix is drawn out the matrix.
- **Deceleration period:** during this period, the rate of volume loss decreases. Then material failure is caused, and sometimes in this period the erosion rate is almost constant. After the deceleration period the material surface roughness changes obviously due to much volume loss.
- **Steady-state period:** finally, the rate of volume loss becomes constant and the mass loss almost keeps a stable value. This period is named steady-state period or terminal stage.

However, only the incubation period is beneficial for the metal surface enhancement due to the hardening effects and negligible mass loss. Thus, in the next paragraphs, this initial period will be introduced in detail.

In the incubation period only small mass loss and little permanent deformation occurs. Sometimes the development of micro-cracks and the local displacement of the material micro particles occur as well [18]. The reduction of grain size caused by the impacts is beneficial for the improvement of hardness.

For an ideal untreated material, strain is nearly zero everywhere inside the material. When the material is impacted by the hydrodynamic impacts due to bubble collapses of cavitation, a progressive hardening on the surface of material occurs. The hardness of the treated workpiece increases progressively after each impact and the surface strain step by step increases with increasing processing time of cavitation. As shown in figure 2.12 after the first covering of the original material, surface strain ε is increased. The first covering means that all the required impact regions are firstly treated without overlapping impacts. This is an ideal case for theoretical analysis. In the real situation, the impacts caused by cavitation bubbles are applied randomly on the workpiece surfaces. When all of the required area are totally treated, it is considered before that moment it is the first covering. Based on the first covering, the second covering means that all the required impact regions are secondly totally treated. By this analogy, the surface strain is increased to maximum ε_U after several coverings. When the surface strain reaches the ultimate strain ε_U , the ultimate tensile strength ε_U occurs, which means that the material damage will be produced if there are more impacts. Therefore, the process time corresponding to ε_U is the end of the incubation period, since in this period only plastic deformation occurs.

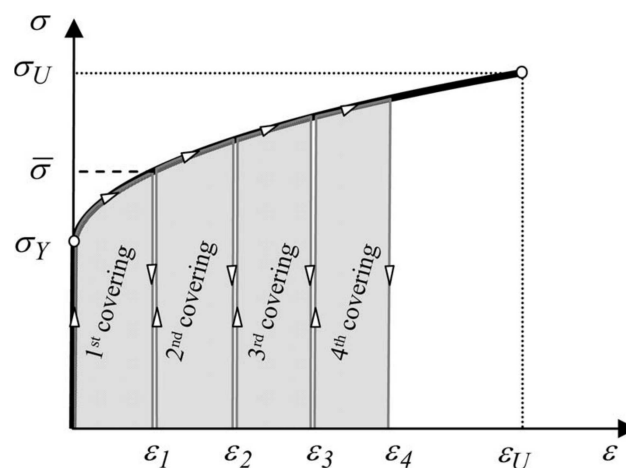


Figure 2.12: Material response during the incubation period [84].

The surface properties improved by cavitation were studied as well [85]. The compressive residual stresses rise quickly with cavitation treatment, but the stresses no longer increase after a long cavitation process time. The surface microhardness increases during incubation period and decreases later [85], since the dislocation density firstly rises and then micro-cracks occur on the material surface.

Section 2.3 described the related knowledge of cavitation and the interactions between cavitation and metal surfaces. In the above description, it can be seen that whether it is evaluated by mass loss or volume loss, the incubation period is shorter than the other periods. Generally, the incubation period depends on the impact loads and material properties. Therefore, this period is difficult to evaluate in tests. Using the plastic deformation to evaluate the incubation period will be a good method, since in the period much plastic deformation and small mass loss are generated. This method is not investigated yet and will be studied in Chapter 6. In the following section, the research about this surface enhancement technology is introduced.

2.4 Development of ultrasonic cavitation peening

In the above sections, all the background knowledge for better understanding the ultrasonic cavitation peening was introduced. As a promising peening methods, ultrasonic cavitation peening has been mainly investigated during the last decade. This process only requires a liquid as working solution. It is efficient and causes less pollution compared to conventional peening processes. In the following, the developments of this process will be described in detail.

In 1987, Takahashi et al. [86] attempted to develop an ultrasonic device for metal working and surface treatment. The effect of ultrasonic cavitation was investigated. In their studies, the test pieces which were made of mild steel (C: 0.09 %) were annealed in a vacuum at a high temperature to remove residual stress. Next, each piece was exposed to ultrasonic cavitation with the standoff distance of 0.3 mm and at a resonance frequency of 20 kHz and with the vibration amplitude of 15 μm . As a key parameter of ultrasonic cavitation peening, the standoff distance in this thesis is defined as width between the sonotrode tip and the workpiece surface. After treatment, the hardness and the fatigue limit increased by 24% and 11%, respectively.

The influences of ultrasonic cavitation on the surface qualities of AISI 4140 and AISI 1045 steels were explored at a standoff distance of 0.7 mm [87]. The vibration amplitude was 40 μm and the working frequency was about 20 kHz. The sketch of the ultrasonic cavitation peening bench is shown in figure 2.13. The workpiece is immersed in the distilled water. They found that the formation of residual stress and texture caused by ultrasonic cavitation is not significantly different from the changes caused by water jet cavitation peening. The deformation mechanism in cavitation erosion is similar to the shot peening process, but the depth of the residual stress of the workpiece under cavitation attacks is less than that under shot peening.

A standoff distance of 1.5 mm, a vibration amplitude of 37.5 μm and the working frequency of 20 kHz were utilized to treat the surfaces of AISI 304 stainless steel specimens [16]. The residual stress induced by ultrasonic cavitation was detected by a X-ray diffractometer. The effect of water temperature on residual stress was studied with the temper-

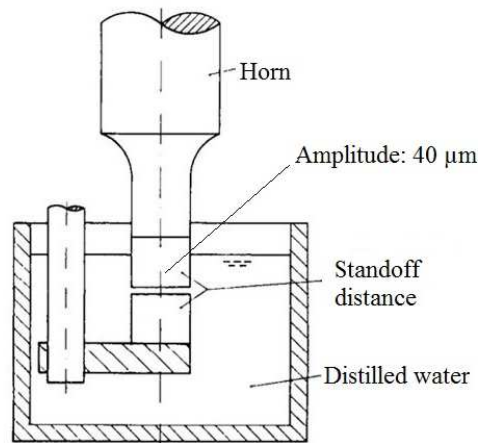


Figure 2.13: Ultrasonic cavitation peening setup [87].

ature interval of 15 °C. The results showed that when the temperature is less than 65 °C, the values of residual stress almost do not change, around 600 MPa. However, when the temperature increases to 95°C, the value reduces to 200 MPa. Therefore, at high temperature the residual stress decreases significantly. Additionally, no matter how much the temperature was, a high compressive residual stress (420 MPa) was introduced by the high vibration amplitude (70 μm) even the process time is as short as 18 s. With the increase of the processing time, the compressive residual stress increases and then reaches a saturation value. The maximum residual stress locates about 70 μm under the treated surface. The maximum value of the surface roughness is as low as 0.63 μm even in the case of a long process time and high vibration amplitude.

Kim et al. [88] investigated the influence of different temperatures and vibration amplitudes on the damage behavior in seawater using ultrasonic cavitation as well. They presented that the higher temperatures were associated with higher corrosion. The weight loss increased with the increase of vibration amplitude.

Ultrasonic cavitation in particular has many advantages in the field of micro-machining. After micro-machining, some raised edges or small pieces are still attached on a workpiece. The edges and the small pieces are named as burrs. Toh et al. [17] found that the burrs can be removed and the residual stress can be induced after machining utilizing ultrasonic cavitation peening. In the tests, the specimens were treated at frequencies of 40, 80 and 120 kHz. It was found that sonication at 40 kHz has the most significant effect on minimizing burr-height formation, regardless of workpiece hardness and immersion time. A mixture of Al₂O₃ and distilled water was also used as medium to investigate ultrasonic cavitation peening [89]. In the experiments, the working frequency was 20 kHz and the standoff distance was about 1 mm. The process with the mixture medium has two main positive aspects: it was capable of removing burrs on treated surface with a higher efficiency and a reduction of roughness was observed which is shown in figure 2.14. The abrasive particles were added into the working liquid as nuclei for the formation of cavitation bubbles. By the collapse of those bubbles, the particles were accelerated to remove the material on the surface. In this way, the roughness decreased rapidly.

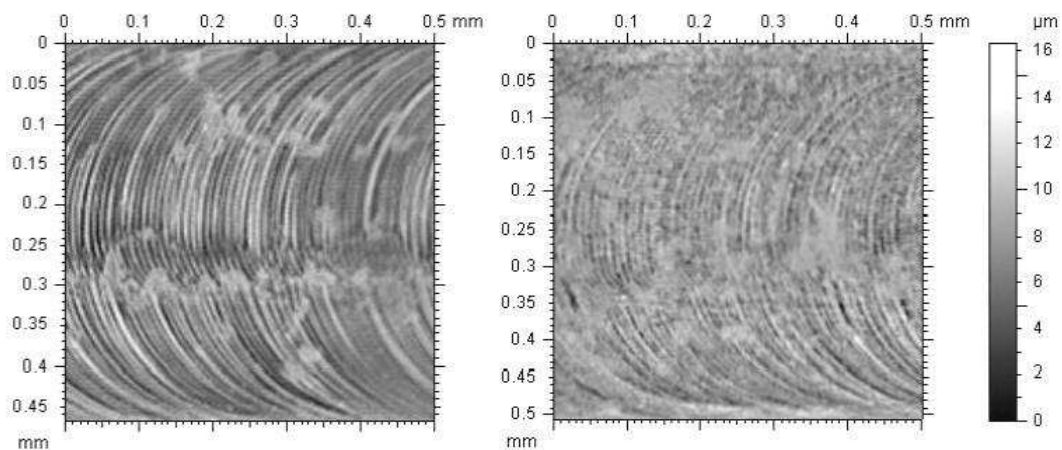


Figure 2.14: Surface topography before and after ultrasonic cavitation peening [90].

Sasaki et al. [91] discussed the effects of cavitation peening on the fatigue properties of cold-rolled stainless steel sheets with a thickness of 0.1 mm. The working frequency was 19 kHz and the vibration amplitude was 12.5 μm . The distance between the sonotrode tip and the specimen surface was 1 mm. After ultrasonic cavitation peening, the fatigue limit increased by approximately 10% while the surface roughness slightly decreased. This means that the homogenization on a treated surface caused by cavitation improves the fatigue resistance. Ultrasonic cavitation peening is a good way to relax the microscope strain preliminary induced by cold working.

Gao et al. [2] measured the surface hardness, surface profile, and roughness of stainless steel and nickel alloy surfaces before and after ultrasonic cavitation peening. During these tests the specimens were positioned in a holder with a standoff distance of 1 mm. The cavitation bubbles were generated in water at a constant frequency of 20 kHz. In their experiments, the two kinds of workpiece samples were polished before being treated by ultrasonic cavitation peening. In figure 2.15, the SEM images of nickel alloy samples in untreated (left) and treated (right) state are shown. There is no significant surface erosion being observed. After treatment, the surface roughness increased with the increase of the vibration amplitude, but the values were still less than 6 μm even with high vibration amplitude. Regarding the microhardness, under the vibration amplitude of 20 μm the hardness of stainless steel and nickel alloy surfaces increased 18% and 20%, respectively. Therefore, Gao et al. consider ultrasonic cavitation peening as a potential surface treatment technology since the hardness increased without a significant increase in surface roughness.

In 2017, Janka et al. [92] investigated the improvement of the surface hardness of stainless steel and aluminum alloy using ultrasonic cavitation peening. In their experiments, the working frequency and vibration amplitude were set to 20 kHz and 150 μm , respectively. The standoff distance was set to 0.5 mm. Both the surface hardness and the mass loss were measured at different process time. It was found that when the mass loss started to increase rapidly, the surface hardness started to decrease almost at the same moment. Thus, it can be concluded that the optimal process time is when the mass loss rate increases

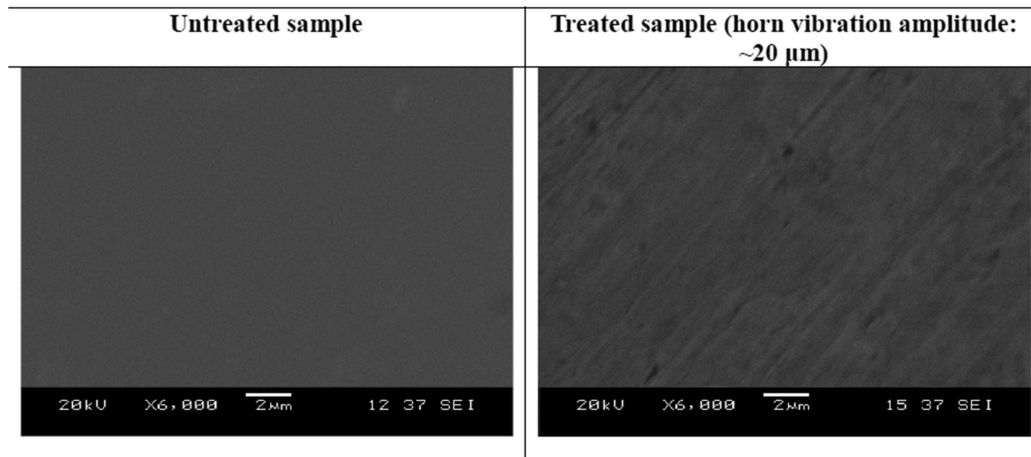


Figure 2.15: The SEM images of an untreated (left) and treated (right) sample by ultrasonic cavitation peening [2].

dramatically.

Besides the flat tip end of the sonotrode for ultrasonic cavitation peening, the sonotrode with concaves were also investigated at the frequency of 17.5 kHz [93]. The radii of concaves are from 1 mm to 4 mm with the interval of 1 mm. During the measurements, the impact loads were recorded by a piezoelectric sensor and the cavitation bubbles were captured by a high-speed camera. The results show that the sonotrode with the concave of 4 mm radius generated the largest impact. Thus, it is deduced that of ultrasonic cavitation peening can be improved effectively by using the sonotrode with the proper geometry.

Ultrasonic cavitation can also be used to improve the properties of deep notches [94]. In the tests, the sonotrode vibrated with the amplitude of 35 μm at a frequency of 20 kHz. The cavitation bubbles concentrated near the notch tip during the process, as shown in figure 2.16. The increase of the residual stress near the notch tip was measured after cavitation treatment. Ultrasonic cavitation is also used to treat the inner surface of a nozzle [95]. In the investigation, the cavitation bubbles was generated in the region near the pressure antinodes where the maximum pressure is generated owing to the effects of a standing wave. This kind of method can easily achieve the enhancement of inner surfaces of holes or nozzles.

In Section 2.4, the influences of temperature and vibration amplitude on the treated surface were introduced. With the temperature in the range of 5 $^{\circ}\text{C}$ and 65 $^{\circ}\text{C}$ a high residual stress can be generated while large vibration amplitude causes strong cavitation. However, the influence of the standoff distance on the treated results seems to be an ignored issue during ultrasonic cavitation peening.

In this chapter, the surface enhancement technologies, cavitation in a small gap and on metal surfaces and the developments of ultrasonic cavitation peening were introduced in detail. Three important issues which need to be investigated are described. The three issues are sound field distribution with the consideration of bubble interactions, detection of the incubation period utilizing the variations of plastic deformation and the influences

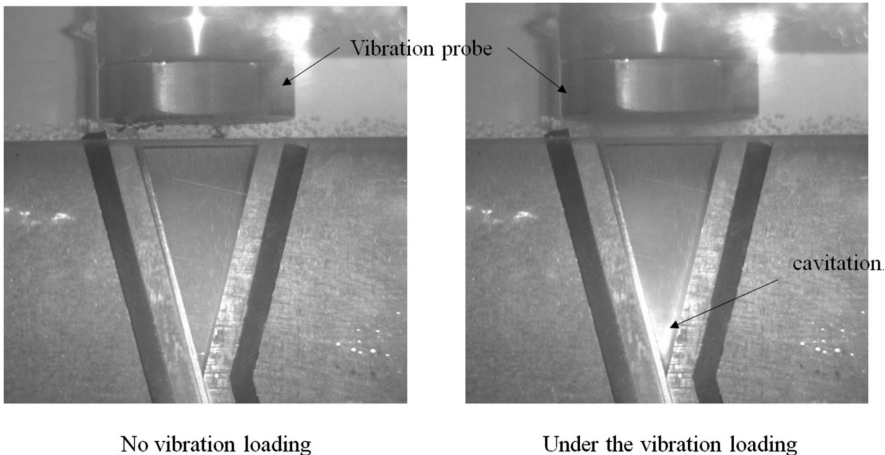


Figure 2.16: Images of the notch tip without cavitation and with cavitation [94].

of the standoff distance on the results of treatments. In the following chapters, all these issues will be analyzed and answered.

3 Research objective

In the motivation, two interesting phenomena related to ultrasonic cavitation peening were presented. Cavitation bubbles can induce different impact effects and thus improve surface properties of metal parts by cavitation peening. At the same time, however, cavitation bubbles change the sound propagation in the working fluid, which makes it different to design equipment for ultrasonic cavitation peening, especially when deep and narrow holes are concerned. In the following, the state of the art is analyzed. Open research questions are presented and the research objective of this thesis is formulated.

3.1 Analysis of the state of the art

During ultrasonic cavitation peening, cavitation bubbles are generated between the horn tip and the treated surface. When the sound wave propagates in the bubbly liquid, the incident sound wave is scattered by the small bubbles. Meanwhile, the bubbles vibrate by themselves, which leads to the further interactions of cavitation bubbles. In previous sound field distribution models for cavitation peening, these interactions were not taken into account. In this thesis, the sound field distribution model and the bubble interaction model will be combined together. The goal is to develop a model which is capable to calculate sound field in ultrasonic cavitation peening.

When a bubble is trapped in a small gap, the standoff distance affects the impacts which are induced by the bubble collapse. The ultrasonic cavitation peening process requires a small gap whose width is generally less than 1 mm. However, in investigations so far, the influences of the small standoff distance on the impact characteristics have been ignored. The researchers used one fixed standoff distance for their studies, but did not explained the choice of this parameter. It is assumed that when the standoff distance equals the maximum diameter of the cavitation bubble, the highest impact force is generated on a workpiece surface. A model of the relationship between the operation parameters (the optimal standoff distance, vibration amplitude and frequency) will be built to obtain the proper choice. Using this model a optimal operation parameter can be determined when the other two operation parameters are given. Two different experiments for measuring impact forces will be carried out to check the simulation results.

Due to the impact caused by cavitation bubbles on the workpiece surface, the surface

properties can be improved in the same way as by other peening methods. During the cavitation process, both plastic deformation and erosion take place. The erosion directly causes the mass loss of workpieces. At the beginning of the process, mainly plastic deformation occurs but only little erosion, which is beneficial for ultrasonic cavitation peening. However, the plastic deformation can not be measured directly. Although the total volume loss and the mass loss can be directly measured and are usually utilized to estimate the process, both of them can not directly evaluate the ultrasonic cavitation peening process. The total volume loss is caused by the plastic deformation volume and the volume change due to mass loss. Thus, the plastic deformation volume is equal to the total volume loss minus the volume loss due to mass loss. By calculating the plastic deformation in this thesis, the treated results can be accurately evaluated. This calculation method is first developed in this thesis.

3.2 Aims of thesis

The following questions are drawn from the analysis of the state of the art. It is the aim of this thesis to answer them.

- How do the characteristics of the sound field in a thin bubbly liquid layer depend on the consideration of bubble interactions?
- How do different standoff distances and driving currents affect the impact loads and surface enhancement on the treated workpieces?
- Is it possible to directly estimate plastic deformation in order to evaluate the cavitation process?
- How do the surface properties change depending on the parameters of ultrasonic cavitation peening?

3.3 Structure of the thesis

In order to answer the above open questions, the thesis is structured along the following lines:

Modeling of the sound field in a bubbly liquid

The cavitation bubbles caused by ultrasound in a small gap change the sound propagation in a bubbly liquid significantly when compared to the situation in a pure liquid. The bubbly liquid will be considered as a special medium in which there are interactions among bubbles. With the bubble interactions, some new characteristics of the sound propagation in the special liquid appear. Through the new parameters (sound speed and attenuation coefficient), the sound propagation distribution can be calculated. In this new

model, which is developed in Chapter 4, the sound field distribution model and the bubble interaction model are combined together.

Modeling of the optimal standoff distance

As a hypothesis, it is considered that the maximum impact is generated at the standoff distance which equals the diameter of the bubble. When the maximum bubble just contacts the two rigid walls, the bubble has the maximum volume. Thus, it can generate the highest impact on treated surface. On the other hand, different vibration amplitudes generate different bubble sizes, which means the one amplitude is corresponding to one optimal standoff distance. Based on this reasoning, the optimal standoff distances at different operation conditions will be calculated and compared to the experimental results in Chapter 5.

Experiments

Sonochemiluminescence is an effective method to study the cavitation fields in small gaps, which not only records the spatial distribution of the cavitation bubbles but also indicates the cavitation intensity. The material deformation caused by cavitation bubbles can be used to evaluate the ultrasonic cavitation effects. Using this method, the optimal standoff distance can be evaluated experimentally. In order to evaluate the impacts caused by cavitation bubbles on a treated surface, a piezoelectric force sensor is utilized to measure the impact loads. The results are analyzed in time domain and frequency domain. Mass loss and total volume loss are measured and calculated to deduce the plastic deformation. The different phases of ultrasonic cavitation erosion will be evaluated by roughness, hardness and surface profile in Chapter 6.

4 Ultrasonic fields in thin bubbly liquid layers

Ultrasonic cavitation peening is a surface treatment technology using the physical effect of ultrasonic cavitation at water-metal interface to improve surface properties. In order to obtain high impacts, a small standoff distance is necessary, usually less than 1 mm. The cavitation bubbles in the small gap significantly disturb the sound wave propagation and interact with each other. In this chapter, the sound field distribution model and the bubble interaction model are combined to investigate the distribution of sound fields with bubble interactions. The sound speed and attenuation coefficient are firstly calculated using the bubble interaction model. Then, the sound field in a bubbly liquid is calculated using the new parameters from the bubble interaction model. Finally, the cavitation field is compared to sonochemiluminescence experiments in various standoff distances and vibration amplitudes.

4.1 Modeling the sound field in bubbly liquids

During ultrasonic cavitation peening, the interactions between bubbles cannot be neglected due to strong cavitation intensity. However, one of the assumptions in previous models of sound field distribution is that the mutual interactions among bubbles are negligible. In the following sections, the sound speed and attenuation coefficient are introduced in order to describe the overall effect of bubble dynamics. These parameters are first calculated for the case of bubble interactions. Then, the model of the sound field distribution in a thin bubbly liquid layer is described.

A scheme of a typical ultrasonic cavitation peening system is shown in figure 4.1. In this configuration, the sound radiator is partly immersed in a liquid. The sound field can be simplified and described as following: the vibration of the horn tip which generates sound beam is piston-like. Then, cylindrical coordinates (R_s, ϑ, z) are introduced, where R_s is the radius. The origin of the coordinate is at the center of the horn tip, ϑ is the rotation angle, and z is the coordinate axis in the direction normal to the specimen surface. It is assumed that both the radiation surface at $z = 0$ and the specimen surface at $z = L$ are fixed rigid walls. The sound wave goes through the cavitation bubbles in z direction from the radiation surface. Then, it is reflected by the specimen surface and propagates towards the radiation surface again. The reflection of the wave goes on and on in the small gap

until the wave totally dissipates in the bubbly liquid. The other surfaces, e.g. the water surface, are considered as ideal pressure release boundaries. On these boundaries, all the sound waves go through it without any reflections.

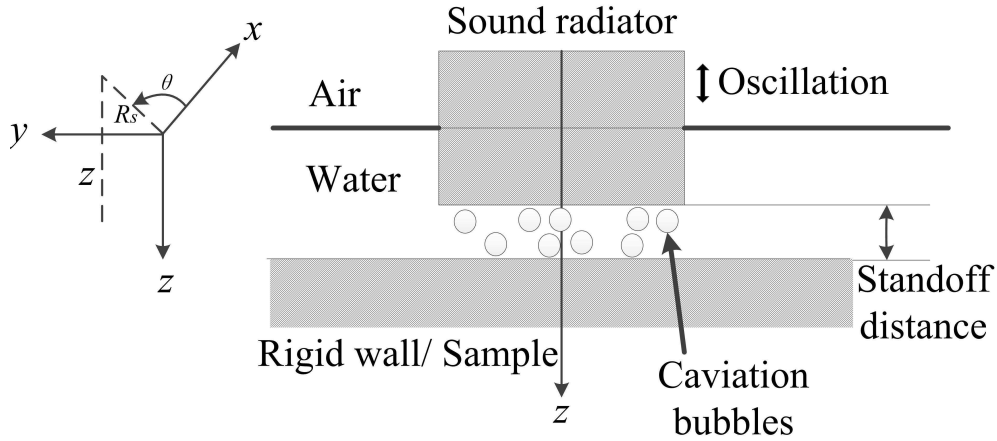


Figure 4.1: Scheme of an ultrasonic cavitation peening system.

In this chapter, the sound propagation models with and without the consideration of bubble interactions are compared. These two models were developed in [76, 77], but did not consider the change of the sound speed and the attenuation with the continuous change of the vapor volume fraction.

Before the investigation of the sound propagation in bubbly liquids, the propagation of the sound wave in a pure medium will be discussed. The generation of sound wave requires two basic conditions: one is a proper wave source, the other one is the presence of an appropriate medium of sound propagation. In order to describe the wave motion, the relationship between the sound pressure, the particle velocity, the changes in density and sound speed have to be understood. To simplify the research situation, the following assumptions are used: the viscosity and thermal conductivity are neglected; the ambient fluid velocity is neglected since the fluid velocity is much less than the speed of sound; the effects of the gravity force is neglected. By neglecting gravity and assuming the ambient fluid velocity is zero, the ambient pressure is constant. In this thesis, the sound pressure is only studied in frequency domain, since the sonotrode for ultrasonic cavitation peening is driven by a sinusoidal excitation. The wave equation in frequency domain can be described as Helmholtz equation [96]. With the consideration of bubble interactions, the bubbly liquid can be considered as a special medium. Thus, the Helmholtz equation can be described as:

$$\nabla^2 P + k_t^2 p = 0, \quad (4.1)$$

in which, P represents the ambient pressure, k_t is the complex wave number, t indicates the case of bubble interactions, ∇ is the gradient operator.

Combining equation 2.7 and equation 2.8 into equation 2.6, the complex wave number

with bubble interactions k_t is

$$k_t^2 = \frac{\omega^2}{c^2} + 4\pi\omega^2 \int_0^\infty \frac{af(a)}{\omega_0^2 - \omega^2 + 2ib\omega} da. \quad (4.2)$$

With this, the complex wave number k_t contains all information to calculate the propagation of sound wave in a two- phase medium. The real part represents the phase of the wave while the image part reflect the amplitude of the wave. Thus, the speed of the sound and the attenuation coefficient can be deduced [97]:

$$c_t = \frac{\omega}{\text{Re}(k_t)} \quad (4.3)$$

$$\alpha_t = \text{Im}(k_t) \quad (4.4)$$

A linear relationship of approximately $2 \times 10^{-9} / Pa$ between the bubble volume fraction β and the acoustic pressure amplitude p was determined in [98]. From equation 4.1, the primary sound pressure is calculated. Then, according to the linear relationship, the volume fraction is obtained. In this case, the complex wave number k_t can be calculated. Next, the new value of volume fraction can be obtained again from equation 4.1. Finally, after certain iterations, the final value is obtained [96]. Using the calculated values, the sound field in a thin bubbly liquid layer is calculated as described in the following paragraphs.

Firstly, the sound waves which are generated by a sound source are calculated in a infinite domain. The sound source is a flat disc and vibrates harmonically in a piston-like model in a direction normal to the disc surface. According to the equation 2.12, the integral has to be done at every point in the bubbly liquid to obtain the whole sound field. However, the circular symmetry implies that the pressure in any one plane perpendicular to the disc and passing through the origin is the pressure distribution of all such planes perpendicular to the disc and passing through the origin. Thus, the integral rendered in equation 4.5, which gives the pressure in the XZ plane, can be used to infer the pressure in the whole sound field. With the radius of the sonotrode tip R_s , there is a constraint $\sqrt{x^2 + y^2} \leq R_s$. The equation is deduced from equation 2.12 and used as a basis for the simulation in Section 4.2.

$$p(x_M, 0, z_M) = \frac{\rho\omega}{2\pi} \cdot u_0 \int_{-R_s}^{R_s} \int_{-\sqrt{R_s^2 - y^2}}^{\sqrt{R_s^2 - y^2}} \frac{e^{\{-k_t i \sqrt{(x_M - x)^2 + y^2 + z_M^2}\}}}{\sqrt{(x_M - x)^2 + y^2 + z_M^2}} dx dy \quad (4.5)$$

Based on the calculation of the sound field in the infinite domain, the way to simulate the sound propagation in a thin bubbly liquid layer is presented in the following paragraphs. In our case, the sound wave is generated by the sonotrode in contact with the

liquid medium. Then the wave propagates in a small gap. Due to the attenuation, the energy of the sound wave is eventually totally absorbed. Thus, the boundaries excepting the surface of the rigid wall are assumed to be ideal pressure release boundaries. On the surface of the rigid wall, the pressure is normal to the boundary. Since the standoff distance is very small, the liquid is considered as a liquid with a homogeneous distribution of cavitation bubbles. If there is no boundary, sound waves propagate from the sonotrode to the treated surface in a liquid. When an infinite rigid wall perpendicular to the sound beam is inserted, the wave propagation direction is converted backward by 180 degrees. In this situation, the original sound field is overlaid with the reflection sound field. The reflected sound waves are reflected again by the surface of the sonotrode. Therefore, the sound pressure is overlapped again and again to get the final distribution of the sound pressure.

In the next sections, the numerical and experimental evidences are provided to support the arguments in this section.

4.2 Simulation of sound field in thin bubbly liquid layers

This section focuses on the simulation of sound propagation and sound field distribution. To investigate the influences of bubbles on the sound wave propagation, the numerical simulations of the sound speed and the attenuation coefficient are first carried out. Then the sound field which is generated by a piston-like sound source will be calculated in an infinite domain. Based on this calculated results, the distribution of sound pressure in a bubbly liquid will be simulated using the method which was described in Section 4.1. The necessary parameters in the following simulations are given in Table 4.1.

Table 4.1: Values of the physical parameters used in the model.

Physical parameters	Unit	Values
Density	$\rho(kg/m^3)$	998.21
Surface tension coefficient	$\sigma(N/m)$	0.07236
Coefficient of viscosity	$\mu(Pa/s)$	0.001
Static pressure	$P_0(Pa)$	1.013×10^5
Vapor pressure	$P_v(Pa)$	2.34×10^3
Sound speed of the host liquid	$c(m/s)$	1500
Ratio of specific heats	γ	1.4
Gas thermal diffusivity	$D_f(m^2/s)$	2.4×10^{-4}

Figure 4.2 (a) illustrates the variations of the attenuation coefficient with and without interaction of bubbles. In the case without bubble interactions, the attenuation coefficient increases with the increase of the vapor volume fraction. If the case of bubble interactions is considered, the attenuation coefficient increases first and then decreases when the

volume fraction is about 1%. Regarding the sound speed in bubbly liquid, figure 4.2 (b) describes the decreasing tendency with the increase of the volume fraction. As shown in the figure, when the bubbles interact with each other, the sound speed becomes slower when the volume fraction is higher. Therefore, in the case of bubble interactions, the attenuation coefficient and the sound speed are smaller than in the case without bubble interaction, especially at the high vapor volume fraction. These simulation results will provide the basic values for the following modeling of sound field distribution in a thin liquid layer.

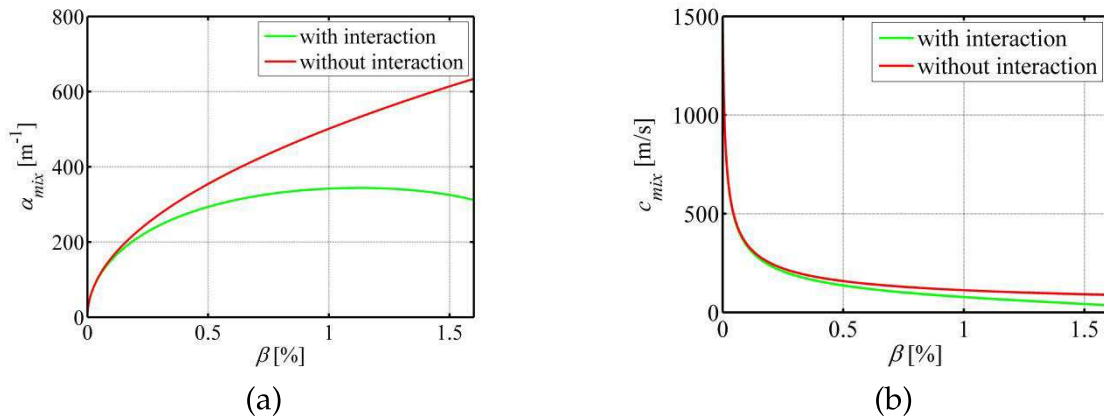


Figure 4.2: Variation of attenuation coefficient (a) and sound speed (b) with the increase of vapor volume fraction.

In general, when a sound wave travels through the liquid filled with cavitation, an increase in the local temperature is generated due to the bubble collapse. The scattering, absorption and reflection of the incident wave additionally contribute to the loss of intensity. Specifically, there are several mechanisms through which the energy of the wave can be lost. The first is the transformation of the mechanical energy into heat, as the wave works against the viscous forces which oppose internal motion in liquid. Secondly, as the cavitation liquid is non-homogeneous, energy loss can occur from the sound beam due to scattering of the sound. When the bubble concentration increases, the multiple scattering among different bubbles induces higher wave attenuation.

In the simulation of sound field in an infinite domain, the source of sound pressure is a sonotrode tip which is excited by a piezoelectric system with electrical input signals. The radius of the tip end is 2.5 mm. Moreover, the vibration amplitude of the sound source is proportional to the driving current with a relationship of approximately $120 \mu m/A$. The reason will be explained in the next section. Different driving currents cause different vapor volume fractions. In this model, it is assumed that the gas bubbles are homogeneously distributed in the liquid. According to figure 4.2, the speed of sound and attenuation coefficient change correspondingly. Due to the decrease of the sound speed in the bubbly liquid, the wave length λ can decrease to 3.4 mm when the vapor volume fraction is 1 %. As a result, the length of the sound near field N is 1.8 mm according to the near field equation of $N = R_s^2/\lambda$. Due to the effects of near field, the distribution of sound pressure in a small gap is complex. In the following simulations, the distribution of sound pressure

in a bubbly liquid in an infinite domain is calculated.

The vibration amplitudes of 25 μm , 30 μm , 35 μm and 40 μm , which correspond to the driving currents of 0.208 A, 0.250 A, 0.292 A and 0.333 A, are investigated, since a high vibration amplitude is required during ultrasonic cavitation peening. In the simulations, the wave number k_t is already calculated utilizing equation 4.2. The radius and height of the calculated spatial volume are 5 mm and 8 mm, respectively. In figure 4.3, the sound pressures are mapped using equation 2.12. It can be seen that the highest sound pressure always occurs at the tip end of the sonotrode and the distribution is not uniform due to the effects of the near field. With the increase of the driving current, a high volume fraction is generated, producing a high attenuation.

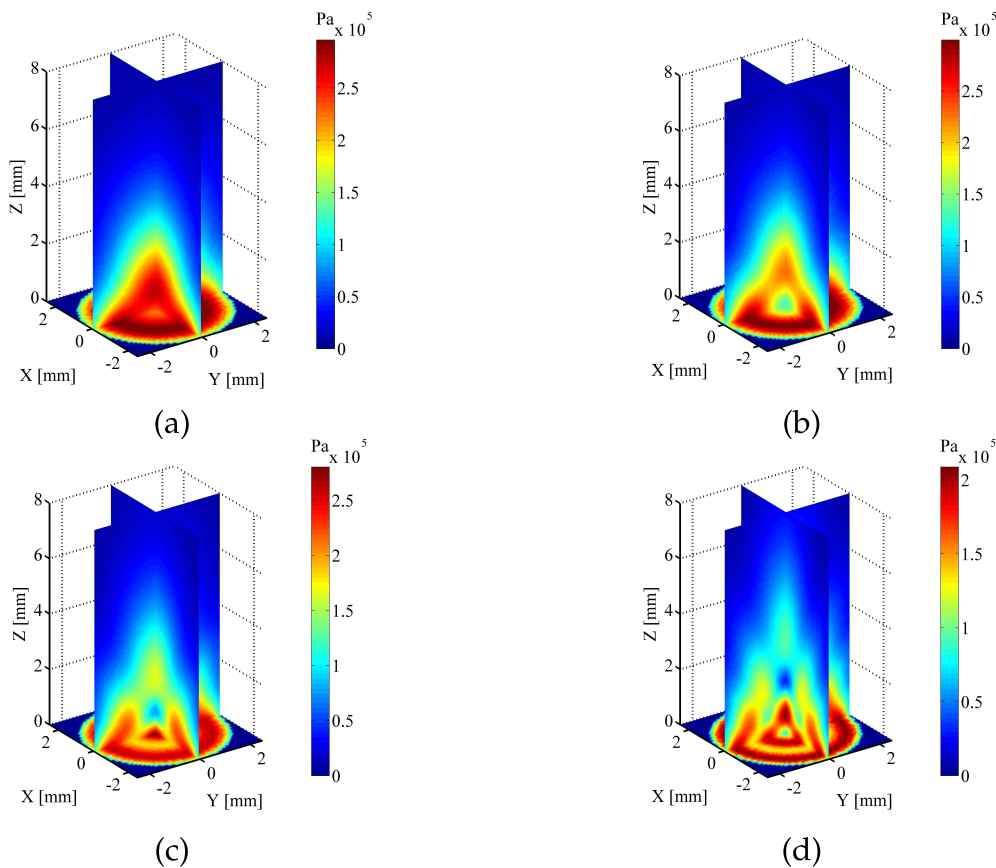


Figure 4.3: Pressure fields for different driving currents at the resonance frequency of 23 kHz: (a) 0.208 A, (b) 0.250 A, (c) 0.292 A and (d) 0.333 A.

As a result, the sound speed will decrease, as shown in figure 4.2. Because the rate of decline in sound speed is greater than the rate of increase in vibration amplitude, the sound pressure near the end of the sonotrode decreases although the vibration amplitude increases. In the distance of 8 mm, the sound pressure decreases gradually to zero due to high attenuation. Even if the simulation is more than 8 mm, the sound pressure is still equal to zero. Thus, the simulation distance is sufficient for the following sound pressure analysis.

In addition to the local sound pressure distribution, the average sound pressure is also

important to investigate. The average pressure in the simulation means that the sum of the sound pressures at every calculated point in the XZ plane along Z direction are divided by the number of the points. The distribution of the average sound pressure can, in brief, show the distribution of cavitation bubbles. The sound pressures in the XZ plane which are shown in figure 4.3 can be averaged and illustrated, see figure 4.4. The average pressure decreases with the increase of the driving current. The sound pressure is strongest at the center ($R_s = 0$) and at the edge of the calculated surface the average pressures are almost the same. According to the average sound pressure distribution, the average bubble distribution can be evaluated, since the higher pressure generally generates the stronger cavitation intensity. The distribution of the average sound pressure will be compared with the mean cavitation intensity in the following experiments.

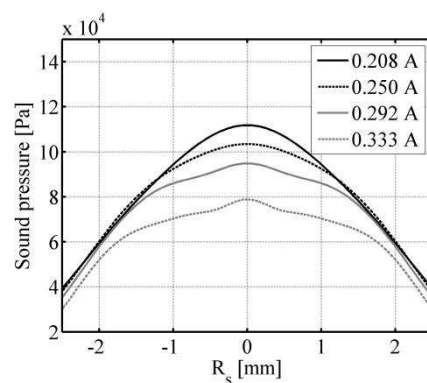


Figure 4.4: The average sound pressure at different driving currents.

Based on the investigation of the sound field in an infinite domain, the distribution of the sound pressure will be studied. Figure 4.5 shows the distribution of sound pressure between the sonotrode and the workpiece at the standoff distance of 0.3 mm (top), 0.7 mm (middle) and 1.3 mm (bottom) and at the driving current of 0.333 A. The figure shows that the highest sound pressure occurs at the central regions on the sonotrode tip and the workpiece surface. The strongest cavitation intensity is also expected to be generated at the central area of the treatment surface. Nevertheless, the distribution of sound pressure at the standoff distance of 0.3 mm is more even than that at the other standoff distances. At this standoff distance, the growths and the collapses of the cavitation bubbles are affected by the small gap. When the standoff distance increases to 0.7 mm, the sound pressure on the workpiece decreases and the distribution of the sound pressure becomes uneven, but the cavitation intensity is expected to be the largest. It is because there is no gap limitation and the energy loss is less compared to that at the standoff distance of 1.3 mm. Thus, the standoff distance of around 0.7 mm is considered as the optimal standoff distance. From these figures, the distribution of sound pressure on the workpiece surface can be directly obtained instead of the further calculations. The distributions will be analyzed in the following.

The distributions of sound pressures in thin bubbly liquid layers have been shown in the above descriptions. It is also essential to explore the distribution of sound pressure on a rigid wall, as the one of the aims of this thesis is to study the effects of cavitation on the

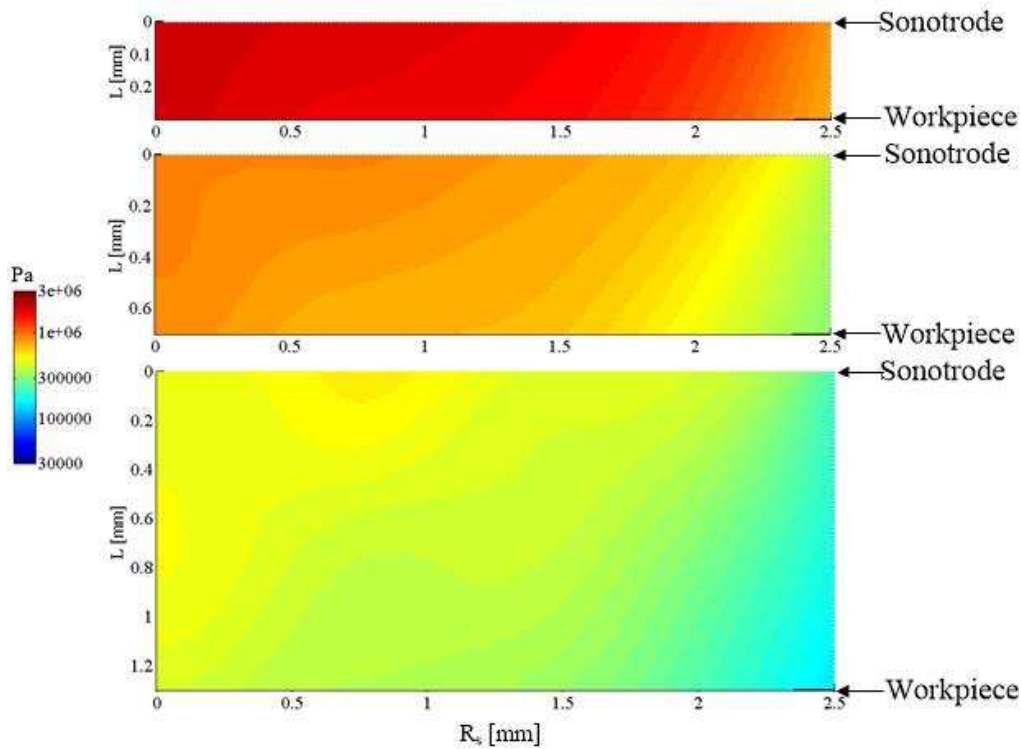


Figure 4.5: The distribution of sound pressure in the gap width of 0.3 mm (top), 0.7 mm (middle) and 1.3 mm (bottom) at the driving current of 0.333 A.

treated surface. From the investigation of the sound pressure distribution on a rigid wall, the cavitation distribution on the wall can be estimated.

Figure 4.6 shows the sound pressure on the rigid wall. In the figure, the z -axis represents the sound pressure on the rigid wall. The X axis and the Y axis represent the standoff distance and the radius of sonotrode tip.

There are two cases about low and high driving current: one at the driving current of 0.208 A (figure 4.6 (a)), and the other one at the driving current of 0.333 A (figure 4.6 (b)). It can be seen that the sound pressure is the strongest at the central area of the calculated surface. At the low driving current, the sound pressure is higher than that at high driving current due to the change of sound speed and vibration amplitude as mentioned above. The sound pressure decreases with the increase of the standoff distance. The sound pressure decreases much more rapidly in a small standoff distance than in a large standoff distance.

Higher sound pressure on the rigid wall causes stronger cavitation, which has major effects on the surface treatment. Thus, it is essential to investigate the maximum sound pressure on the rigid wall in the simulations. As the supplementary information of figure 4.6, figure 4.7 shows the maximum sound pressure on the rigid wall at four different driving currents. The maximum sound pressure on the rigid wall decreases with the increase of the standoff distance. In the range of the small standoff distance, the maximum sound pressure decreases rapidly while it decreases slowly in the range of the large stand-

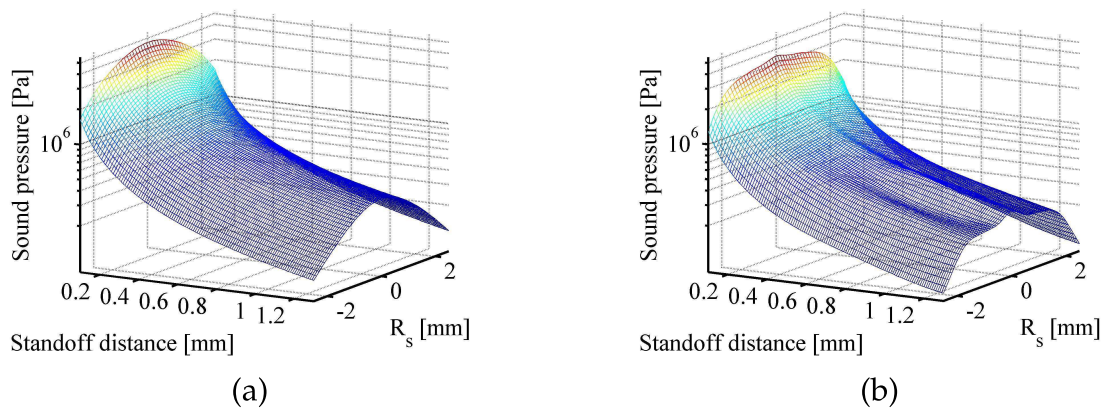


Figure 4.6: The sound pressure on a rigid surface at driving currents of (a) 0.208 A and (b) 0.333 A.

off distance. When the standoff distance is from 0.7 mm to 1.2 mm, the sound pressure is larger at the driving current of 0.333 A than that at the driving current of 0.292 A. In other considered conditions, the lower driving currents still cause the higher sound pressure under above investigation condition.

In order to investigate this deeply, the distribution of local sound pressure on the rigid wall is compared in different driving currents (0.087 A, 0.125 A, 0.167 A, 0.208 A, 0.250 A, 0.292 A and 0.333 A). Figure 4.8 shows the local distribution of sound pressure on the rigid wall at the standoff distances of 0.3 mm (a), 0.7 mm (b), and 1.3 mm (c) when the driving currents are 0.087 A, 0.125 A, 0.167 A, 0.208 A, 0.250 A, 0.292 A and 0.333 A, respectively. It can be seen that at the edge of the available treated surface, the sound pressure is much smaller than that in the central area. At the central area, the sound pressure increases and then decreases again with the increase of the driving current. The distribution of sound pressure becomes more and more complicated when the driving current increases. As shown in the figures there are two peaks beside the peak at the center, which means that a ring area with high sound pressure can appear in the view of XY plane. This is because when the driving current increases, the sound speed decreases, which leads the wave

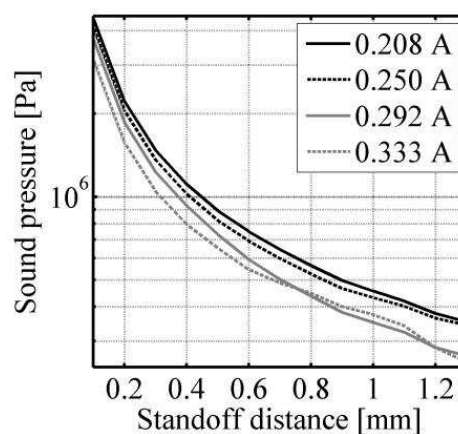


Figure 4.7: Maximum sound pressure at four different driving currents.

number to increase. As a result, the side lobes of the sound beam appear.

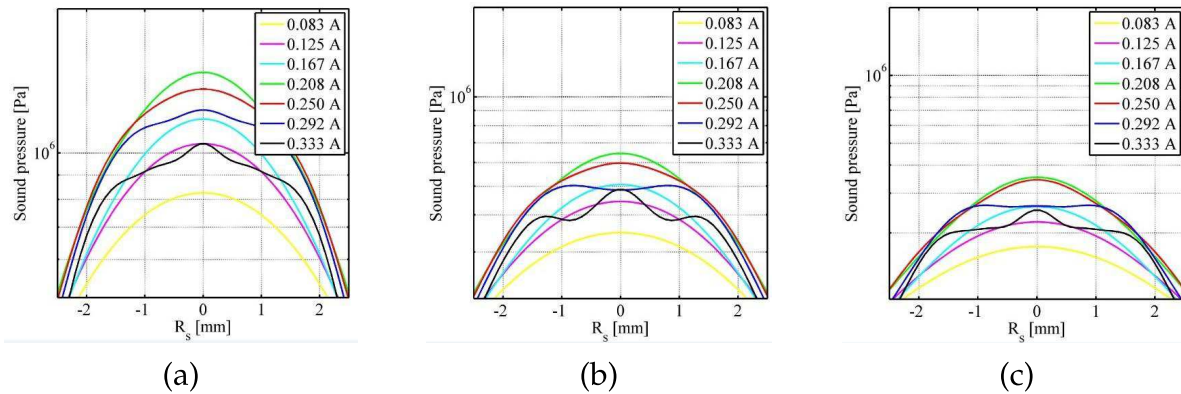


Figure 4.8: The distribution of the local sound pressure at the standoff distances of 0.3 mm (a), 0.7 mm (b), and 1.3 mm (c).

Through the above analysis, the results are summarized as follows: the sound pressure on the rigid wall decreases with increases in the standoff distance; at the same standoff distance, the maximum sound pressure increases first and then decreases when the driving current increases from 0.083 A to 0.333 A. Among the investigated input currents, a value of 0.208 A is the largest sound pressure level in all cases. In the next section, these simulation results will be validated by sonochemiluminescence experiments.

4.3 Experimental determination of the cavitation distribution utilizing sonochemiluminescence

Sonochemiluminescence (SCL) is a phenomenon of light emission which is produced by the OH^- and the sonochemically oxidizes luminal. Thus, the spatial distribution of cavitation bubbles in an aqueous solution can be indirectly shown by the SCL method. In this section, the experimental setup and the methods for the investigation of cavitation bubble distributions are introduced, including the transducer with its control system, experimental methods for sonochemiluminescence and the photography method for cavitation bubbles.

4.3.1 Experiments

Figure 4.9 shows the experimental setup for the investigation of the SCL in small gaps. The transducer was immersed in a liquid which was contained in a cylindrical glass container. A Nikon D3100 camera was fixed below the bottom of the glass container to capture the SCL phenomenon. The transducer used here is a classical sandwich transducer designed and manufactured at the Institute of Dynamics and Vibration Research. It is composed of a titanium alloy tail-mass, four PZT piezoelectric ceramic rings and a head

mass in titanium alloy. A titanium screw was used to assemble and prestress the transducer. The transducer is operated in its $\lambda/2$ mode at the first longitudinal resonance frequency at about 23 kHz. A sonotrode with $\lambda/2$ length is connected with the transducer. The diameter of the sonotrode tip is 5 mm. The transducer was driven at resonance by a digital phase control unit (IDS Digital-Phase Control 500/100k) [99] with a power amplifier QSC 4050 (manufacturer). Both phase feedback and current feedback control were used for the investigations. Using the digital phase control unit, the driving current, phase between driving current and voltage, impedance and power can be recorded during cavitation process. The ultrasonic horn was partly submerged in water. The distance between the water surface and the tip end of the horn was always maintained at 10 mm. The changes of standoff distances were measured by a displacement sensor (Solartron LVDT AS/150).

When the cavitation bubbles are generated, the vapor volume fraction changes and the impact loads on the end of the sonotrode occur. This significantly affects the resonance frequency and vibration amplitude of the transducer. To avoid the change of working parameters of the transducer, a control system is necessary. Figure 4.10 illustrates the equivalent circuit of a transducer with a load at the resonance frequency. In the electrical part, C_p , U and i represent capacitance, driving voltage and current, respectively. In the mechanical part, d , c_t , m and V are modal damping, stiffness, mass and the velocity of the transducer tip, respectively. α is the electromechanical coupling coefficient. In the

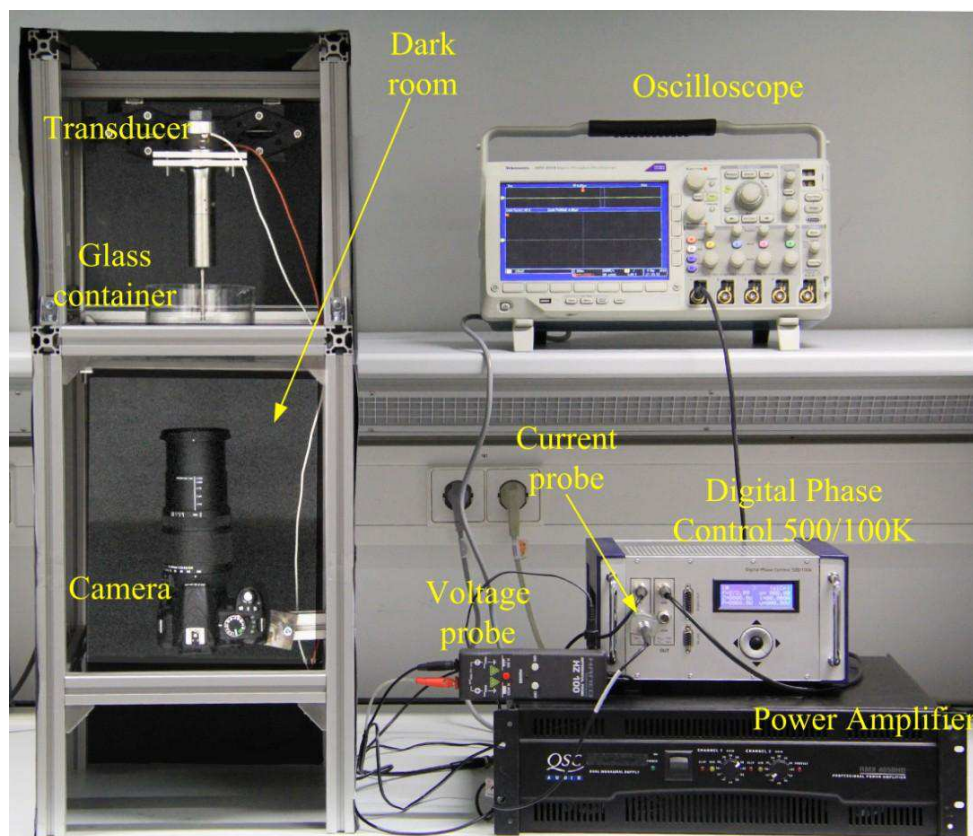


Figure 4.9: Experimental setup for SCL.

equivalent circuit, it is proposed that the liquid load impedance on the horn tip is Z_L . The transducer mechanical impedance, an intrinsic property of the transducer, is fixed once the transducer is assembled. When a transducer is driven exactly in its resonance frequency, the impedances from c_t and m cancel each other. In this case there is nearly no current going through C_p , which means that the driving current is proportional to the tip velocity. This requires a precise preliminary identification of the parallel capacitor C_p . Using this parameter, the phase of the mechanical admittance was calculated internally with the consideration of the compensation of the parallel capacitor C_p and used as the input variable of the phase control loop [100, 101]. The velocity amplitude is only proportional to the displacement amplitude of the transducer's tip when excited harmonically.

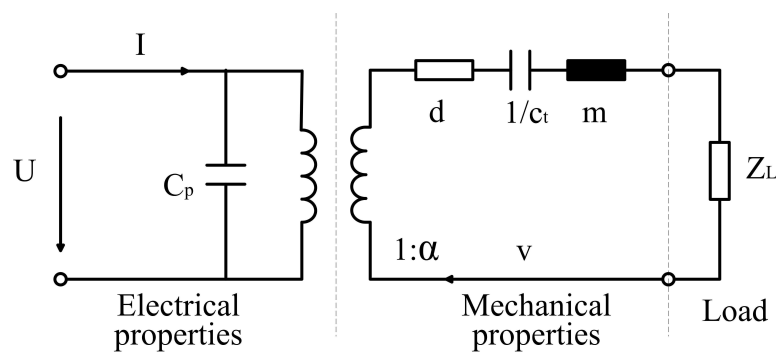


Figure 4.10: Equivalent electro-mechanic circuit of the resonant transducer with load.

Therefore, when in resonance, the displacement amplitude \hat{X} is proportional to the current amplitude \hat{I} . For this measurement in the unloaded case, a relationship of approximately $120 \mu\text{m}/\text{A}$ could be determined. The vibration velocity at the center of the horn tip was measured by a one point 3D vibrometer (Polytec CLV 3000). The digital phase control unit can make the driving current steady with various loading. A current probe (Tektronix P6021) was used to obtain the current values.

Figure 4.11 shows an example of the different working parameters (power, phase, current, impedance and frequency) in control at the driving current of 0.333 A. The transducer was controlled at the resonance frequency. At the beginning of ultrasonic cavitation, all the parameters had a transient change and then remained almost unchanged. The resonance frequency decreased slightly due to the temperature effect on the transducer.

The experimental liquid of SCL was made of luminol ($\text{C}_8\text{H}_7\text{N}_3\text{O}_2$) (0.004 mol/L), NaOH (0.1 mol/L) and water. During the experiments, the standoff distance was varied between 0.1 mm and 1.3 mm with an interval of 0.1 mm. The driving currents are 0.208 A, 0.250 A, 0.292 A and 0.333 A, respectively. At each standoff distance, four photos were taken corresponding to different driving currents. SCL images were captured by the camera (18-250mm/f3.5-6.3, ISO400, focal length 262 mm) with an exposure time of 90 s. Since the light caused by SCL is weak and can not be seen by naked eyes, a long exposure time is necessary to obtain a high quality photo. All of the experiments were carried out in a dark room. Since the sonotrode tip is a cylindrical, the available area of the SCL photo is a circular region. The SCL images were processed by the software *ImageJ*, a picture

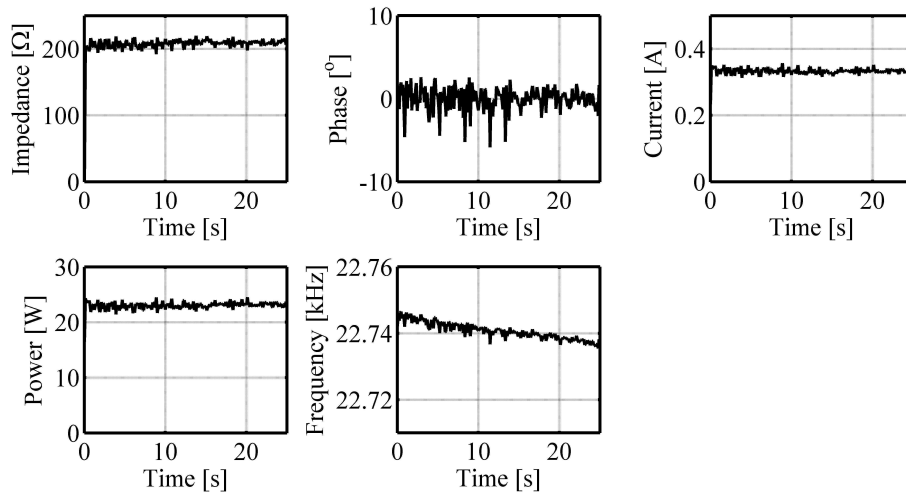


Figure 4.11: The different working parameters at the driving current of 0.333 A.

processing software. Accordingly, it is a commonly used and easy to operate software for processing SCL figures. The intensity of cavitation can be reflected by the relative light intensity; thus by the analyzing the gray value of the photos, the spatial distribution of the cavitation field can be obtained. In order to reduce the distraction of other light from the surroundings, the relative light intensity is subtracted by the background light intensity. For every photo, the surrounding light intensities in four different areas beyond the available area were calculated as the average value. The mean distribution of the light intensity in the calculation areas can be directly obtained by *ImageJ*, which is shown in figure 4.12 (a). The available light intensity in the photos was plotted along the diameter as shown in figure 4.12 (b). In order to obtain the average results, the photos were rotated every 45 degrees and then the average values were calculated.

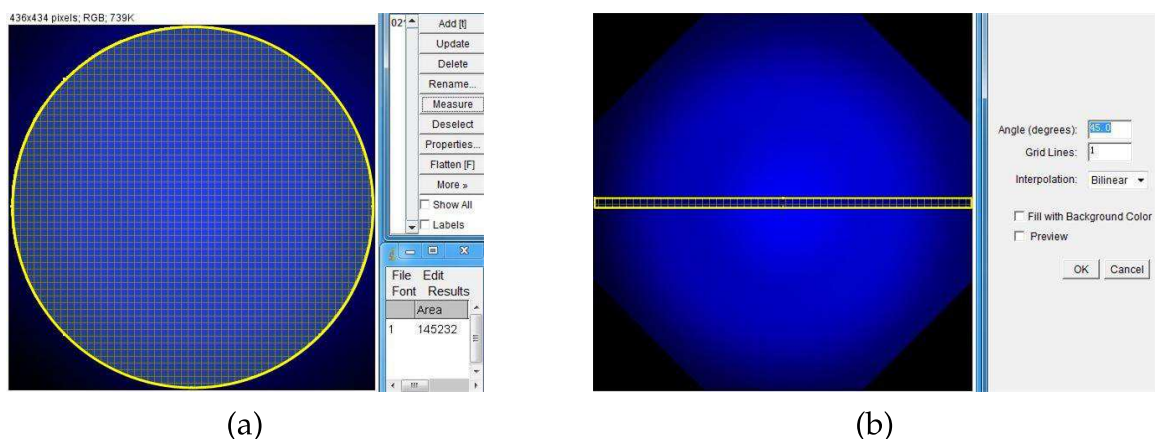


Figure 4.12: The method of the data process by the rotation of the photo: mean distribution (a) and local distribution (b).

In order to directly observe the distribution of cavitation bubbles, a high-speed camera (Phantom v710) was used to capture images of the bubbles at the standoff distance of 0.3 mm. The high-speed camera was also fixed below the bottom of the glass container. The exposure time used here was 10 μ s. The window size and the corresponding frame

rate are 1028×1028 and 1000, respectively. In this relatively low frame speed, the captured area is large. Thus, more cavitation bubbles can be captured in one photo, which is beneficial for the statistics and analysis of bubbles. Owing to the small size of cavitation bubbles, it was necessary to assemble a magnification system with the camera. f1.4 Pentax lenses were used in the present work and provided a magnification of $18\times$. With these settings, the bubbles can be seen clearly and more bubbles can be captured at once. A custom-made light (XENON NOVA 300 cold light fountain) source provided sufficient illumination for these experiments.

Figure 4.13 (a) shows the bubbles at the driving current of 0.208 A while figure 4.13 (b) shows the bubbles at the driving current of 0.333 A. Most of the bubbles at the low driving current are larger than those at the high driving current, while the number of bubbles at low driving current is much smaller than that at high driving current. Therefore, by increasing the driving current, the bubble size decreases slightly but the bubble density increases substantially. This leads to the decrease of the concentration of luminol in the cavitation liquid, since the vapor volume fraction increases and there is no luminol solution in the cavitation bubbles.

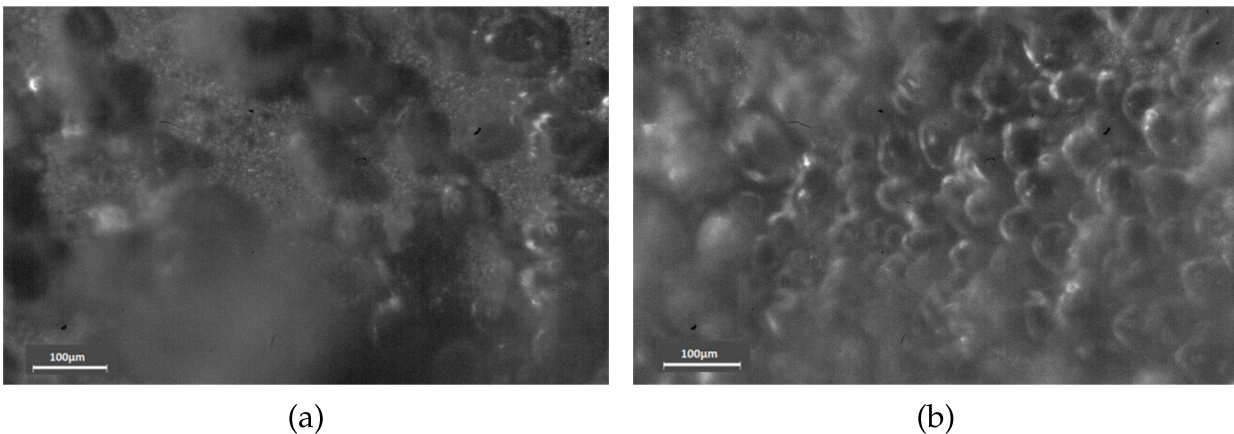


Figure 4.13: The distribution of cavitation bubbles at driving currents of (a) 0.208 A and (b) 0.333 A.

4.3.2 The mean distribution of cavitation bubbles

From the photographs captured by the high-speed camera, it can be seen that the bubble density increases with the increase of the driving current, which will provide some evidences for understanding SCL experimental results. To evaluate the cavitation intensity in small gaps, the SCL experiments were carried out at five different driving currents: 0.125 A, 0.208 A, 0.25 A, 0.292 A and 0.333 A. The investigation at the current of 0.125 A is helpful to know the SCL without sufficient input power. In the experiments, the standoff distances were changed from 0.1 mm to 1.3 mm with an interval of 0.1 mm. The experimental results are shown in figure 4.14, in which the mean light intensity distribution at different standoff distances and driving currents is illustrated. The mean light intensity, i.e. the average light intensity in the area of the circle with the radius of 2.5 mm, is plot-

ted. The SCL relative intensity represents the deference between the real intensity and the background intensity. The X -axis represents the standoff distance and the Y -axis the SCL relative intensity. In the following paragraphs, the effects of the driving current and the standoff distance on the cavitation intensity will be explained using the results of SCL experiments.

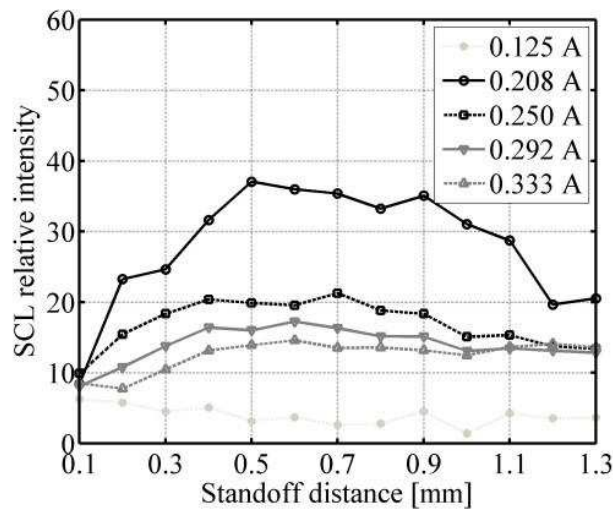


Figure 4.14: Mean light intensity distribution at different standoff distances and driving currents.

Firstly, the variations of the cavitation intensity at different driving currents will be analyzed. When the driving current is 0.125 A, the SCL relative intensity fluctuates in the range between 1 and 6. The value of the SCL relative intensity at this low driving current is smaller than that at all other high driving currents, since low driving current does not have enough energy to generate strong cavitation. With an increase in the driving current to 0.208 A, the SCL relative intensity increases rapidly and becomes the strongest almost at each standoff distance. When the driving current increases to 0.250 A, the value of the SCL relative intensity decreases. With continuing to increase the driving current, the value of SCL relative intensity keeps decrease. This is because with high driving currents many cavitation bubbles are produced in the gaps, leading to a high gas void fraction. This phenomenon has been validated by the high-speed figures shown in figure 4.13. Therefore, the concentration of the luminol in the solution decreases. Although the cavitation intensity is strong enough, the value of the SCL relative intensity is weak due to the low concentration of luminol in solution. The phenomenon that the SCL relative intensity increases and then decrease with increasing the cavitation intensity was also reported previously [102, 103].

Secondly, the SCL relative intensity is also much related to the standoff distance. At the driving current of 0.125 A, the SCL relative intensity is weak and less influenced by the variation of the standoff distance. With an increase in the driving current to 0.208 A, the value of SCL relative intensity increases to a peak value of 37 and then decreases. The peak occurs at the standoff distance of 0.5 mm. When the standoff distance is small, the

growths and collapses of cavitation bubbles are limited by the small gaps. Thus, lower cavitation intensity causes less SCL light emission. With the increase in the standoff distance, the dynamics of cavitation bubble are no longer limited in a small gap, which results in considerable energy emission. However, the continuous increase in the standoff distance does not change the vibration amplitude and there are many cavitation bubble existing in the gap. Due to the attenuation caused by the cavitation bubbles, the cavitation intensity near the observed side is weaker than that near the transducer surface. The light caused by SCL is reflected, scattered and absorbed by the bubbles near the surface of the glass. With the same generated energy, the light of SCL is lost when it travels through the cavitation bubble layers. Thus, the value of the SCL relative intensity decreases when the standoff distance becomes larger than 0.5 mm. However, the light of SCL caused by the bubbles near the glass surface can be totally captured and those bubble should mainly affect the surfaces of treatment workpieces. The similar tendency also occurs at the driving current of 0.250 A, 0.292 A and 0.333 A.

Overall, when the input energy is low, the SCL relative intensity is as weak as the cavitation intensity. When the input energy is great enough, the SCL relative intensity is great relative to the standoff distance. In general, there is a strong SCL relative intensity existing with the variations of standoff distance when it is observed from the bottom.

4.3.3 The local distribution of cavitation bubbles

The mean distributions of cavitation bubbles at different conditions have been introduced above. However, it is still essential to investigate the local distributions of cavitation bubbles, since the near sound field results in the inhomogeneous distribution of cavitation bubbles in small gaps. The local distribution can be illustrated by a "linescan" which is through the middle of the SCL image as shown in figure 4.15, since the available area of the image is circular symmetry. The local distribution of the cavitation is studied in the following by analyzing the case at the driving current of 0.208 A and the standoff distance of 0.7 mm. It can clearly be seen that the light intensity is the strongest in the center area. There is a ring area where the cavitation intensity is stronger than that in the edge region but lower than that in central region.

The distributions of the SCL relative intensities at different standoff distances and different driving currents are shown in figure 4.16. Figure 4.16 (a) shows the distribution of SCL relative intensity at the driving current of 0.208 A. In the figure, the X and Y axis are the measurement radius R_s and the standoff distance, respectively. As shown in the figure, the strongest SCL relative intensity is located at $R_s = 0$. In the position of the same radius, the SCL relative intensity increases to a peak at the standoff distance of 0.7 mm, and then decreases again. Taking into account the distribution of SCL relative intensity along with the radius, the tendency appears to go down from the center of $R_s = 0$. As shown in the previous simulation results, the sound pressure is stronger at the center and is stronger than in other areas. Thus, the strongest cavitation is caused by the strongest sound pres-

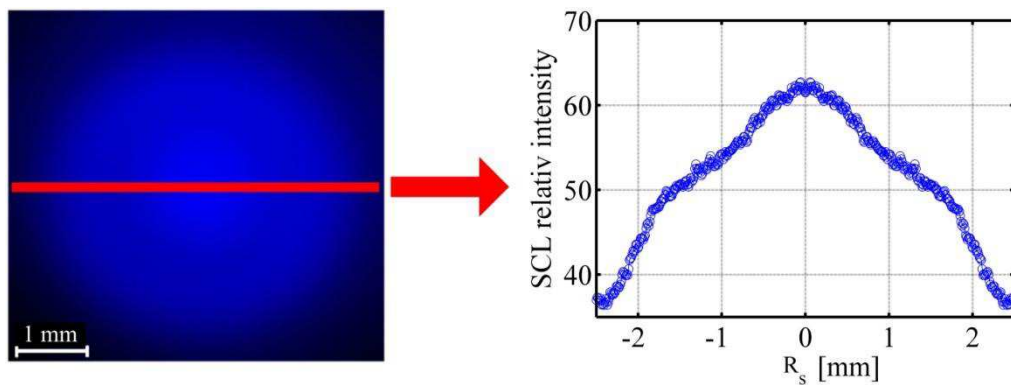


Figure 4.15: Photo of SCL and light intensity distribution at the driving current of 0.208 A and the standoff distance of 0.7 mm.

sure, which is reflected by the SCL relative intensity. The maximum SCL relative intensity means the strongest cavitation intensity, which can cause the strongest impact during the treatment. The strongest cavitation intensity occurs in the range of the standoff distance between 0.6 mm and 0.8 mm. The reason was explained in the last section.

The SCL relative intensities at the driving current of 0.250 A, 0.292 A and 0.333 A are also illustrated in the figure 4.16. It can be seen that there is a similar tendency as that at the driving current of 0.208 A. The strongest SCL relative intensity is located at $R_s = 0$ and there is a peak of the SCL relative intensity with increasing the standoff distance.

The differences are: the standoff distance corresponding to the strongest SCL intensity is larger than that at low driving current; the peak value at low driving current is higher than that at high driving current; the ring area where the SCL relative intensity is stronger is not as obvious as that at the low driving current. These changes could be caused by the second Bjerknes forces, which cause bubbles to repel each other. This is because when the bubbles have the similar size and movement, the Bjerknes forces appear mutually repellent. The larger bubbles generate the larger Bjerknes forces. If the Bjerknes force is weak, the distribution of cavitation bubbles will nearly agree with the distribution of the sound field. When the cavitation intensity becomes stronger, the ring area is not obvious anymore due to the larger repulsive forces.

From the above description, the effects of different standoff distances on the SCL relative intensity are clearly illustrated. However, the distributions of cavitation bubbles at a fixed standoff distance but different driving currents are still required for a complete understanding of the issue. Figure 4.17 shows the local distribution of the SCL relative intensity at the standoff distances of 0.3 mm (a), 0.7 mm (b), 1.3 mm (c) when the driving currents are 0.125 A, 0.25 A, 0.292 A and 0.333 A, respectively. These figures are supplementary to figure 4.16. It can be seen that when the standoff distance is 0.3 mm, the SCL relative intensity increases and then decreases with the increase of the driving currents with the similar distribution trend, which continues decreasing from the center. When the standoff distance is small, the bubble is not spherical due to the limitation of the walls. The limitation decreases the cavitation intensity, which leads to a weak SCL intensity.

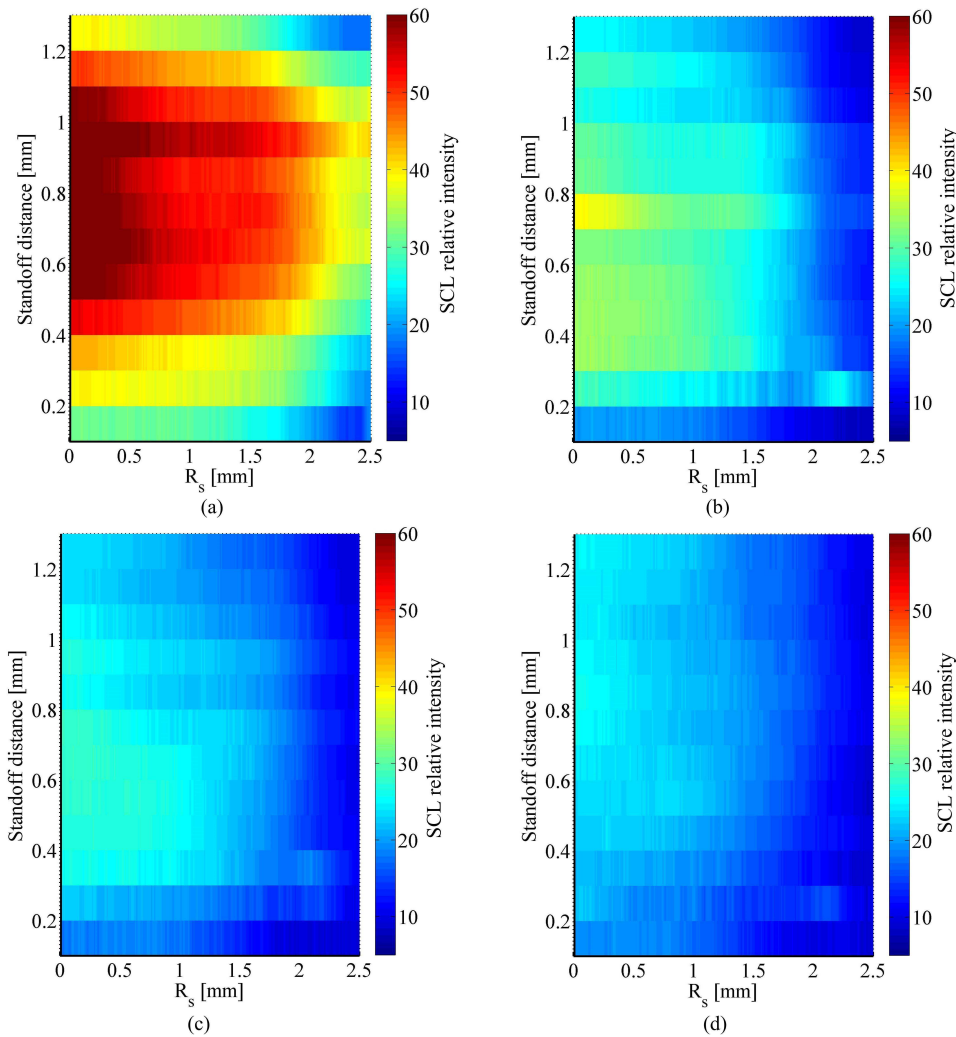


Figure 4.16: SCL relative intensity distribution at driving current of (a) 0.208 A, (b) 0.250 A, (c) 0.292 A and (d) 0.333 A.

When the standoff distance is increased to 0.7 mm, the local distributions of the SCL relative intensity at different driving currents result in noticeable changes. This is due to the effects of side lobes in the near field.

The intensity decreases from $R_s = 0$, then slightly increases and finally decreases along with the increase of the R_s . The increase shows a ring area of SCL light when it is observed from the SCL photo. This is because the effects of the side lobes of the sound beam increase. However, the main lobe is still dominant, which leads to the strongest SCL relative intensity in the central region. At this standoff distance, almost all the curves have a similar tendency and a higher SCL relative intensity compared to other two figures in figure 4.17. If the standoff distance increases to 1.3 mm, the local distribution of SCL relative intensity is similar to that at a standoff distance of 0.3 mm.

In this chapter, to verify the intensity and the distribution of cavitation bubbles in the small gaps, a sound propagation model in the bubbly liquid is built and then the SCL

experiments were carried out to provide the evidences. In the model, the effects of the bubble interactions on sound propagation and distribution are taken into consideration. Compared to the model without bubble interactions, the sound speed and the attenuation coefficient at the high volume fraction decrease significantly. Due to the effects of the sound speed and the attenuation coefficient, the sound pressure first increases to a peak at the driving current of 0.208 A and then decreases with increasing the driving current from 0.087 A to 0.333 A with the interval of 0.042 A (the vibration amplitude from 10 μm to 40 μm with the interval of 5 μm).

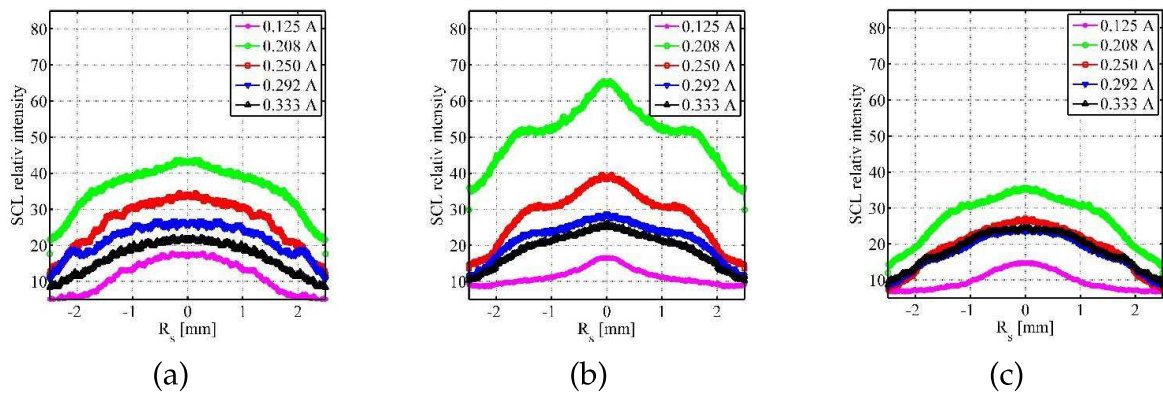


Figure 4.17: The local distribution of SCL relative intensity at standoff distances of (a) 0.3 mm, (b)0.7 mm, (c)1.3 mm.

Then the mean SCL relative intensity was investigated at different driving currents and standoff distances. It is found that the higher driving current causes the lower SCL relative intensity while the strongest cavitation intensity occurs at the standoff distances between 0.5 mm and 0.7 mm. For the local distribution of cavitation bubbles, the SCL experiments show that the strongest cavitation intensity occurs at the center of the treated region. Compared to the calculation results, there is a difference at the range of standoff distance between 0.1 mm and 0.4 mm because of the limitation of bubble dynamics by the small gaps. The violent cavitation reaction always concentrate at the vicinity of $R_s = 0$ and sometimes the ring phenomenon occurs. However, the primary tendency of the cavitation intensity and distribution can be verified utilizing both the model and the SCL experiments.

5 Investigation of the impact loads caused by cavitation bubbles in small gaps

The distribution of cavitation bubbles in a thin liquid layer was studied in Chapter 4. However, during ultrasonic cavitation peening, the greatest concern is not about bubble size distribution but on the impact loads generated on the workpiece surfaces. The impact loads are influenced by many parameters, such as frequency, input power, temperature, initial bubble size, standoff distance. Excepting the standoff distance, the effects of all other parameters on the workpiece surfaces were extensively investigated in previous studies as reported in Chapter 2. In this chapter, the influences of different standoff distances on the workpiece surfaces are theoretically investigated prior to experimental investigations. Then, the numerical results are validated on the basis of the volume of the pits caused by the impact loads. This work was partly published in my own contribution [104]. These measurements are easy to achieve but this result only reflects the surface deformation. Hence, a piezoelectric sensor is used as an additional method to investigate the impact loads caused by the collapses of cavitation bubbles.

5.1 Numerical investigation of the bubble characteristics

Cavitation phenomena have been investigated for over a century. It is well known that when the vibration frequency becomes high, more power is required to generate cavitation. In this case, the ultrasonic frequency near 20 kHz is more beneficial for ultrasonic cavitation peening. The impact loads decrease with increase the liquid temperature if the other conditions remain unchanged. More cavitation bubbles and stronger cavitation intensity are caused as the input power increases. Those factors, except the effect of the standoff distance, can be well explained by existing theories and experimental investigations.

During the ultrasonic cavitation peening process, a small standoff distance between the workpiece surface and the ultrasonic horn tip is generally utilized to avoid undesired energy loss. The undesired energy loss is mainly from the attenuation of wave propagation in bubbly liquids. Even a small change in the standoff distance significantly affects the dynamics (growth and collapse) of cavitation bubbles. Consequently, the capability of ultrasonic cavitation peening greatly changes with the variations of standoff distances due to the attenuation of wave propagation and the limitation of bubble dynamics by

the small gap. The aim of this section is to provide a theoretical model to analyze the cavitation capability at different standoff distances.

5.1.1 Different cavitation bubble sizes in a small gap

For a single cavitation bubble, there are three different shapes in a small gap, as shown in figure 5.1. The three cases can be divided by $w^* = L/R_m$ the ratio between standoff distance L and maximum bubble size R_m (radius). In the first case ($w^* < 2$), the bubble growth and collapse are limited by the small gap. However, the larger bubble volume still generates a stronger impact load on a workpiece surface. The impact caused by the collapse of cavitation bubbles decreases with the decrease of w^* and the micro-jet is dominant when the impact is produced. It has been confirmed that the amplitude of the impact peak in the case of $w^* = 1.61$ is larger than that in the case of $w^* = 1.25$ [37].

In the second case ($w^* = 2$), the diameter of the maximum bubble is the same as the standoff distance, which means that the bubble wall contacts both the workpiece surface and the sonotrode tip. In this case, the impact force on the workpiece is mainly from the micro-jet instead of the shock wave. In general, the impact caused by the shock wave is smaller than that caused by micro-jet under the same conditions [31].

In the third case ($w^* > 2$), the maximum diameter of the bubbles is smaller than the standoff distance. It was found that the cavitation bubble has a spherical form at the stage of expansion at $w^* = 2.2$ [51]. Even if the standoff distance is small, high attenuation will cause the sound pressure to decrease rapidly. Thus, with the increase of the standoff distance, the sound pressure near the workpiece surface decreases. When the standoff distance is less than a quarter wave length, the sound pressure amplitude will decrease with increasing the standoff distance. Correspondingly, the bubble size becomes smaller, which results in the smaller impact from a bubble collapse on the workpiece surface.

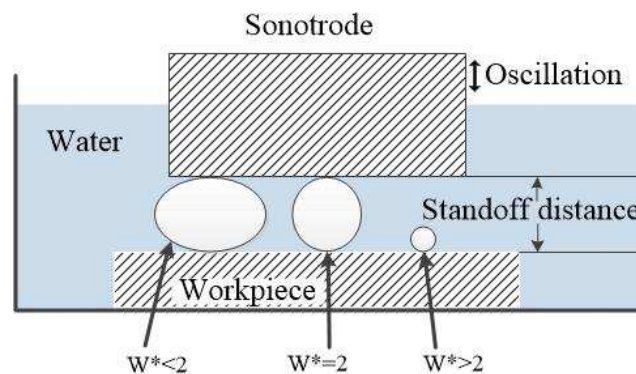


Figure 5.1: Three different bubble characteristics in a small gap.

From the above description, it can be concluded that the effects of w^* on the impact loads were not detailedly investigated yet, but the effects of certain values of w^* (for example, 1.25, 1.65, 2.2 and 5.0) were studied. It was found that the impact loads increase with

the increase of w^* from 1.25 to 1.65 while decrease with the increase of w^* from 2.2 to 5.0. Therefore, the following conclusion can be drawn: the standoff distance in which a single bubble can generate the highest impact force on treated surface is in the range of $1.61 \leq w^* \leq 2.2$. In order to simplify the following studies, it is assumed that the strongest impact force on the workpiece surface is caused when the bubble contacts both the workpiece surface and sonotrode tip.

$$L = 2R_m. \quad (5.1)$$

During ultrasonic cavitation peening, the most energy into the impact process is required. Thus, the optimal standoff distance is at the value of $w^* = 2$, since the strongest collapse on the treated surface is produced at this standoff distance and the energy loss is less than than in the case of $w^* > 2$. Therefore, in the case of $w^* = 2$, the largest impact load occurs on the workpiece surface based on a given R_m . In the case of $w^* = 2$, a large value of R_m is more beneficial for ultrasonic cavitation peening, since a bigger bubble causes a larger impact load.

Different sound pressures generate different bubble sizes while different standoff distances are corresponding to different values of w^* . The sound pressure is related to the vibration amplitude of the sonotrode. In the following, a model is introduced in order to determine the relationship between the vibration amplitude and the optimal standoff distance.

5.1.2 Impacts from cavitation bubbles at different driving currents

The sound pressure depends on the driving current of the sonotrode. Different sound pressure generates different bubble sizes, which causes different impacts on treated surface. However, the impacting loads caused by cavitation bubbles are related not only to the sound field but also to the bubble dynamics. To simplify the model, some assumptions about cavitation bubbles must be made:

- Moving bubbles always stay spherical;
- the liquid is not compressive.

Thus, the dynamics of a spherical bubble that undergoes a sinusoidal pressure in an infinite body of liquid can be described by equation 5.2 [105] with the consideration of the viscosity of the liquid and vapor pressure.

$$R\ddot{R} + \frac{3}{2}\dot{R}^2 = \frac{1}{\rho_l} \left(\left(P_0 + \frac{2\sigma}{R} \right) \left(\frac{R_0}{R} \right)^{3K} + P_s \sin \omega t - P_0 - \frac{2\sigma}{R} - \frac{4\mu}{R} \dot{R} + P_v \right) \quad (5.2)$$

where R_0 is the initial bubble radius, P_s is the amplitude of the acoustic sound pressure, σ is the surface tension coefficient, μ is the viscosity of the liquid, P_v is the vapor pressure, K is the polytropic exponent.

When the cavitation bubbles collapse in a small gap, the plastic deformation or even brittle fractures on the workpiece surface are mainly caused by the micro-jets instead of the shock waves. Therefore, it is necessary to investigate the micro-jets. The formations of the micro-jets are due to the uneven variations of the bubble walls. After equation 2.2 is submitted to equation 2.3, the micro-jet velocity can be deduced in equation 5.3.

$$v_{microjet} \approx 2.186 \frac{R_m}{R_0} \sqrt{\frac{P}{\rho_l}} \quad (5.3)$$

Apart from the micro-jets, energy density of the sound waves can also be used to estimate the impact effects on the workpiece surface. The two forms of energy in a wave are kinetic and potential. In the simple case for the plane wave, the kinetic energy is equal to the potential energy. Thus, the sound energy density in a bubbly liquid can be shown as equation 5.4 [23] and has unit of energy per unit volume.

$$E = \frac{p^2}{\rho_m c_m^2} \quad (5.4)$$

where p , ρ_m and c_m are the sound pressure, density of the bubbly liquid and speed of sound, respectively. In the following paragraphs, the calculation results are illustrated and analyzed. All the values of the physical parameters used in the calculations are shown in Table 5.1.

Table 5.1: Physical values applied in the calculations.

R_0 (μm)	ρ_l (kg/m^3)	P_0 (Pa)	μ (Pa.s)	P_V (Pa)	K
5	998	101300	0.001	2340	4/3

Since each cavitation bubble oscillates independently, the study of the growth and collapse of a cavitation bubble has a universal significance. Based on equation 5.2, the dynamics of single bubbles in conditions are simulated as shown in figure 5.2. Figure 5.2 (a) shows the variations of cavitation bubbles in liquid with different sound pressure amplitudes at 23 kHz. It is assumed that the radius of an initial bubble R_0 is 5 μm at $t = 0$. As shown in this figure, the cavitation bubbles in the high sound pressure have a similar tendency, growing to a maximum size and then beginning to shrink. The maximum bubble radius increases with an increase of the sound pressure amplitude. This is a typical dynamic of cavitation bubbles called transient cavitation. When the sound pressure is close to P_0 (for example, $1.1P_0$), the bubble does not collapse in a period but oscillates around its equilibrium size. This phenomenon is defined as steady cavitation. As shown in figure 5.2 (b), when the initial bubble radius is 15 μm , the collapse of the bubble occurs after

the second growth. This simulation is carrier out in $4P_0$. In figure 5.2 (c), the dynamics of cavitation bubbles are compared at different driving frequencies in $4P_0$. It can be seen than at lower frequency the bigger bubble size is generated. The collapse of the bubble at 69 KHz also occurs after the second growth. Therefore, higher sound pressure, smaller initial bubble size and lower frequency are beneficial for the generation of more violent cavitation.

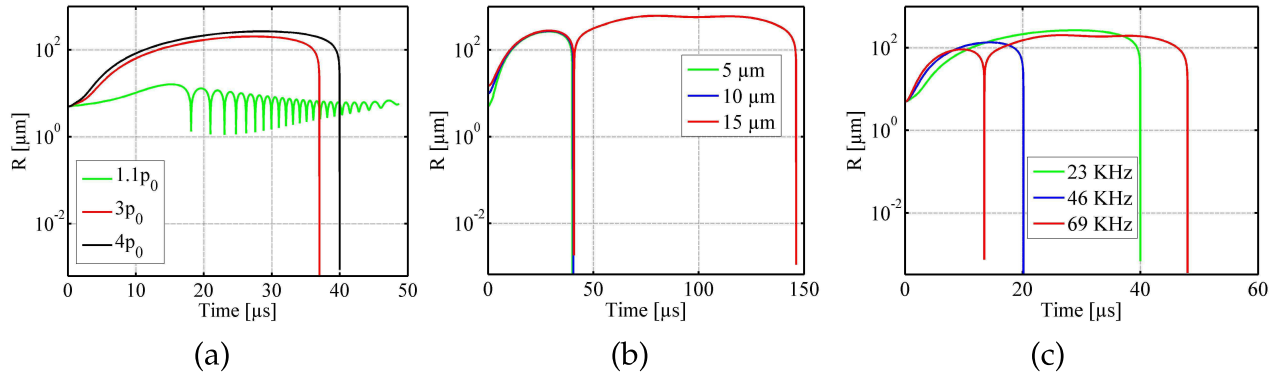


Figure 5.2: Dynamics of cavitation bubbles at (a) different sound pressure, (b) different initial radii and (c) different frequencies

To obtain the optimal standoff distance at a driving current, the calculation process is divided into two steps. In the first step, the relationship between the sound pressure and the radius of the maximum bubble are calculated. During the period of the growth and collapse of a cavitation bubble, the maximum bubble size occurs and depends on the amplitude of the sound pressure. According to equation 5.2, the change of the maximum radius R_m of the cavitation bubble along with the change of sound pressure is partly shown in figure 5.3. The radius of the maximum bubble increases with the increase in the sound pressure. According to equation 5.1, the optimal standoff distance will be calculated in the following section after obtaining the relationship between the maximum bubble size and the sound pressure in the first step.

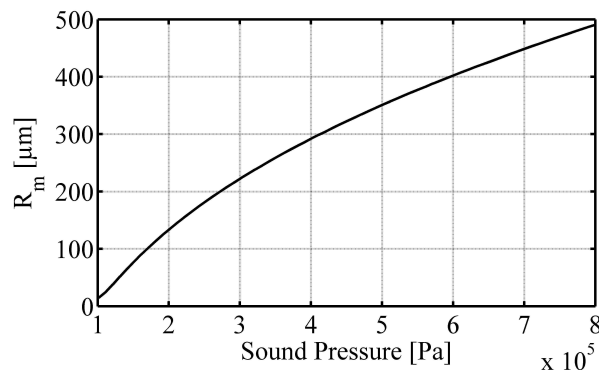


Figure 5.3: The maximum radius of cavitation bubbles in water ($f=23\text{KHz}$, $R_0=5 \mu\text{m}$) with different sound pressure.

In the second step, the optimal standoff distances corresponding to different driving currents are calculated. The maximum bubble size of a cavitation bubble depends on the driving current. If the size of a bubble is not limited in a gap, the bigger the maximum size of the bubble, the larger the impact is when the bubble collapses. When the bubble is located in the gap, the largest impact occurs in the case of $w^* = 2$. Thus, under the same driving current and frequency, there is a well defined standoff distance leading to the most violent bubble collapse on the workpiece surface. Consequently, at this standoff distance the impact caused by the cavitation bubble produces the largest plastic deformation or erosion on the workpiece surface. This is beneficial for the peening process.

In Chapter 4, the sound pressure on the workpiece surface was calculated. According to the relationship shown in figure 5.3, the bubble sizes on the workpiece surface at different standoff distances and driving currents are calculated at 23 KHz and with the initial bubble radius of 5 μm . Then, the relationship between the diameter of the maximum bubble and the standoff distance is shown in figure 5.4. The X axis represents the diameter of the maximum bubble while the Y axis represents the standoff distance. As described above, in the case of $w^* = 2$ there are four optimal standoff distances corresponding to the four different driving currents, respectively. In order to obtain these optimal results, a line whose slope is equal to 1 is plotted. As a result, the intersection points between the line and the four curves represent the case of $w^* = 2$. Therefore, the optimal standoff distances are 0.75 mm, 0.73 mm, 0.68 mm and 0.67 mm corresponding to the driving currents of 0.208 A, 0.250 A, 0.292 A and 0.333 A, respectively.

The region above the line represents the case of $w^* < 2$. In this region, the cavitation bubbles are not spherical due to the small gap. The impact load on the workpiece surfaces decreases with the reduction of the standoff distance. The region below the line shows the case of $w^* > 2$. In this region, the cavitation bubbles contacted with the workpiece surface are spherical and the diameters are less than the gap width. Figure 5.5 shows that the radii of the maximum cavitation bubbles with different standoff distances at the driving current of 0.250 A. When the standoff distance increases, the bubble size near the treated surface become smaller due to the attenuation and the decrease of sound am-

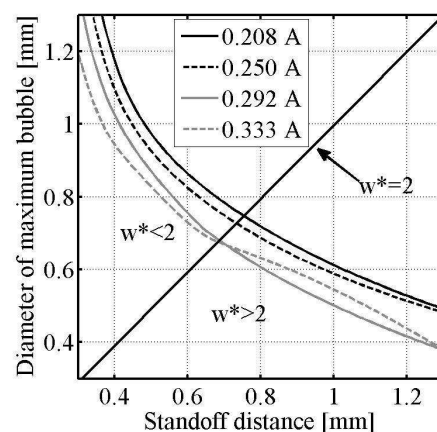


Figure 5.4: Bubble sized at different standoff distances and driving currents.

plitude. Thus, there are other bubbles away from the workpiece surface. The impacts of these bubbles on the workpiece surface are mainly from shock wave instead of micro-jet. Therefore, at the same driving current, the impact loads on the workpiece surface become smaller with the increase of the standoff distance at the case of $w^* > 2$.

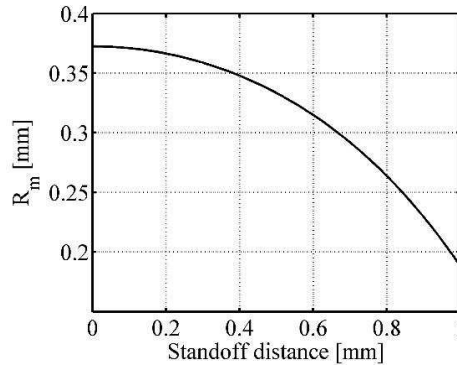


Figure 5.5: The maximum bubble sizes with different standoff distances at the driving current of 0.250 A.

In this chapter, only the four different driving currents (0.208 A, 0.250 A, 0.292 A and 0.333 A) are investigated, since ultrasonic cavitation peening requires the high vibration amplitude. As described in Chapter 4, at the lower driving current the sound pressure on the workpiece surface is higher than that at the higher driving current, which leads to the bigger bubble size at the lower driving current. Thus, the energy caused by one bubble at the lower driving current is more than that at the higher driving current. The main effect on treated surfaces depends on the micro-jet caused by the collapse of cavitation bubbles. From equation 5.3, the velocity of micro-jets at different driving currents and standoff distances are calculated and shown in figure 5.6 (b). The velocity of the micro-jet decreases with the increase in the standoff distance and the driving current.

Nevertheless, at the higher driving current, the wavelength is shorter than that at lower driving current, which causes the increase of the bubble density as shown in figure 4.13. According to equation 5.4, the energy density on the workpiece surface is calculated and shown in figure 5.6 (a). It can be seen that the energy density increases highly with the increase of the driving current. Thus, at higher driving currents, more cavitation bubbles with lower energy are generated on the workpiece surface but the energy density is higher. This means that the single impact load decreases with increasing the driving current but the number of the impact loads increases. Thus, the higher driving current generates the larger impact loads in time average on the workpiece surface. The energy density on the workpiece surface decreases with the increase in the standoff distance. Note that the simulation results shown in figure 5.6 are only available at the case of $w^* > 2$ and $w^* = 2$. Since the growth and collapse of a cavitation bubble is confined by the small gap in the case of $w^* < 2$, the variations of the energy and the micro-jet are different than as shown in figure 5.6.

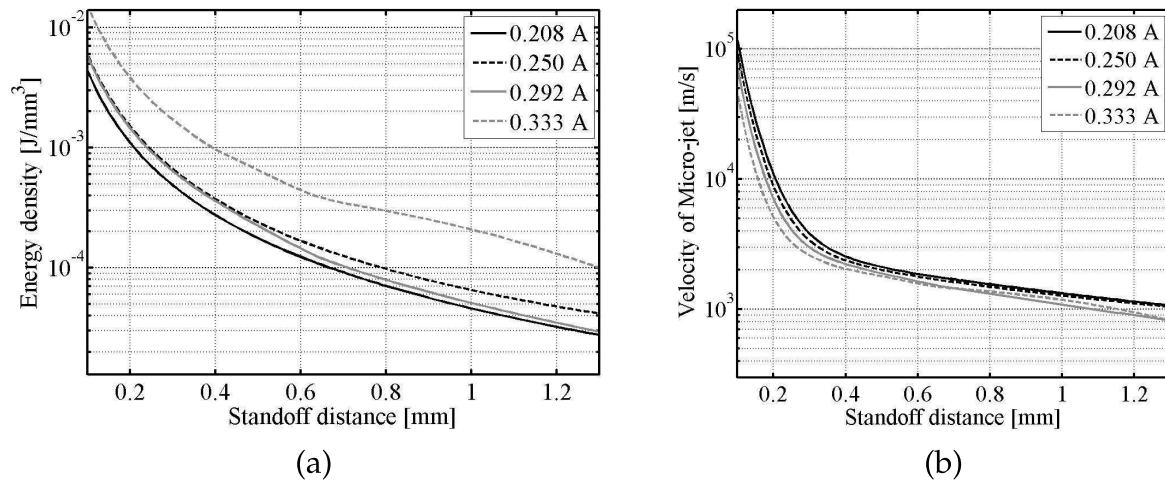


Figure 5.6: (a) The energy density of sound pressure on the treated surface at different standoff distances and driving currents; (b) the relationship between the standoff distances and the velocities of micro-jets at different driving currents.

Above, the effects of cavitation bubbles on workpiece surfaces with different standoff distances was theoretically studied. It was shown that the most favorable standoff distance equals double the maximum radius of a cavitation bubble caused by sound pressure. This model can also be used for calculating the optimal vibration amplitude when the frequency and the standoff distance are determined. Similarly, the optimal frequency can be calculated using this model when the vibration amplitude and standoff distance are given.

Although the impact caused by a single cavitation bubble at higher driving current is smaller than that at lower driving current, the number of the impacts is more due to the increase of the bubble density. Those simulation results will be evaluated in the following sections.

5.2 Experimental investigation of surface volume change

There are many approaches for validating the ultrasonic cavitation on a workpiece surface, for example, aluminum foil and force sensor. With regards to the ultrasonic cavitation peening, the main research objective is the improvement of the surface properties. During this process, the violent collapse of cavitation bubbles strongly impacts on the workpiece surface by the micro-jets, which leads to the generation of the plastic deformation and erosion on the surface. Therefore, the surface volume loss (can also be called volume change) after treatment can be used to evaluate the cavitation intensity. In other words, the cavitation capability can be evaluated by the volume change of the workpiece surface before and after the peening process. To study the influence of process parameters, the standoff distance was varied between 0.1 mm and 1.3 mm. The driving currents were 0.208 A, 0.250 A, 0.292 A and 0.333 A. The initial water temperature was 22 °C,

measured by a temperature controller (AQUA MEDIC T controller TWIN (200.25)). The duration of treatment time was 60 s for every workpiece. Moreover, in order to minimize the influence of temperature, the water in the cylindrical water container was replaced after each measurement, which can make sure that the initial temperatures are the same and the increase of the temperature is less than 4 °C. The distance between the water surface and the tip end of horn was always kept at 10 mm. The standoff distances were measured with the displacement sensor. The control system of the transducer used was the same one as in the SCL experiments. The test specimen is cut into a square of 10 mm by 10 mm and attached to a test bench utilizing a double-sided adhesive tape. The specimen surface was polished before treatment. The roughness was measured by an Alicona microscope and the values of the roughness of the polished surfaces were approximately 0.1 μm .

Since the polished surface is very smooth, it can be considered as a plane which is represented by the red grid in figure 5.7 (left). After cavitation treatment, the polished surface is corroded and a new topography occurs. Thus the volume change is the volume which is contained between the plane and the new topography. Figure 5.7 (right) shows the volume change with the cutaway view along the yellow line figure 5.7 (left). The measurements of the volume change were carried out by the microscope.

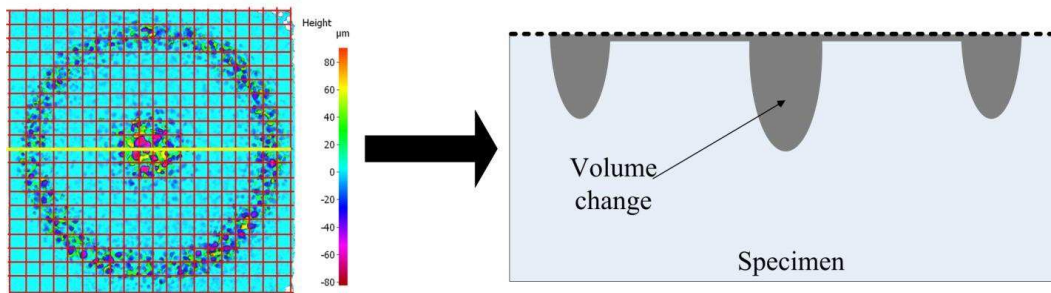


Figure 5.7: The measurement method of volume change.

The change in volume was defined as the difference in volume before and after treatment. Figure 5.8 clearly shows that the surface topographies of the specimens after treatment are different at different standoff distances. In the case of the vibration amplitude at 40 μm , corresponding to the driving current of 0.333 A, the volume change at the standoff distances (a) 0.2 mm, (b) 0.7 mm and (c) 1.1 mm are shown in figure 5.8. As shown in figure 5.8 (c), a smaller volume change compared than that in figure 5.8 (b) is produced. In figure 5.8 (b), the greatest volume change is caused at the center and in the ring area. By increasing the standoff distance to 1.1 mm, the volume change on the treated surface decreases. The cavitation intensity at the center area is almost negligible. It can also be seen that the diameter of the ring is reduced with the increase of the standoff distance. The main reason for this is the effect of the near sound field which is caused by the interfer-

ence of sound waves. The simulation results in figure 4.8 (b) also show this phenomenon. The reason of these phenomena will be explained in the following.

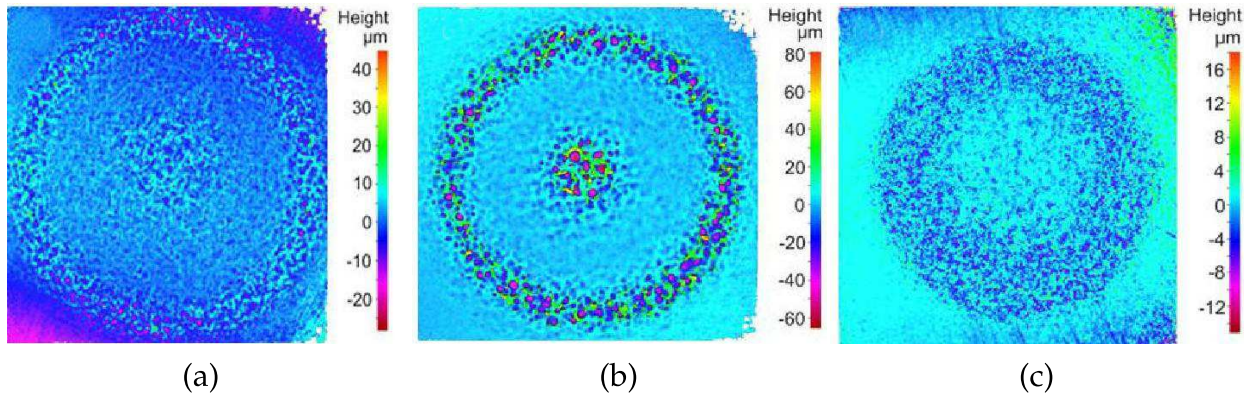


Figure 5.8: Surface topographies at standoff distances of (a) 0.2 mm, (b) 0.7 mm and (c) 1.1 mm with the driving current of 0.333 A

The change of volume at the different four driving currents along with increasing standoff distances is shown in figure 5.9. In this figure, the Y axis represents the volume change caused by cavitation bubbles and the X axis represents the standoff distance. The green, blue, red and black dots are the values of volume change at the driving currents of 0.208 A, 0.250 A, 0.292 A and 0.333 A, respectively. The values of the dots are relatively concentrated and exhibit a unimodal distribution. Thus, the dots can be fitted by the Gaussian equation. From the Gaussian distribution, the mean distribution and the tendency of the data at different standoff distances can be easily obtained.

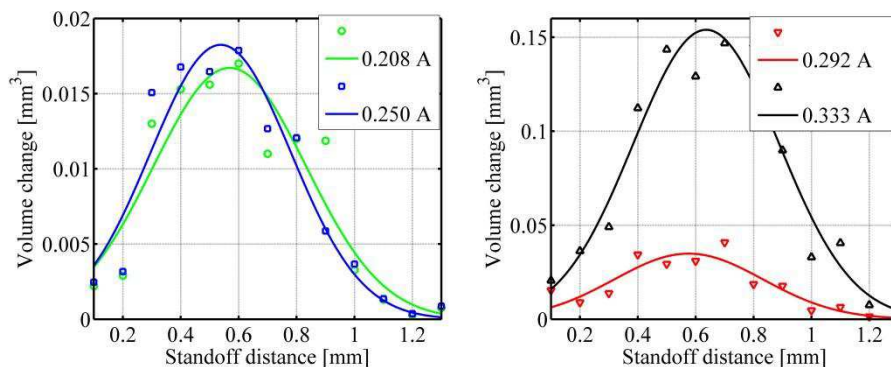


Figure 5.9: The fitted and measurement results of volume changes with increasing standoff distance at different driving currents.

The tendency of the volume change of the fitting curves are similar. The largest volume change occurred in the range of the standoff distance between 0.5 mm and 0.7 mm when the driving current changes from 0.208 A to 0.333 A. The experimental results can be explained well by the change of w^* . In the case of $w^* < 2$, there are two characteristics of bubble collapse: they are the neutral collapse at smaller standoff distances and the splitting collapse at relatively large standoff distances. The impact pressure caused by the neutral collapse is smaller than that caused by the splitting collapse. Therefore, in

the case of $w^* < 2$, the impact loads on the workpiece surface increases as the standoff distance increases. When the standoff distance is larger than $2R_m$, it is the case of $w^* > 2$ and corresponds to the decreasing curve in figure 5.9. The peak of the volume change corresponds to the standoff distance that approximately equals $2R_m$, which is the case of $w^* = 2$.

Figure 5.9 shows that the maximum volume change increases significantly with an increase in the driving current. The increase in the driving current leads to a decrease in sound pressure, which generates smaller cavitation bubbles. After a bubble collapse, smaller impacts are produced on the treated surface. However, higher energy because of more bubbles on the treated surface causes more plastic deformation and erosion. In this case, although the impact caused by a single bubble decreases, the impact number increases because more cavitation bubbles are generated. As a result, more volume change on the treated surface occurs when the vibration amplitude increases in the experimental conditions.

The experimental results are plotted and compared with the simulation results in figure 5.10. The gray dashed curve represents the calculation results while the black lines refer to the experimental results. In this figure, the Y axis is the optimal standoff distances and the X axis represents the driving current. Theoretically, the optimal standoff distance decreases along with the increase in the driving current. Experimentally, the optimal standoff distance decreases from the driving current of 0.208 A to 0.250 A and then increases.

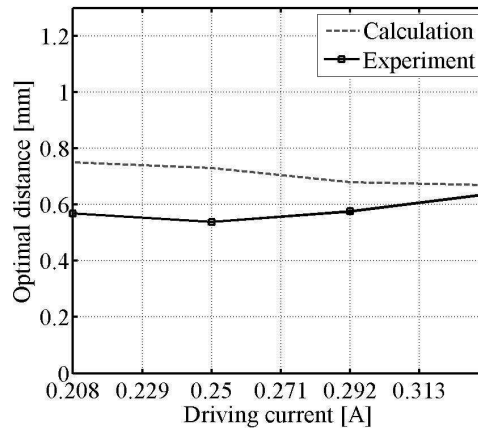


Figure 5.10: Optimal standoff distance versus vibration amplitude.

It can also be seen that the calculated optimal standoff distance is larger than the one measured at the low driving currents. Possible reasons for this are as follows. First, the sound pressure is not homogeneously distributed on the workpiece surface as illustrated in figure 4.6. In the calculated model the maximum sound pressure is utilized because it plays a major role in the surface treatment process, but the measured volume change were generated by the non-uniform distribution on the workpiece surface. Thus, the calculated results are a little higher than the experimental results. However, the results can roughly

reflect the volume change at the center of a sample. Second, all the sound wave propagation is considered to be linear instead of nonlinear. This may also have an influence on the calculation results. In addition, the surface becomes increasingly rough due the impact of cavitation bubbles, which induced the change of cavitation fields. Diffraction and absorption of sound waves always exist on the workpiece surface. Therefore, the sound pressure is less than the calculated pressure, which leads to a reduction of the optimal standoff distances with the maximum cavitation capability during ultrasonic cavitation peening.

Apart from the volume change on the treated surface, the impact area is another evaluation parameter for surface enhancement technology. The impact area means that all the areas are treated by cavitation during ultrasonic cavitation peening. Through the impact areas, the density of the impact loads on the workpiece surface can be estimated. Figure 5.11 (a) shows an example of the available impact area. Due to the smooth surface, once a impact load is applied on the surface, surface topography will changed and can be observed by the microscope. Since the area is circular, the changes of the radius shown in figure 5.11 (a) with a red line can act as a parameter to evaluate the distribution of cavitation bubbles on the treated workpieces. In figure 5.11 (b), the radii of the impact areas are plotted, which can be used to calculate the impact areas. It can be seen that, at the driving current of 0.333 A, the radius of the impact area almost remains stable at 2.1 mm. Regarding the other three driving currents, all the radii of the impact areas decrease with the increase in the standoff distance but the decrease rate is faster when the driving current is smaller. At the driving current of 0.208 A, the radius of the impact area is as small as 1.4 mm. This is because when the driving current is higher, the effects of the side lobes of the sound beam result in the increase of the process area of the workpiece. Therefore, it can be concluded that the impact area is more sensitive at large standoff distances than that at small standoff distances.

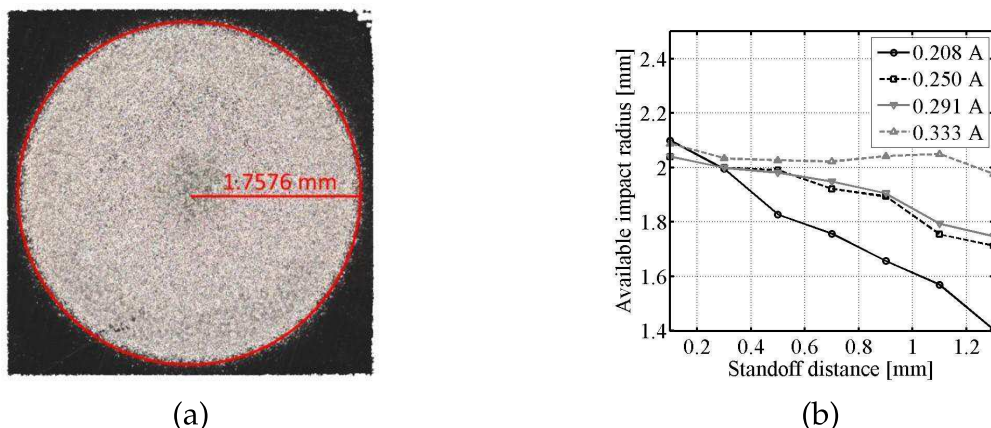


Figure 5.11: (a) An example of the available impact areas and (b) the radii of the available impact areas at different driving currents and standoff distances.

In this section, the volume change and the impact area at different driving currents and standoff distances were measured and discussed. In order to obtain the optimal standoff distance, the Gaussian equation is used to fit the values. It is found that the optimal stand-

off distance is in the range between 0.5 mm and 0.7 mm. The investigations imply that for each vibration amplitude, there is an optimal standoff distance that maximizes the capability of ultrasonic cavitation peening. Additionally, the impact area is considered as another evaluation parameter during this process. The results show that the standoff distance at high driving currents has less influence on the impact area than at low driving currents. The above-mentioned results roughly show the effects of different operation parameters on the treated surface. Nevertheless, the volume change only shows the overlapping results of cavitation bubbles on the treated surface. To more completely investigate the individual impact load caused by cavitation bubbles, in the following sections a piezoelectric sensor is utilized in the investigations.

5.3 Experimental investigation of the impacts on workpiece surfaces utilizing the piezoelectric effect

The measurement method of the surface deformation demonstrates an excellent ability for evaluating the capability of ultrasonic cavitation peening. Due to the overlapping of the pits generated by cavitation bubbles, it is difficult to obtain the impact number and impact loads by measuring the workpiece surface. Therefore, a piezoelectric sensor was used additionally to record the impact signals on the workpiece surface. By analyzing the signals from the piezoelectric sensor, the amplitude of impact loads and the number of the impact loads can be obtained.

5.3.1 Experiment setup for the detection of impact signals

The experimental setup and a scheme with the magnified part are illustrated in figure 5.12. The transducer and the control system were already described in Chapter 4. During measurements, the resonance frequency and the input power of the transducer were recorded. A piezoelectric sensor consisting of a titanium alloy surface cover, two piezoelectric disks and an aluminum alloy bottom was put in a water container. Due to the high corrosion resistance of titanium alloy, the deformation on the surface of the sensor could be avoided as much as possible during measurements. The diameter and the thickness of the piezoelectric disk are 12 mm and 2 mm, respectively. The diameter and the thickness of the surface cover are 30 mm and 0.5 mm, respectively. A copper sheet is located between the two piezoelectric ceramics acting as the positive electrode. Three screws were used to fix those parts together. As the sensor was immersed in water, waterproof glue was used to keep water out from the piezoelectric disks. The signals from the sensor were first converted by a high voltage oscilloscope probe (100x attenuation Testec TT-HV) and then recorded by an oscilloscope (Tektronix DPO3014). Since the resistance of the probe is as high as 100 M Ω , the impedances of other parts in the electric circuit can be neglected. In the measurements, the standoff distance changed from 0.1 mm to 1.3 mm

with the interval of 0.1 mm. The driving currents were 0.208 A, 0.25 A, 0.292 A and 0.333 A.

The piezoelectric sensor was calibrated by a steel ball impact technique. During the calibration, a steel ball was hung from a string, which can be considered as a simple pendulum. The angle of the sensor surface to the horizontal was 90 ° and the center of the sensor was impacted by the steel ball. Since the diameter of the impact areas are less than 5 mm and the diameter of the piezoelectric ceramic is 12 mm, the calibration in the central area of the sensor was accurate enough. The motion of the ball was captured by a high-speed camera and the output signals of the sensor were recorded by an oscilloscope. The speeds of the steel ball before and after the impact can be calculated. The force during the impact was obtained by the momentum theorem using the mass of the steel ball, the impact duration time and the speeds of the steel ball before and after the impact [106]. As a result, the relationship between the output voltage of the piezoelectric sensor V_B and the impact force F_B can be described as:

$$V_B = 0.694F_B \frac{V}{N}. \quad (5.5)$$

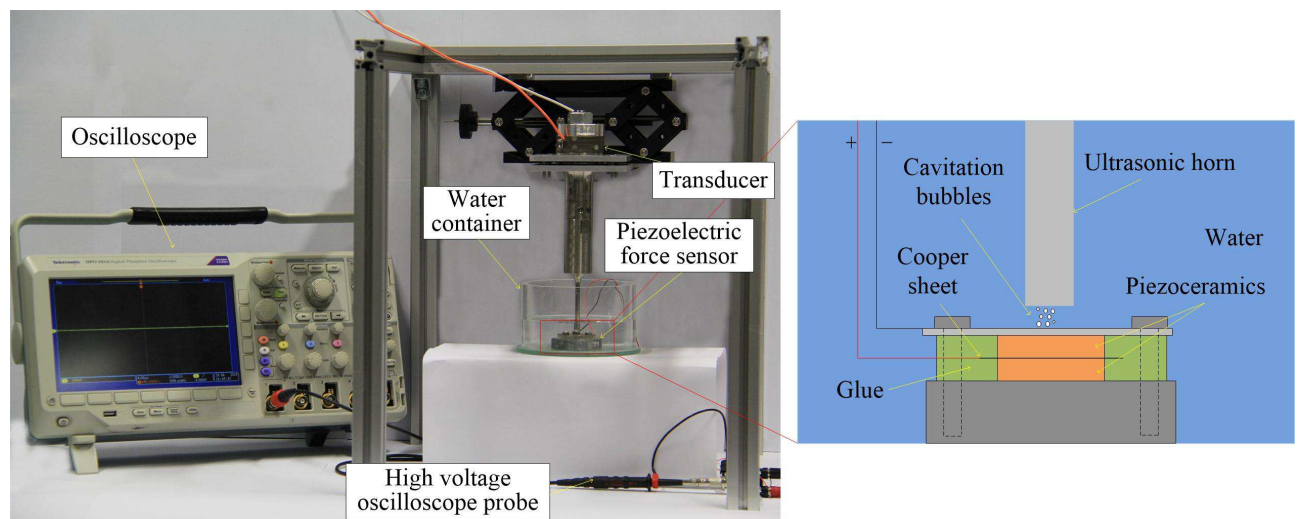


Figure 5.12: Experimental setup for detecting impact utilizing a piezoelectric sensor and a scheme with the magnified part

5.3.2 Impact force caused by cavitation bubbles

As an evaluation factor for ultrasonic cavitation peening, the impact loads caused by the collapses of cavitation bubbles are recorded and processed. The effects of different stand-off distances and different driving currents on impact loads are analyzed in the following sections. When the cavitation bubbles are generated in small gaps, the sensor surface is impacted by the impulse from the cavitation collapse. Then, the voltage signal from the

force sensor can be recorded to obtain the impact loads which are presumably due to the impulse. In order to evaluate the impact on the treated surface, the available impact area has to be measured. This area can be reflected by the erosion pattern caused by cavitation bubbles, as shown in figure 5.11.

When the impulse impacts on the sensor surface, electric signals are generated due to the piezoelectric effect. The impulse impacts can be caused by the collapses of cavitation bubbles and the cavitation clouds. Figure 5.13 shows a part of the impact signals which were converted using equation 5.5. For the determination of an impact load spectrum, 20 s of signals were acquired at a sampling rate of 500 K/s. A minimum threshold (shown as the red dotted line in the figure 5.13), in this case 8.6 N, was considered for impact detection, since the impact load below this value is not expected to make any damage on the soft material (Aluminum foil). The value of 8.6 N is much higher than the background noise (maximum amplitude: 0.0058 N). Additionally, ΔT , which reflects the duration of the impact impulse, is defined as the peak width. The peak width refers to the duration time of the positive part of the pulse. In the following analysis, only the peaks which are higher than 8.6 N are considered.

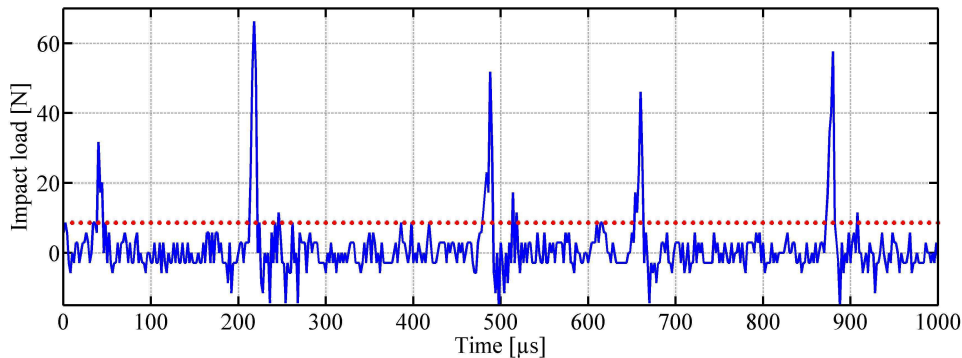


Figure 5.13: The peaks of the impact loads and the threshold.

When the cavitation bubbles are generated by the vibration, the variations of bubbles change periodically with the vibration of the sonotrode. Figure 5.14 (a) shows the excitation signals of the transducer and the impact signals at the driving current of 0.333 A and the standoff distance of 0.7 mm. It can be seen that the large impact peaks always occur at the positive excitation signals. This is because most cavitation bubbles collapse at the period of the positive pressure in the liquid. The positive excitation signals of the transducer correspond to the positive pressure in the liquid. Thus, the impact peaks are mainly concentrated in the period of positive excitation signals. The largest impact may be due to the impact caused by bubble clusters.

In order to compare the impact peaks at the period of the positive excitations and the negative excitations, the peaks of the positive excitation and the negative excitation are first obtained. Then, the impact peaks corresponding to the peaks of the excitation signals are counted and plotted in figure 5.14 (b). The figure shows that the peaks at maximum positive pressure are much larger and more numerous than that at the maximum negative

pressure. The peak rate refers to the peak number per square millimeter per second. Thus, it is deduced that the large impact on the treated surface is mainly generated in the period of positive pressure.

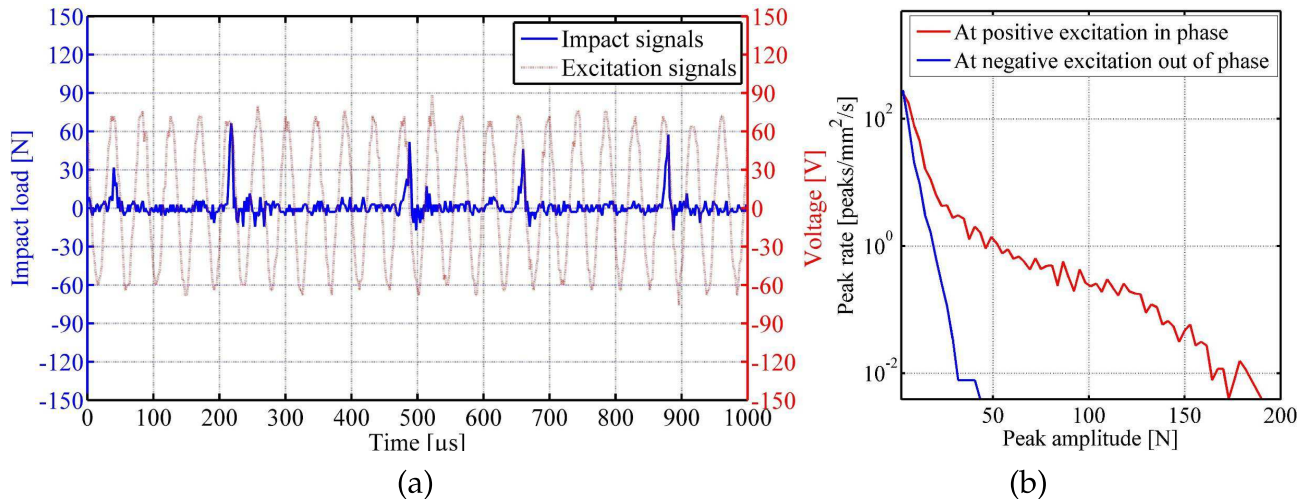


Figure 5.14: (a) Example of the impact signals and the excitation signals; (b) The impact peaks corresponding to the positive peaks and negative peaks of the excitation signals.

As the impact load correspond to the impact load peaks, more violent cavitation collapses cause higher impact load peaks. In figure 5.15, the collective of load peaks are compared at different driving currents (0.208 A, 0.250 A, 0.292 A and 0.333 A) and standoff distances (0.1 mm, 0.7 mm, 1.3 mm). The horizontal axis gives the force amplitude whereas the vertical axis gives the peak rate. The higher driving current leads to higher impact loads and the number of larger impact loads is much less than that of small impact loads. Large impacts have a much greater influence on the treated surface, since only a sufficiently large impact causes plastic deformation on the treated surface. The higher driving current makes the amplitude of the vibration of the sonotrode larger, which results in the increase of output energy on the workpiece surfaces. Thus, the number of cavitation bubbles generated in the gap is higher at higher driving currents than that at smaller driving currents. The impact loads caused by those cavitation bubbles become larger due to more impulses on the sensor surface.

Figure 5.15 shows that the variations of the standoff distance are sensitive to the distribution of the peaks. At the same driving current, the peak rate of the lager impact loads at the standoff distance of 0.7 mm is the highest while the rate is the lowest at the standoff distance of 1.3 mm. The highest peak amplitude reaches about 260 N. The frequency of the large impact loads is higher at higher driving currents and there are the similar tendencies at the driving currents of 0.208 A, 0.250 A, 0.292 A and 0.333 A. Therefore, the impact effects on workpiece surface at the standoff distance of 0.7 mm is better than others. These results also validate that there are more events of bubble collapses occurring at the higher driving currents.

In addition to the amplitude of the impact loads, the peak width is another key factor

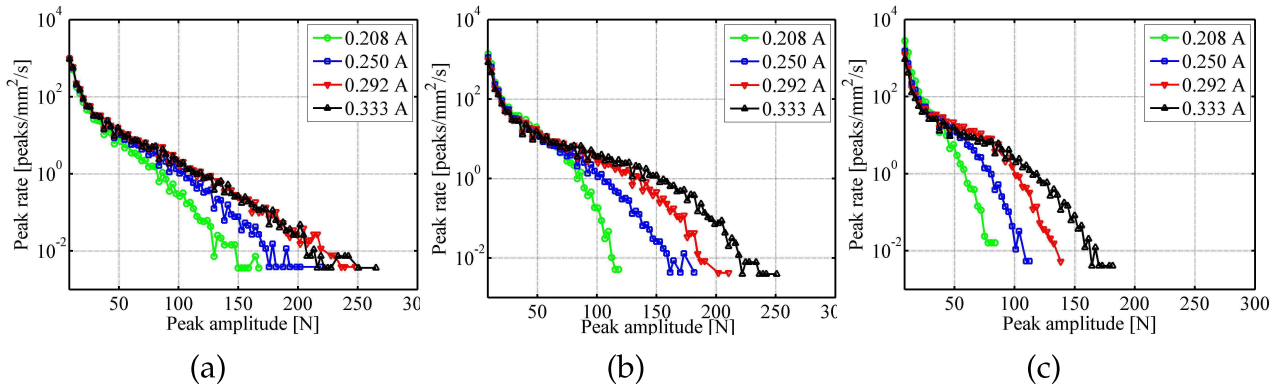


Figure 5.15: The peak rates of the impact loads at the standoff distances of (a) 0.1 mm, (b) 0.7 mm and (c) 1.3 mm.

to evaluate the impact effects caused by cavitation bubbles, since the larger peak width represents the larger emitted energy with the same peak amplitude. In other words, large peak durations cause more impact energy on the treated surface, if other conditions remain the same. Figure 5.16 shows the relationship between peak width and the peak rate. As shown in figure 5.16 (a), the peak rate decreases with the increase in the peak width. The distributions of the peak widths at different driving currents stay virtually the same. The distributions at different standoff distance also remain similar, as shown in figure 5.16 (b). Therefore, the distributions of peak widths change little whether it is at different driving currents or at different standoff distances.

To more clearly show the relationship among the peak number, the peak amplitude and peak width, for example, at the standoff distance of 0.7 mm, figure 5.17 (a) and figure 5.17 (b) show the contours at driving currents of 0.208 A and 0.333 A, respectively. At the same peak width, the number of the higher peak amplitude at driving current of 0.333 A is always more than that at driving current of 0.208 A. Therefore, it is deduced that higher driving currents generate more impact energy on workpiece surfaces.

As shown in figure 5.17, the cavitation impacts on a surface depend on the peak ampli-

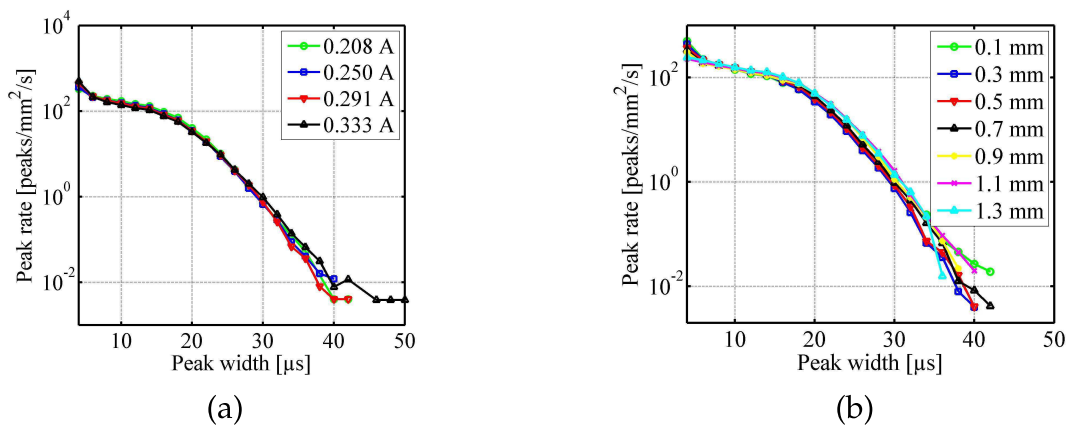


Figure 5.16: Peak rate versus peak width at different driving currents and standoff distances.

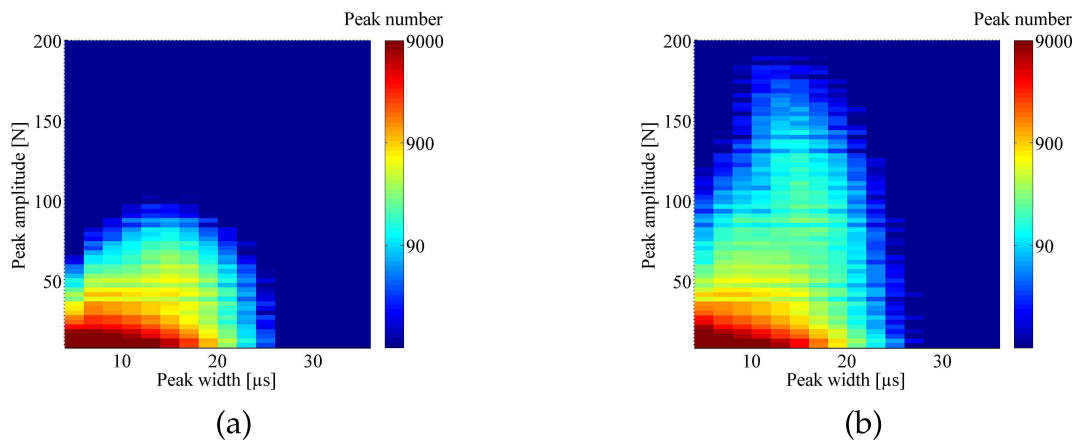


Figure 5.17: Contour of the number density of cavitation impulsive versus peak width and peak amplitude at the driving currents of (a) 0.208 A and (b) 0.333 A.

tude, peak width and peak number. In order to easily evaluate the impacts on surfaces, those scatter plots can be fitted by a line function. An example at the driving current of 0.208 A and at the standoff distance of 0.1 mm is shown in figure 5.18 (a). As the peak widths is almost unchanged at different driving currents and standoff distances, the larger value of the slope means there are more higher peak amplitudes. Figure 5.18 (b) shows the slopes at different driving currents and standoff distances. The results reflect the fact that, as the driving current increases, the impact amplitude also increases. The optimal standoff distance occurs at the range of 0.6 mm and 0.9 mm.

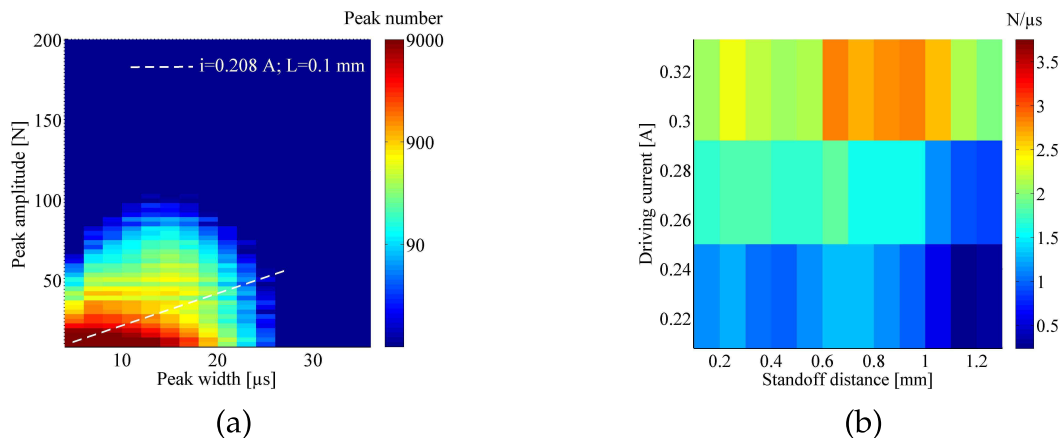


Figure 5.18: The slopes at different driving currents and standoff distances.

From the analysis of the peak amplitude, peak width and peak number in time domain by the peak rate and the fitted slopes, it is found that the impact energy increases with increasing the driving current. At the range of the standoff distance between 0.6 mm and 0.9 mm, the impact energies are higher than those at other standoff distances. Since the impacts caused by ultrasonic cavitation should show the periodicity characteristics, in the next section the impact peaks are analyzed in the frequency domain, whereby new characteristics are reached.

5.3.3 Impact analysis in frequency domain

The liquid on the treated surface undergoes ultrasonic sound pressure at the resonance frequency of the ultrasonic transducer at about 23 kHz, which leads to the periodic growth and collapse of the bubbles. However, cavitation phenomena are microscopic, transient, random and multi-phase, which leads to a random nature of the signals from the sensor. The signals are assumed to realizations of a stationary random process. The power spectrum density (PSD) can be used to show the characteristics of the recorded signals in frequency domain. In other words, the signals obtained in time domain are transformed to frequency domain by Fast Fourier transform (FFT). The PSD analysis is performed based on the output of FFT transform.

Since the PSD of the impact loads is equal to the PSD of the electric signals of the sensor, the PSD of the electric signals will be investigated in the following. Assuming that the voltage and the current on a resistance R_e are $V(t)$ and $i(t)$, respectively, the instantaneous power can be described as: $P(t) = V(t)^2/R_e$. For qualitative analysis, it is usually assumed that the resistance R_e is 1 Ω to obtain the normalized power value. The original unit of the PSD is V^2/Hz . Using the normalized method, the unit can transform V^2/Hz into $V^2/\Omega/Hz(W/Hz)$. For quantitative calculations, the de-normalized power value can be obtained by substituting the actual power value. The PSD are computed utilizing the Matlab implementation of the Welch method, which is a commonly used estimation method for correcting the power spectral density [107]. In the following analysis, the whole signals are divided into many segmentations and the Flattop window is used to reduce the errors by compensating for the spectral energy leaks. In the Welch method, the length of the window represents the length of the segmentation for each processing while the overlap parameter refers to the length of the overlap between two adjacent segments of data.

It is the same as the signals in the analysis in time domain, the number of the sampling is 10 M and the sampling time is 20 s. Here, the Welch method with 50% overlap and a flattop window function of 2.5 s size is utilized to plot the power spectrum density. A high overlap of the processing data leads to high frequency resolution. However, when the overlap is more than 50%, the effect is useless and only more average values are obtained. The more segments there are, the smaller the noise is, but the less the accuracy of the amplitude is. Thus, 2.5 s is a better choice for this PSD analysis. Figure 5.19 shows an example at the standoff distance of 1.3 mm and at the driving current of 0.333 A. As the figure shown, the peak amplitude at about 23 kHz is higher than other peak amplitudes at the corresponding frequencies. This frequency equals to the resonance frequency of the sonotrode. The peaks at around 46 kHz and 69 kHz are caused by the effects of the sound irradiation from the sudden changes in pressure. The changes are due to the shock waves [108]. Since the vibration amplitude is smaller, the values of the PSD are smaller than that at the resonance frequency. Therefore, the power at the resonance frequency is dominant. The frequency resolution is 0.2 Hz in the power spectral and the bandwidth of the power

is from 0 to 10^5 Hz.

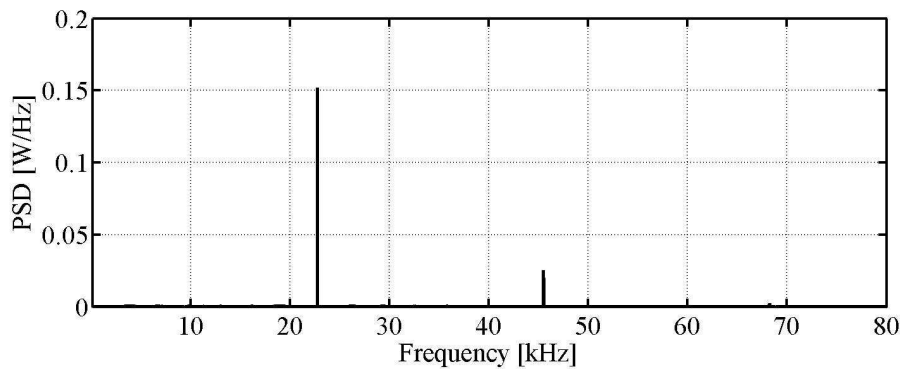


Figure 5.19: Power spectrum density at the standoff distance of 1.3 mm and at the driving current of 0.333 A.

Since the main power occurs at the resonance frequency, the power is investigated under different conditions to show new characteristics. Figure 5.20 shows the amplitude values of the PSD at the resonance frequency when the driving currents and standoff distances change. Similar to the tendency show in figure 5.9 and figure 5.18 (b), the amplitude value of PSD increases with the increase of the driving current while increases first and then decreases with increasing the standoff distance. The difference is the range of the optimal standoff distance between 0.8 mm and 0.9 mm, because the results only show the main power at the resonance frequency instead of the total received power with the bandwidth from 0 to 10^5 Hz. Nevertheless, the analysis in the frequency domain is an effective way to evaluate the impact effects during ultrasonic cavitation peening.

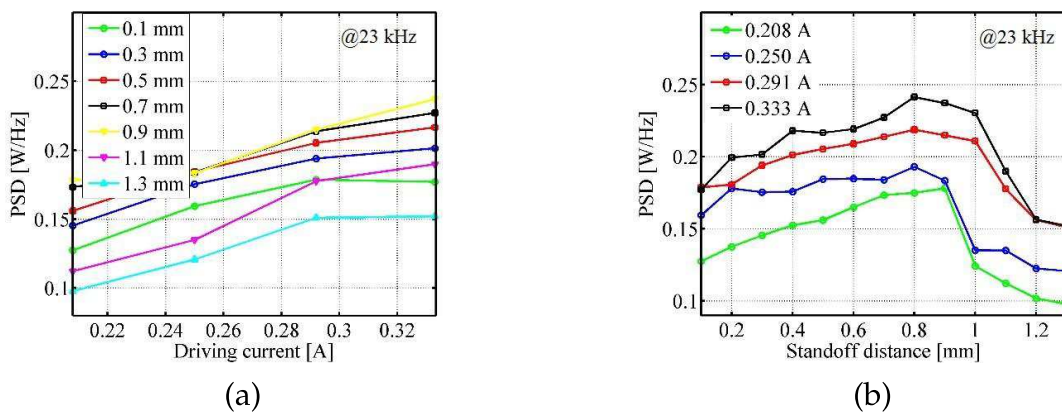


Figure 5.20: The values of the power spectrum density at the resonance frequency of 23 kHz.

5.3.4 Efficiency of the cavitation process

Since the impact power at other frequencies also have an influence on the workpiece surface, the total received power of the piezoelectric sensor is worth analyzing and discussing. The total received power is the sum of the powers from 0 to 10^5 Hz. As shown in

figure 5.21 (a) the power increases with an increase in the driving current. Figure 5.21 (b) shows that the power increases initially and then decreases with an increase in the stand-off distance at the same driving current. The peaks of the four curves are in the range of 0.5 mm and 0.9 mm.

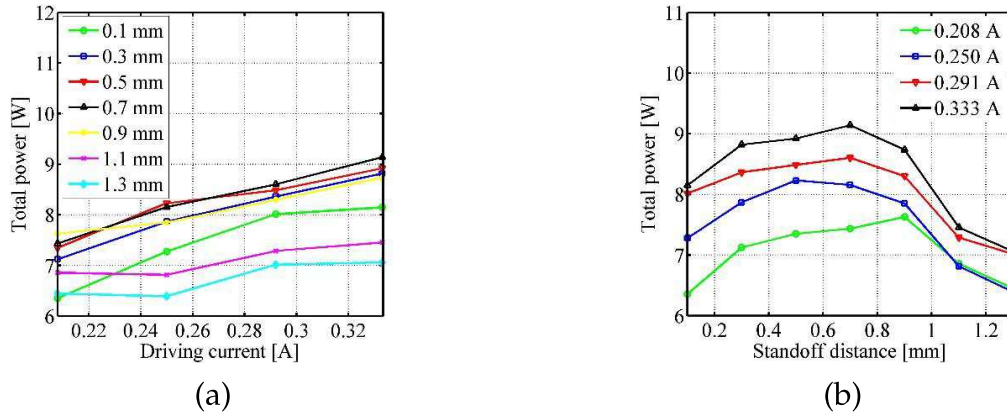


Figure 5.21: The total received power at different standoff distances and driving currents.

For the purpose of industrial application, to improve energy conversion, delivery and utilization efficiency is another research objective. The total received power shown in figure 5.21 can be used to estimate the cavitation efficiency which can be estimate on the basis of the ratio of the total received power on the sensor surface to the input electric power of the transducer. Figure 5.22 (a) shows the input power applied on the working transducer under different conditions. The electric input power can be directly obtained from the digital phase control unit. The power increases with increasing the driving current and is almost unaffected by the standoff distance changes. Figure 5.21 shows the power due to the impact on the piezoelectric sensor. The power is considered as the output power, since the processed signals is obtained directly from the measurement sensor. In figure 5.22 (b), the cavitation efficiency over driving currents and standoff distances is plotted. It can be seen that the high cavitation efficient occurs at low driving current, since the attenuation is low at the low driving current. Thus, more energy can be delivered to the sensor surface. At the optimal standoff distance, the cavitation efficiency is the highest since in the case of $w^* = 2$ the largest impact loads are generated.

In this chapter, different bubble shapes were initially discussed, since the optimal standoff distance depends on the bubble characteristics. It was deduced that the optimal standoff distance equals the maximum bubble diameter ($w^* = 2$). Next, the energy density of the sound pressure and the velocities of the micro-jets on the workpiece surface were calculated. According to the calculation results, the optimal standoff distance is validated with two different experiments, the experiment of the surface volume change and the experiment of impact loads on the sensor surface. The simulation results show that the largest impact on the workpiece surface should occur in the range of 0.67 mm and 0.75 mm under the investigation conditions. By measuring the surface volume change and analyzing the impact signals in time domain and frequency domain, it was found that the experimentally determined optimal standoff distances are in agreement with the calculated results.

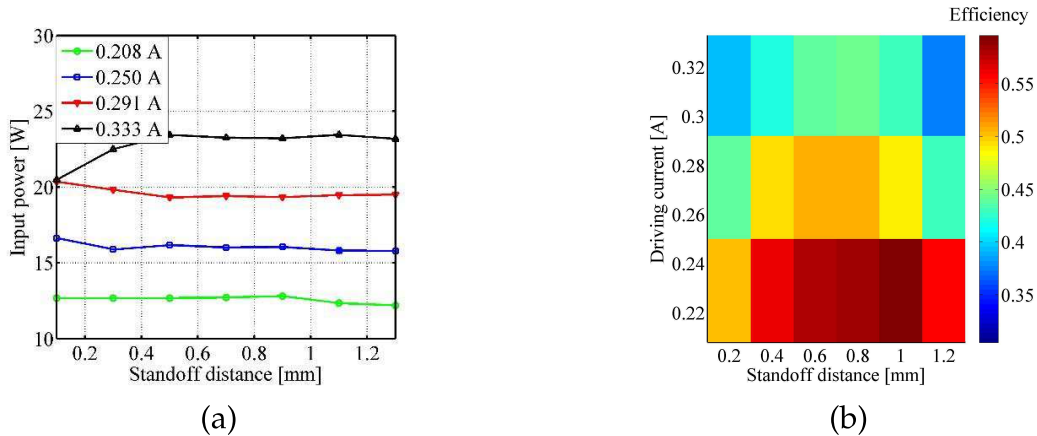


Figure 5.22: (a) Input power of the transducer at different driving currents and standoff distances; (b) Efficiency at different driving currents and standoff distances.

The highest cavitation efficiency also occurs at the optimal standoff distance.

6 Phases of the ultrasonic cavitation process and variations of surface properties

The affects of acoustic cavitation on the surface properties of solids can be classified in four different phases, as presented in chapter 2. They are incubation period, acceleration period, deceleration period and steady-state period. Since only the first phase, the incubation period, is beneficial to the ultrasonic peening process, this chapter focuses on the determination of the duration of this phase and on the modification of surface properties during the phase of the cavitation process. In this chapter, the detection of the incubation period of the ultrasonic cavitation process and the mechanical behavior of the metal surface subjected to various conditions are presented. The main part of this chapter was published in [109].

6.1 Detection of the process phases by plastic deformation measurements

In this section, experimental procedures, micro-structures of the workpieces and a evaluation of different phases during cavitation process will be introduced. These investigations are beneficial for understanding a new method which is used to more accurately detect the incubation period.

6.1.1 Experimental procedures

The test setup for generating cavitation bubbles is the same as that described in Section 4. The specimen was immersed in a water container ($\Phi 110 \text{ mm} \times 90 \text{ mm}$) and the depth between the free liquid surface and the specimen surface was 10 mm. The standoff distance was 0.7 mm and the initial water temperature was 22 °C. In order to minimize the influence of temperature, the water in the container was replaced after each measurement. In this way, the initial temperature can be guaranteed the same and the experimental time can be saved. The original specimen is in the form of 4-mm-thick sheet made of aluminum alloy 5005 with a polished surface with a roughness of about 100 nm. The original surface hardness is 50 HV. As revealed by optical microscopy (figure 6.1), this aluminum alloy has an initial grain size of $77 \pm 27 \text{ }\mu\text{m}$ [110]. After polishing it was cut into square pieces

(10 mm × 10 mm) and treated by ultrasonic cavitation peening. Since the specimen surface is very smooth, the original surface is measured repeatedly using the Alicona microscope and then the average values were obtained as reference surface.

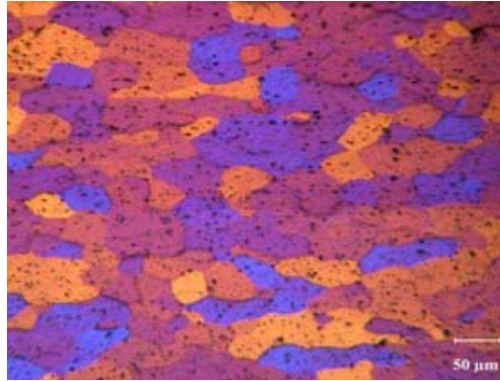


Figure 6.1: Optical measurement of the microstructures of the aluminum alloy 5005 [110].

To detect the mass loss and volume change, the experiments were carried out with different cavitation process times (from 30 s to 270 s with the interval time of 30 s) and different driving currents (0.208 A; 0.250 A; 0.292 A; 0.333 A). When the treatment of a specimen was completed, the specimen was dried using absorbent paper before further measurements were made. The specimen was weighed with a microscale before and after treatment. The measurement resolution of the scale is 0.1 mg. In order to get accurate measurement results, the weight test was done when the specimen was removed from the water after one hour. The volume change of the specimen was also measured after the treatment.

The surface microhardness was measured by a hardness tester designed and assembled by myself, shown in figure 6.2. The main parts of the hardness tester include: an eddy-current displacement sensor (Lion precision ECL101 with probe U 5), a force sensor (HBM PW4M C3) and a Vickers indenter of the micro load (SIANTEC SV1032M). During measurements, the specimen was fixed on the test bench. The measurement point can be adjusted by the horizontal guide. Moving the vertical guide downwards and upwards can load force and unload force, respectively. Using this method, the signals from the force sensor and displacement sensor were recorded and then processed by Matlab. The microhardness can be analyzed using the loading and unloading curves.

During cavitation peening, a circular treated region or a ring region is produced on the specimen surface. The microhardness of ten different points evenly distributed along the diameter of the circular ring region was measured. The microphotography of the measured surface, which is magnified 50 times, is partly shown in figure 6.3.

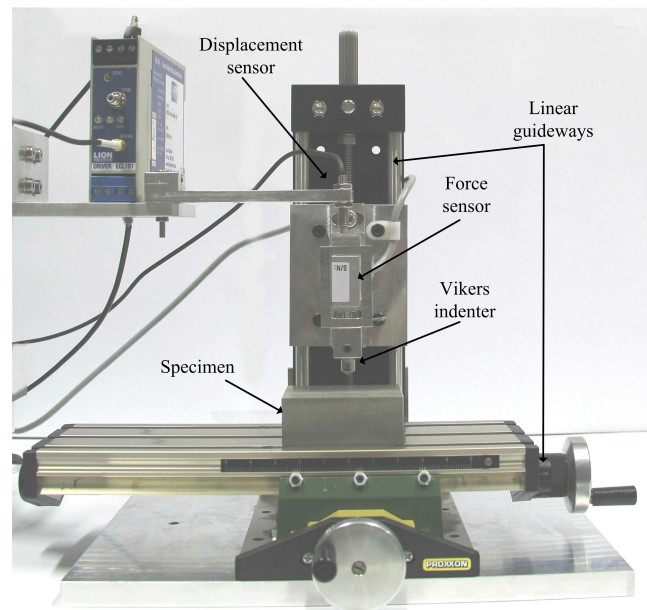


Figure 6.2: The hardness tester.

6.1.2 Micro-structure in different phases

The micro-structure of the initially polished surfaces was captured by the microscope with a magnification of 50 times. Figure 6.4 (a) shows a part of the polished surface as an example. Some scratches due to the polish process are clearly seen. However, the surface is still very smooth and its surface profile is shown in figure 6.4 (b). The height variation of the curve is almost the same as the surface height along the line in figure 6.4 (a). The height of peak to peak is as low as about $0.1 \mu\text{m}$. Ten specimens were selected and measured. Since all the surface conditions were nearly identical, the example shown in Figure 6.10 can be considered as a reference.

The plastic deformation on the treated surface is produced and accumulated with the increase in the process time. In order to see the isolated plastic deformation pits, it is necessary to treat the specimen in a very short time. The test time used here was 0.5 s, which can guarantee that some single pits exist. The test time was controlled by the phase

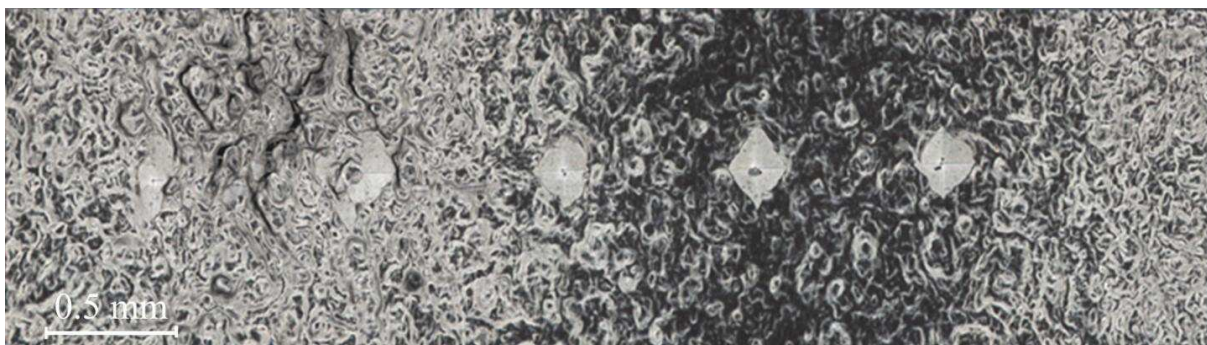


Figure 6.3: The microphotography of a treated specimen with the patterns printed by the Vickers indenter.

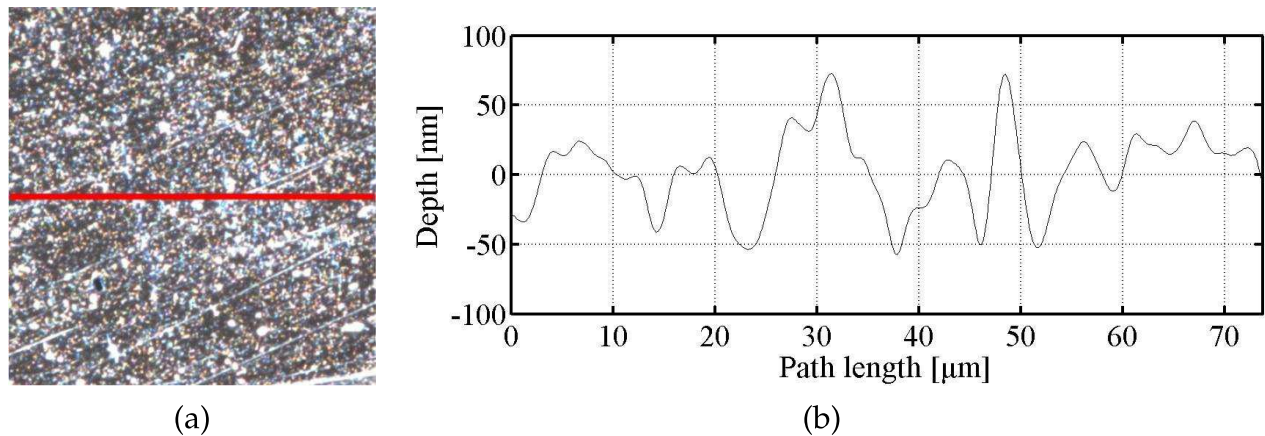


Figure 6.4: The polished surface and the surface profile.

digital control unit. When the process time increases, the number of the pits also increases. In this process time, the impacts may overlap on the same area, which leads to a large pit with corrosion if the number of the impact load is enough. The single plastic deformation pit and the corrosion pit are shown in figure 6.5 (a) and figure 6.5 (b), respectively. In figure 6.5 (a), the capture area is $110\ \mu\text{m}$ by $110\ \mu\text{m}$, and there is a pit with the depth of $1.4\ \mu\text{m}$. The dimension of the pit is about $20\ \mu\text{m}$. It is a plastic deformation pit since there are not any obvious edges around the pit. On the other hand, for figure 6.5 (b), the captured area is also $110\ \mu\text{m}$ by $110\ \mu\text{m}$, and there is a larger pit with the depth of about $30\ \mu\text{m}$. The diameter of the pit is about $90\ \mu\text{m}$. The edges of the pit are sharp. Therefore, it can be deduced that the pit was caused by the grain loss instead of the plastic deformation, since the size is similar to the grain size shown in figure 6.1.

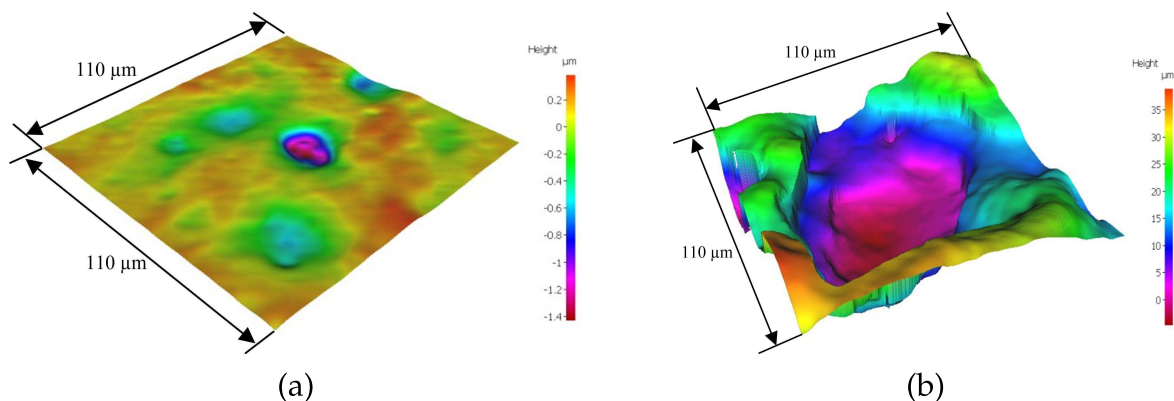


Figure 6.5: A plastic deformation pit and a corrosion pit with an area of $110\ \mu\text{m}$ by $110\ \mu\text{m}$.

In order to observe the variations of the surface profile in different phases, the microstructures of the specimen surfaces were captured at a driving current of $0.208\ \text{A}$ as an example. Figure 6.6 (a), (b) and (c) correspond to the process times from $30\ \text{s}$, $150\ \text{s}$ and $270\ \text{s}$. All the figures were captured on the central area, as the cavitation intensity is the strongest in this area. In figure 6.6 (a) there is no corrosion but only plastic deformation and some small pits are generated on the treated surface, because the contrast which is produced by the plastic deformation does not suddenly change. In this figure, it is also possible to observe that no material loss has occurred yet and there are also no obvious

cracks. In figure 6.6 (b) cracks are obviously observed. In figure 6.6 (c), the surface is severely corroded. The large pit indicates that there are material loss on the treated surface. During cavitation process, the plastic deformation is generated in the first phase. In the second phase, the cracks appear on the treated surface. Finally, the grains are torn from the surface and the mass loss occurs simultaneously.

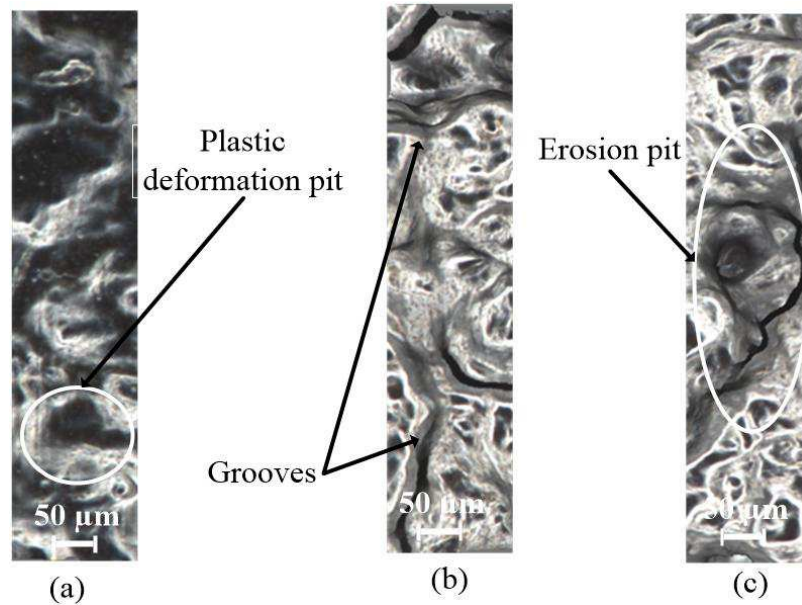


Figure 6.6: The microstructure of treated specimen with process times of (a) 30 s, (b)150 s and (c) 270 s at the driving current of 0.208 A.

It can be deduced that at small driving currents, pits caused by cavitation are generally shallow. At high driving currents, the specimen surface profile changes severely and large pits are formed due to violent impacts. Thus, higher driving currents cause more plastic deformation in a shorter period. With an increase in the process time, more mass loss will be caused as well.

According to the results from figure 6.6, figure 6.7 can show the explanation for the cavitation process. Figure 6.7 (a) illustrates a section of the polished surface, in which the grains are shown clearly. Figure 6.7 (b) represents the plastic deformation pits on the surface. The dashed line represents the original surface while the curve adjacent to the dot line represents the plastic deformation. This plastic deformation occurs simultaneously as the surface is still highly elastically deformed. After the impacts caused by the collapses of cavitation bubbles, the compressive residual stress is generated on the surface. With the increase in the impacts, some cracks are generated on the surface due to dislocations of grains, which is shown in figure 6.7 (c). In the aspect of the inner stress, when the inner stress exceeds the ultimate stress, the material damage (cracks) occurs. However, the grains still stay in the specimen surface. If there are more impacts on the treated surface, the grains will be pulled out and mass loss occurs [111]. Figure 6.7 (d) depicts this situation. In this case, the compressive residual stress is reduced and the surface hardness decreases, which is not desired. Thus, the duration time before the cracks are generated

on the surface is the optimal process time for ultrasonic cavitation peening.

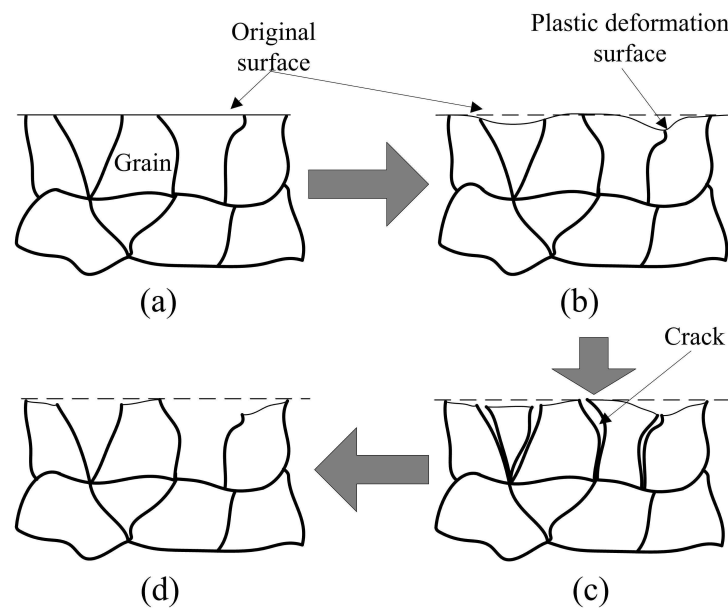


Figure 6.7: Scheme of the different phases during ultrasonic cavitation erosion.

In this section, the different phases of ultrasonic cavitation erosion were described through the changes of micro-structures. It can be concluded that there are three different phases in terms of the micro-structure: the plastic deformation, the generation of cracks and the grain loss. During ultrasonic cavitation peening, the ultrasonic cavitation on the treated surface should end before the crack generation.

6.1.3 Evaluation of different phases during ultrasonic cavitation peening

Based on the discussion about the micro-structure in the last section, a new method for detecting the incubation period will be developed in this section. During a cavitation process, volume change and mass loss are generated gradually and can be measured after the treatment. The volume change contains the volume change due to the mass loss and the volume change due the plastic deformation. As described in Chapter 2, the volume change and mass loss can not clear distinguish the incubation period. Therefore, using the volume of plastic deformation to distinguish the incubation period is a new method due to the generation of much plastic deformation in this period.

Figure 6.8 shows four different surface topographies of specimens after ultrasonic cavitation peening treatments under the following experimental conditions. The driving current was 0.250 A and the process times were 60 s, 120 s, 180 s and 240 s, respectively. The square measuring area has an edge length of 4 mm. As shown in the figures, when the cavitation process time increases, more pits are generated and the depths of the pits increase. Thus, more volume change is introduced. Most pits are concentrated in the ring

region and in the center area, which is a typical pattern induced by ultrasonic cavitation peening using a cylindrical sonotrode. The sonotrode tip has a diameter of 5 mm, but the diameter of the erosion ring area is less than 4 mm. The most volume change is highest in the central region, which means that the intensity of cavitation bubble collapses occur in the central area. For the single pit which is caused by many impacts, the maximum depths at the process time of 60 s and 120 s are around 20 μm and 160 μm , respectively. As shown in figure 4.17, at the same experimental conditions, the radius of the ring in the SCL photography well agrees with the radius of the ring in figure 6.8. With an increase in the process time, the erosion in these regions becomes increasingly severe. Thus, it was validated that when the cavitation bubbles are trapped in the small gaps, more cavitation bubbles concentrate at the ring and the central area.

In figure 6.8 (d), the inhomogeneous distribution of the ring pattern is obviously observed, since the specimen surface and the tip end of the sonotrode are not totally parallel. Due to the tiny difference of the standoff distance, the near-field sound pressure on the treated surface changes. As a result, the distribution of the collapse events of the cavitation bubbles on the specimen surface is inhomogeneous. Nevertheless, with the increase of the process time, the number of the impacts caused by the collapse of cavitation bubbles increases, which leads to more erosion and plastic deformation on the treated surface. Thus, both the mass loss and the volume change may increase, for example, in figure 6.8 (a) the volume change is 0.1355 mm^3 but there is no erosion.

Figure 6.9 shows the variations of the specimen surfaces with different driving currents of 0.208 A, 0.250 A, 0.292 A and 0.333 A at the same process time of 240 s. It can be seen that the diameters of the rings increase with the increase in the driving currents. In general, higher driving currents introduce more input power, which leads to the generation of higher sound pressure. Due to the high sound pressure on the specimen surface, the stronger cavitation intensity is produced on the surface. The pits at the driving current of 0.333 A are the deepest of all the specimens. The pit depth is around 160 μm at the driving current of 0.208 A while the depth is 250 μm at the driving current of 0.333 A. Furthermore, the center pit is larger than others. In the SCL experiments shown in figure 4.17, the strongest cavitation intensity also occurs at the central area, but the ring areas do not well agree with the ring areas in figure 6.9. This is because that at the higher driving current, the side lobes of the sound beam increase as described in Chapter 4. Therefore, the distribution of the cavitation bubbles on the specimen surface is different from the SCL results which show the spatial distribution of cavitation bubbles.

Apart from the change in the topography, the mass loss is also various under different experimental conditions. The mass loss refers to the difference in the mass of the specimen before and after the cavitation peening process. As shown in figure 6.10, mass loss increases when the process time is extended. It can be seen that more mass loss occurs at the higher driving currents. To provide a clear comparison, the mass loss at driving current of 0.208 A and 0.333 A are described in detail in the following. At the first treatment time of 30 s, the difference of mass loss is about 0.1 mg at the two above-mentioned

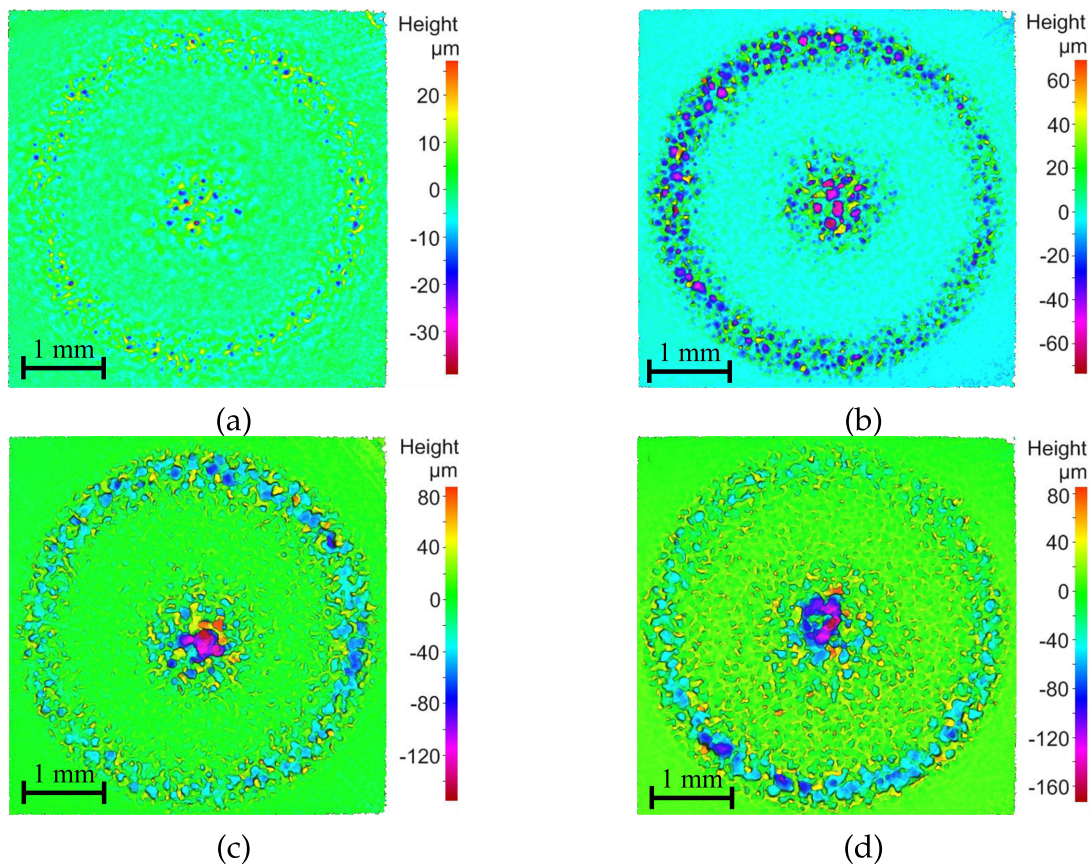


Figure 6.8: Measured surface topographies of specimens treated with 0.250 A and different process times: (a) 60 s, (b) 120 s, (c) 180 s and (d) 240 s.

currents. When the process time increases, the difference of mass loss at the two driving currents becomes increasingly large. At the end of the process time, the difference already reaches 0.5 mg. The curves sometimes intersect with each other due to the measurement solution of 0.1 mg.

During the cavitation process, more process time causes a greater amount of impact events on the treated surface. Higher driving currents lead to the higher vibration amplitudes of the sonotrode, thus more violent bubble collapses are generated on the treated surface. As a result, with more process time and higher driving current, more cavitation bubbles and higher impact intensity occur, which leads to more mass loss as well. However, there are different phases during ultrasonic cavitation process. Ultrasonic cavitation peening takes the advantages in the incubation period. Thus, the first two phases are important because in the latter two phases cavitation erosion and not plastic deformation is generated. Since the cavitation erosion is a continuous process, the clear boundary between the incubation period and the acceleration period does not appear in the experimental conditions. From figure 6.10 it is not easy to determine the end of the incubation period. In the following sections, the investigation is focused on the determination of the end of the incubation period.

Compared to the mass loss, the volume change can also be used to evaluate the effects of cavitation process on the specimen surface. Figure 6.11 illustrates the volume change

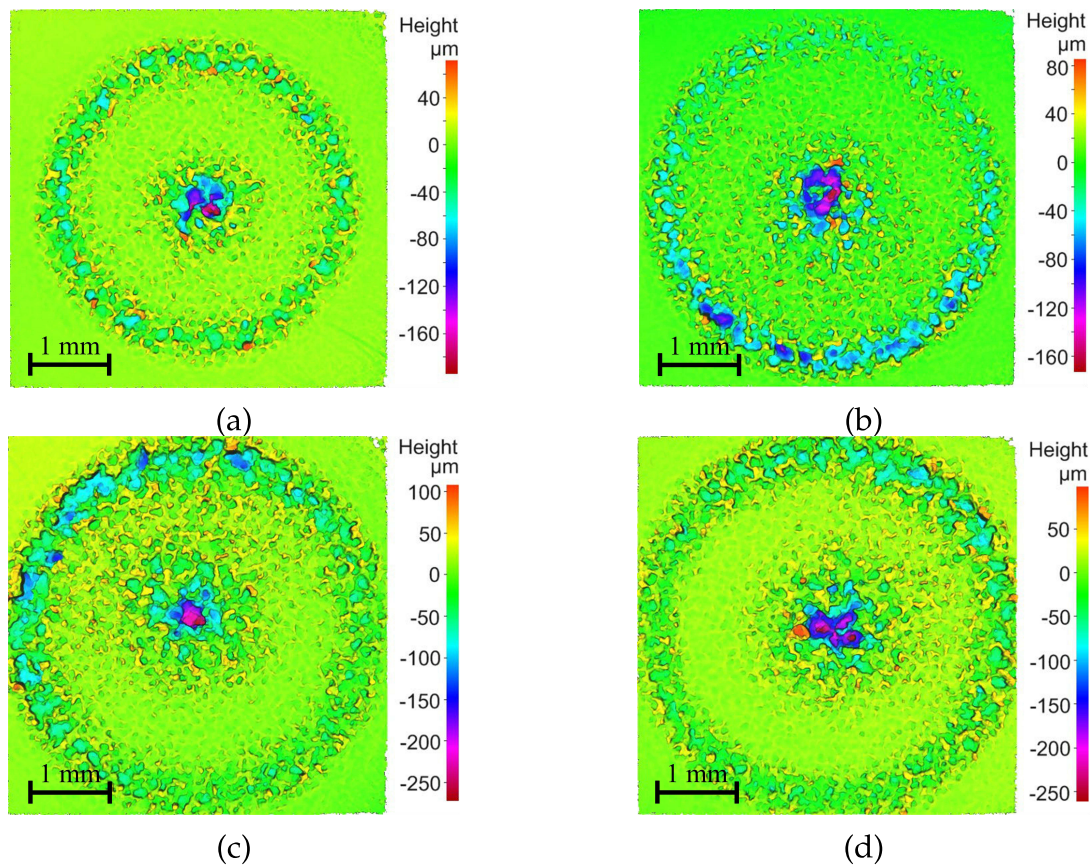


Figure 6.9: Measured surface topographies of specimens treated with the driving currents of (a) 0.208 A; (b) 0.250 A; (c) 0.292 A and (d) 0.333 A.

under different driving currents and different process times. Similar to the tendency of the mass loss, the volume change increases with an increase in the process time while more volume change is caused by higher driving currents. It also can be seen that the volume change increase more rapidly in the initial process period than that in the end process period. Especially at the first process time of 30 s, the difference of the volume change remains almost completely the same whether the driving current changes or not. This may be due to the removal of the oxide layer on the specimen surface. With the continuous increase of the process time, the increase rate of the volume change becomes different. At the end of the experimental time, the volume change reaches more than 0.9 mm^3 at the driving current of 0.333 A while about 0.5 mm^3 at the driving current of 0.208 A. It is also not easy to exactly determine the end of the incubation time from figure 6.11. Thus, it is important to determine the end of the incubation period during ultrasonic cavitation peening.

In the incubation period, the plastic deformation is dominant in the volume change. The plastic deformation pits on the specimen surface is mainly caused by the multi-impact from the micro-jets. Figure 6.12 is utilized to understand the procedure of single pit formation. The figure shows the pits with plastic deformation or mass loss caused by ultrasonic cavitation. Even if the impact is as high as 200 MPa, it is difficult to generate a pit with mass loss after an impact. Thus, the typical pit formation with the mass loss should

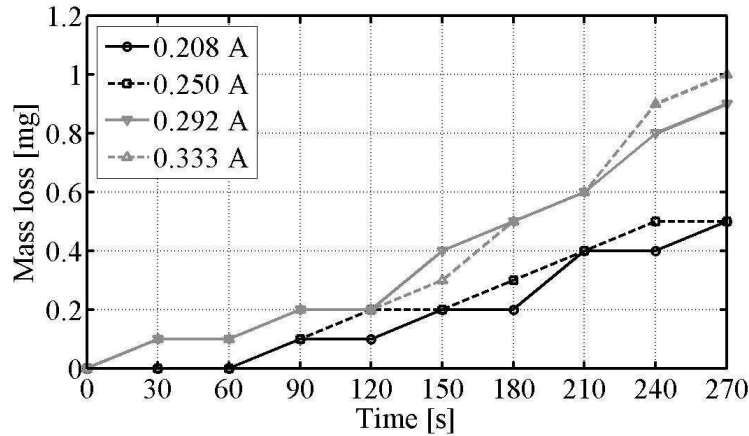


Figure 6.10: Mass loss at different process time and driving currents.

be from multi-impacts. At the beginning of the cavitation process, much plastic deformation is produced and the grains are refined. With the continuous increase in the process time, some micro cracks first occur and grow. After a certain length of the cracks parts or grains will break out, which damages the treated surface. As shown in figure 6.12, the region of the mass loss is marked by the gray dotted and jagged lines. During the ultrasonic cavitation peening process, the mass loss is not desired. Additionally, the total volume change consists of the mass loss and the plastic deformation.

As described above, due to the cavitation process, refined grains are produced and plastic deformation is generated. Both the refined grains and the plastic deformation cause slight changes to the surface density. Here, the change of the density is neglected. Therefore, the volume of plastic deformation is calculated with equation 6.1.

$$V_p = V_{change} - \frac{m_{loss}}{\rho_w} \quad (6.1)$$

where V_p is plastic deformation volume; ρ_w is the density of the specimen; V_{change} is the

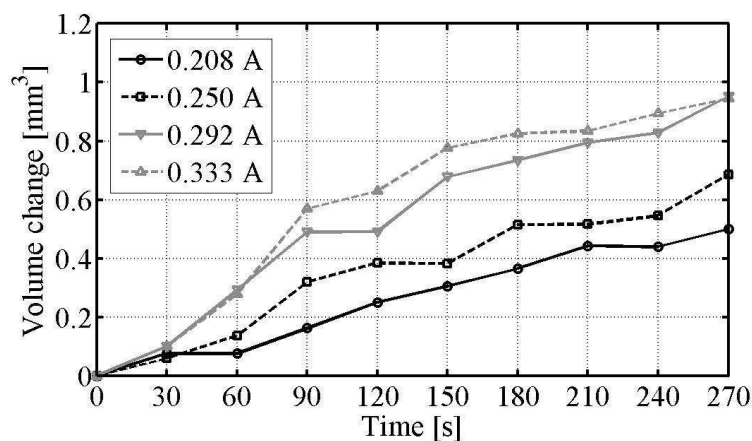


Figure 6.11: Volume change at different process times and driving currents.

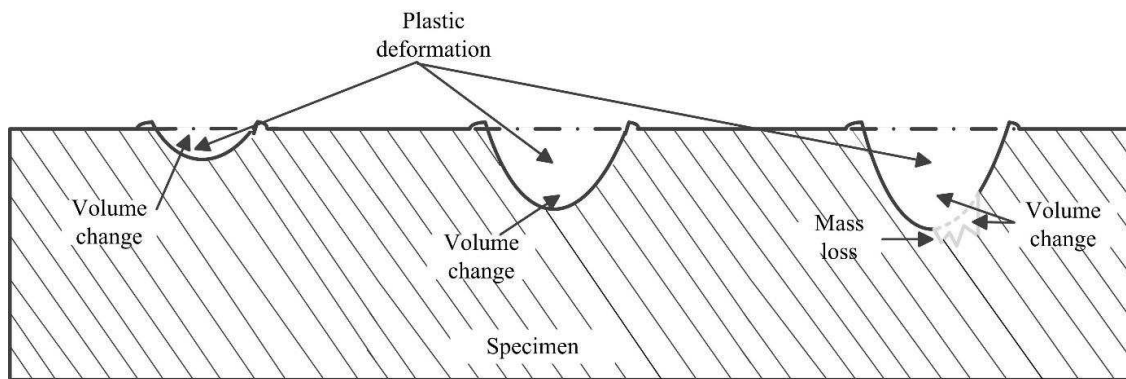


Figure 6.12: Scheme of a surface with plastic deformation and mass loss.

total change of the volume and m_{loss} is the mass loss after treatment.

Figure 6.13 shows the volume change of plastic deformation with different driving currents and the process times. At each driving current, all the data show a first rise and then steady trend. Therefore, the data with the same driving current are reasonable to be fitted by two straight lines. By this way, the intersection point of the two lines can distinguish the two stages. During fitting, the minimum sum of the mean square deviations of the two fitted lines is selected as an optimal case of the two fitted lines. After fitting, it can be seen that the volume change of the plastic deformation increases quickly at the first stage and then remains almost constant.

At both stages, the rate of the plastic deformation at the lower driving current is slower than that at a higher driving current. Additionally, the end of the incubation period can be determined by the inflection point of the two lines at each driving current, because, after the inflection point, the plastic deformation decreases. On the other hand, as shown in figure 6.13, the mass loss changes only little after the inflection point in all situations. Therefore, the time corresponding to the inflection point is considered as the end of the incubation period.

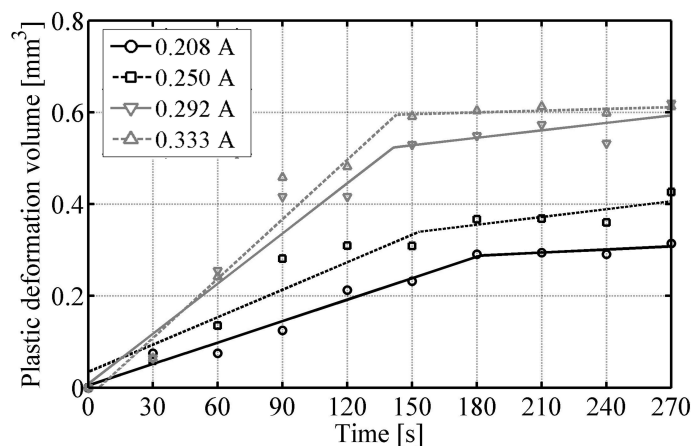


Figure 6.13: Volume change of the plastic deformation at different process times and driving currents.

To show clearly the changes of the plastic deformation during ultrasonic cavitation, the values of the rates of the plastic deformation at different driving currents are listed in detail in Table 6.3. Furthermore, the time corresponding to the inflection points are also described in the table. The incubation period at the driving current of 0.208 A is much longer than that at the other three driving currents. The rate of the plastic deformation is more rapid at higher driving currents than that at lower driving currents. At the same driving current, the plastic deformation increases rapidly until the end of the incubation period. This is because higher energy density is produced on the treated surface at the higher driving current. Although the size of the cavitation bubbles becomes smaller at the higher driving current, the impact events caused by the collapse of the cavitation bubbles increase significantly. Therefore, the higher driving current causes a shorter incubation period. With an increase in the process time, the number of impacts on the surface increases as well. If the damage is caused by the same energy, the beginning of the damage at the lower driving current is longer than that at the higher driving current. Thus, the beginning of the damage caused by the cavitation erosion is later at the low driving current. After the incubation period, the plastic deformation is still generated, but only slightly.

Table 6.2: The incubation period and plastic deformation rate at different driving currents.

Driving current (A)	Incubation period (s)	Plastic deformation rate in incubation period (mm^3/s)	Plastic deformation rate after incubation period (mm^3/s)
0.208	181	1.577×10^{-3}	0.227×10^{-3}
0.250	153	1.911×10^{-3}	0.569×10^{-3}
0.292	141	3.642×10^{-3}	0.543×10^{-3}
0.333	142	4.312×10^{-3}	0.127×10^{-3}

The difference of mass loss and volume change before and after treatment were investigated in this section. Both increased as the driving current and the process time increased. From the measurement results, the plastic deformation was deduced. The results show that a higher driving current leads to a higher plastic deformation rate on the treated specimens and shortens the incubation period. Compared to the determination of the volume loss and the mass loss, the determination of the plastic deformation has two advantages: the incubation period can be more precisely calculated and the rate of plastic deformation can be obtained. The surface properties of the treated workpieces during these period will be investigated in the following section.

6.2 Investigations of the relationship between surface properties and cavitation process time

In the last section, the incubation period was determined by the plastic deformation volume. It is expected that the mechanical surface properties at the end of this period is optimal. In this section, the surface topography, surface roughness and micro-hardness will be investigated.

6.2.1 Surface topographies and roughness at different process phases

The surface topography is one of the characteristics of the specimen after ultrasonic cavitation peening used to evaluate the surface properties, since the surface profile reflects the cavitation intensity and the cavitation modification areas. Since the treated regions on the specimens surfaces are circular symmetrical, curves that vary along the diameter can represent the change in the all treated regions. Figure 6.14 shows surface topographies of the specimens with different process times and different driving currents of (a) 0.208 A, (b) 0.250 A, (c) 0.292 A and (d) 0.333 A. The X axis is the process time, the Y axis is the evaluation length of the specimen along the diameter of the ring area and the Z axis represents the height change of the surface caused by cavitation peening. The duration of the process time for each group was from 30 s to 270 s with the time interval of 30 s. The scan area is 4 mm by 4 mm, since this area includes all the surface variation area.

At the first process time of 30 s, the surface topographies are almost unchanged even at the high driving current. Meanwhile, the changes of the surface topographies are less than that at the longer process times. When the process time increases by 30 s, the height in each central region is the highest. Then, with the continuous increase of the process time, the variations of surface topographies become more pronounced even at the other parts. This means wider and deeper pits have been produced on the treated surfaces. At the driving current of 0.208 A, when the process time increases to 180 s, the surface topographies become more rough. However, with the increase in the driving current, the duration time when the surface profile variation becomes shorter and shorter. It can clearly be seen that at the driving current of 0.333 A the duration time before rapid variations of the surface occur is only 60 s. Thus, all the topographies under the investigation conditions are shown in figure 6.14 and the change tendencies are also introduced. The surface profile does not change much in the incubation period. The measurement data in the topographies can also be used to evaluate the surface roughness. Under the investigation conditions, the roughness is always relatively low, less than 8 μm , in the incubation period.

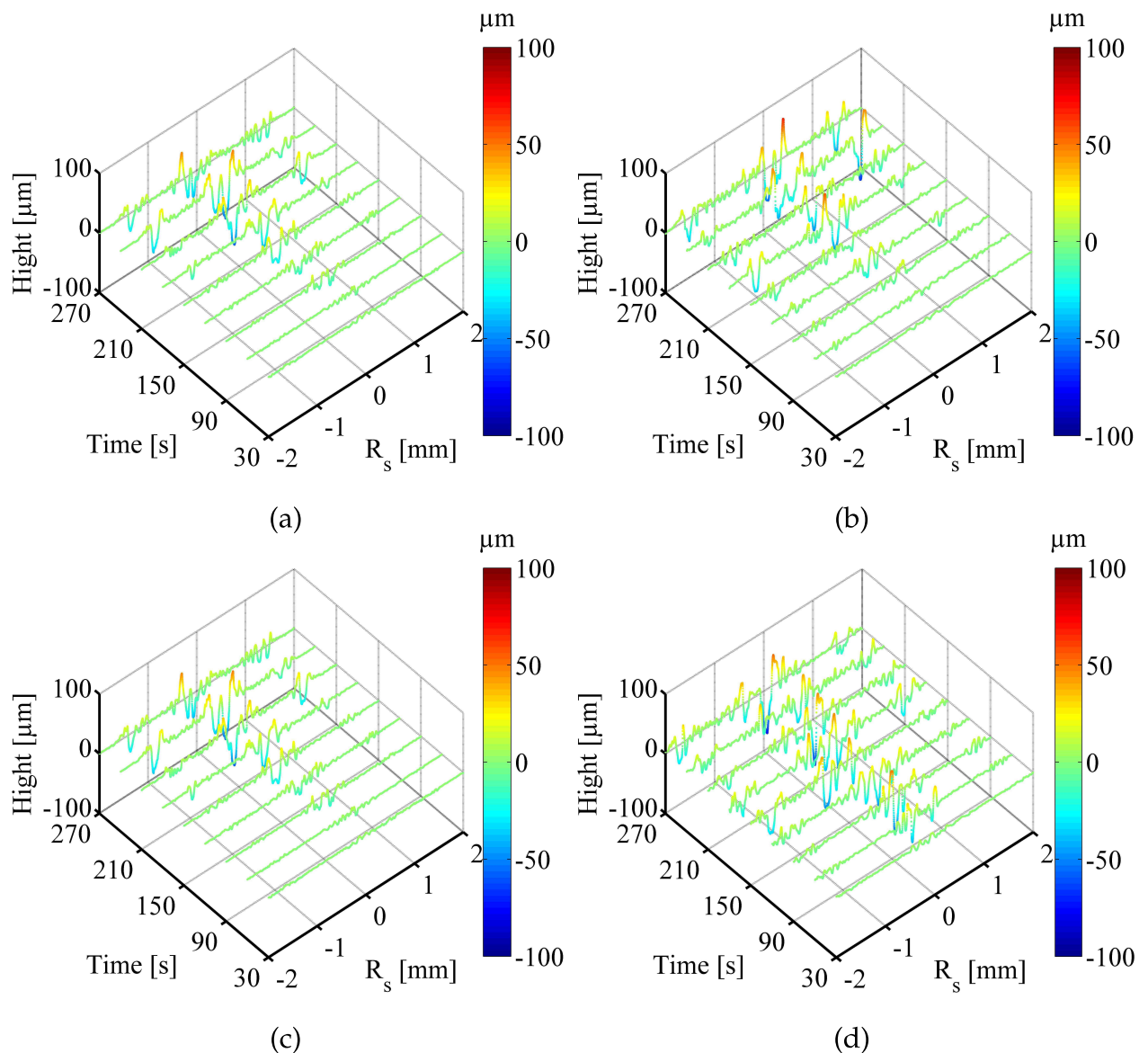


Figure 6.14: Surface topographies of specimens with different process times and different driving currents of (a) 0.208 A; (b) 0.250 A; (c) 0.292 A; (d) 0.333 A.

6.2.2 Micro-hardness at different process phases

Micro-hardness is important for the evaluation of the surface quality. When an impact is generated on a metal grain, the grain is plastically deformed, which results in dislocation movement and multiplication. The dislocation multiplication means the increase of the number and density of the dislocations. These effects increase the hardness of the grain. In general, it is supposed that the hardness in the plastic deformation region is greater than that in the original surface due to the dislocations of grains. Surface hardness can usually be measured utilizing the length of the diagonals of the imprinted rectangular shape of an indenter. In most cases after ultrasonic cavitation process, the imprinted rectangular shape produced by the indenter is not seen clearly enough due to the tiny patterns and the rough surfaces. In the load-displacement method, the micro-hardness of a material sur-

face from indentation load-displacement data is obtained by the calculation of one cycle of loading and unloading. During the test, the force F (maximum value is 2 N) is applied on the indenter and the displacement h is measured simultaneously. An exemplary load-displacement curve of the micro-hardness measurement is shown in figure 6.15. On each peened specimen, the micro-hardness was evenly measured at five different points along the diameter of the ring area. The values were averaged and the standard deviations for each sample were calculated to obtain the final averaged micro-hardness values. It can be observed that the maximum load was 1.96 N and the maximum indentation depth h_{max} was 15.2 μm . The residue depth after unloading h_f is 13.2 μm . The stiffness S is determined by the slope at the tangent line of the beginning of the unloading curve. From the above parameters, the micro-hardness is finally calculated using equation A.3.

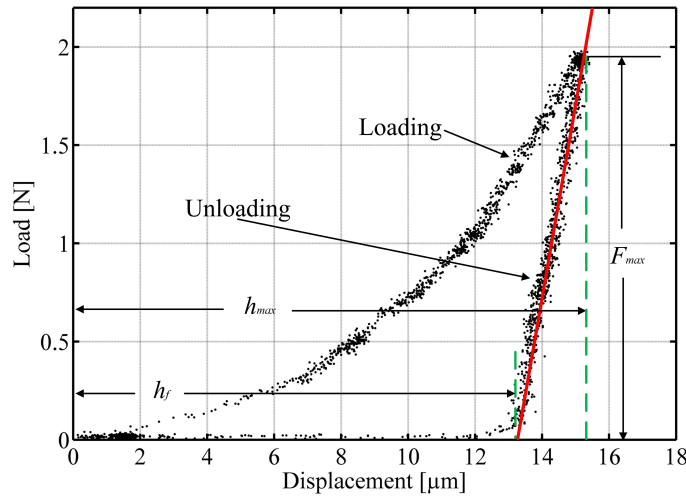


Figure 6.15: The load-displacement curves for the measurement of hardness.

The micro-hardness of the original specimen surface is HV 50. Figure 6.16 shows the values of the micro-hardness and the confidence intervals (cyan lines) after treatment. The micro-hardness first increases and then decreases at different driving currents with an increasing process time. At the beginning of the cavitation erosion, a hardening layer is produced resulting from the impacts of the cavitation bubble collapses. With an increase in the process time on the specimen surface, cavitation erosion becomes severe, which causes small cracks to occur on the specimen surface and some damage is produced soon afterwards. Hence, the textures of the specimen surface are destroyed, which leads to a decrease in the surface micro-hardness. For different driving currents, the micro-hardness reaches a peak value more rapidly at the higher driving current than that at the lower driving current. At the driving current of 0.333 A, the surface micro-hardness is enhanced to HV 76 at the process time of 120 s. Compared to the original surface micro-hardness, it is increased by 52%. The increase of the micro-hardness reaches the same level as water jet cavitation peening. The maximum micro-hardness at the driving current of 0.208 A, however, occurs at the process time of 150 s and the value is HV 68, which is lower than at the driving current of 0.333 A. These time spans almost correspond to the incubation periods shown in Table 6.3. Therefore, during the incubation period, the micro-hardness can be

enhanced owing to the continuous plastic deformation. When the incubation period ends, the influences of surface deterioration on the treated surface become significant, which leads to a decrease in the surface micro-hardness. Thus, the highest micro-hardness occurs at the end of the incubation period. Overall, the average value of the four maximum micro-hardnesses can reach as high as HV 76, which means that there is a 52% enhancement of the micro-hardness.

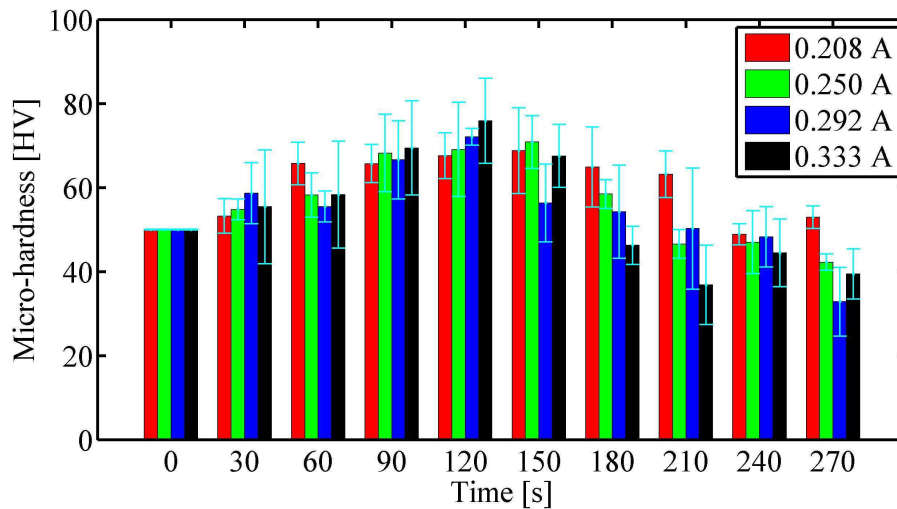


Figure 6.16: Variations of surface micro-hardness at treated conditions.

In this section, the surface properties of the aluminum alloy 5005 specimens were treated with different time and driving currents, in order to study the different phases during ultrasonic cavitation peening. The incubation period, micro-structures, roughness and micro-hardness are also investigated. Some important results are reached as follows:

Both the mass loss and the volume change increase with the increase in the process time and driving current. To precisely determine the incubation time, the volume of plastic deformation can be calculated by equation 6.1. The results can indicate the incubation period clearly. It is found that a higher driving current shortens the incubation period. There are three different phases of variations of the micro-structures during ultrasonic erosion: the plastic deformation, the generation of cracks and the grain loss. For the ultrasonic cavitation peening process, the ultrasonic cavitation on the treated surface should end before the crack generation. The increase in the process time and in driving current causes the surface roughness to increase, but the increase of surface roughness is low during the incubation period. The increase in the surface micro-hardness of the treated specimens is expected due to the fact that a hardening layer is formed during incubation period. The average micro-hardness was enhanced by 52% for the aluminum ally 5005.

7 Discussion

In Chapter 3.2, four questions were posed that will be answered in the following.

- **How do the characteristics of the sound field in a thin bubbly liquid layer depend on the consideration of bubble interactions?**

Cavitation bubbles are generated due to the vibration of the sonotrode, which leads to the variation of the vapor volume fraction in liquid. The vapor volume fraction has a great influence on the propagation of sound in liquid. When the excitation power of the ultrasound is high enough, the interactions of bubbles have to be considered. It is found that the sound speed decreases quickly if bubble interactions and the related increase of the vapor volume fraction. Based on the simulation results, the distribution of sound pressure in small gaps was calculated. Under the simulation conditions, more side lobes of the sound beam occur with higher vapor volume fraction and there is a peak value of the average sound pressure on the treated surface. The distribution of the cavitation bubbles was evaluated utilizing the sonochemiluminescence (SCL) method. The SCL relative intensity was determined by the bubble size and the bubble density. It was found that there is a peak value of the average SCL relative intensity with the increase in the vibration amplitude, which agrees well with the simulation results. The main differences between the simulation and experiments occur when the standoff distance is less than 0.4 mm. The reason is that the growths and collapses of the cavitation bubbles are limited by the small gaps.

- **How do different standoff distances and driving currents affect the impact loads and surface enhancement on the treated workpieces?**

The impact loads were evaluated utilizing the detection of the volume change and a piezoelectric force sensor, respectively. The results from these two methods show similar tendencies with different standoff distances and driving currents. Under experimental conditions, the impact load increases with the increase in the driving current. Higher driving currents introduce more energy, thus the impact effects on the treated surface become stronger.

Theoretically, the optimal standoff distance equals the diameter of the maximum bubble. When the cavitation bubbles are limited by a small gap, the collapse is different from the collapse of a spherical bubble, which leads to smaller impact on the treated surface. With a

large standoff distance, the cavitation bubbles on the treated surface become smaller due to the decrease in the sound pressure. It is found that the experimental optimal standoff distance is slightly larger than the calculated one, as the treated surface is considered to be a rigid wall in the calculated model. Sound transmission was neglected. However, the calculated results are close to the experimental results.

- **Is it possible to directly estimate plastic deformation in order to evaluate the cavitation process?**

Ultrasonic cavitation peening has the advantage of generating plastic deformation of materials. The volume change and mass loss were previously used to evaluate the cavitation process. In this thesis, a new method was developed to distinguish different phases during the ultrasonic cavitation process. The plastic deformation can be calculated by the volume change and mass loss. Thus, by analyzing the variations of plastic deformation during different process times, the different phases can be easily recognized. From the initial stage to the end of the incubation period, the plastic deformation increases constantly. When the incubation period ends, the plastic deformation rate trends to be zero, which means that there is no more plastic deformation.

- **How do the surface properties change depending on the parameters of ultrasonic cavitation peening?**

The micro-structure changes with the increase in the process time. Initially, the plastic deformation occurs on the treated surface. With the increase in the number of impacts, some cracks are generated on the surface due to dislocations of grains. However, the grains still remain on the specimen surface. The grains are finally pulled out which leads to mass loss and decrease in the surface hardness. Thus, the moment before the cracks are generated on the surface is a desired process time for ultrasonic cavitation peening. In general, at the end of the incubation period, the surface hardness reaches its maximum value and the surface roughness is small.

- **Conclusion**

All the open questions which were formulated in Chapter 3 have been answered in this thesis. A model taking the interactions of cavitation bubbles into consideration was first built to calculate the sound field distribution in a liquid. SCL experiments were then carried out to valid the model. The impact loads in small gaps were studied experimentally and theoretically for the first time as well. Finally, a more precise method, the plastic deformation method, was used to recognize the different phases of ultrasonic cavitation process.

8 Conclusions and outlook

8.1 Conclusions

Ultrasonic cavitation is widely used in many industrial applications. As one of the novel applications, ultrasonic cavitation peening has the advantages of ultrasonic technology: it is easy to control, has compact structures as well as a high output power. During this process, cavitation bubbles are generated in a small gap. In order to avoid energy loss, the gap width is usually less than 1 mm, which leads to cavitation characteristics which had not been studied in the past.

To obtain more violent collapses of cavitation bubbles, high vibration amplitude of the sonotrode is required. In this case, the interactions of bubbles need to be considered in the model of sound propagation in the bubbly liquid. Compared to the model without bubble interactions, the sound speed in the case of bubble interaction is smaller. Then the sound distribution in the small gap and on the rigid wall was calculated. It was found that, under the simulation conditions, there is a peak value of the average sound pressure on the treated surface with increasing the driving current. The local sound pressure distribution on the treated surface is analyzed as well. The results show that the highest sound pressure is generally in the central area. Sometimes the ring regions occur. Additionally, the sound pressure on the rigid wall also decreases with an increasing standoff distance.

The distribution of cavitation bubbles corresponds to the distribution of sound pressure. The Sonochemiluminescence (SCL) experiments were carried out to validate the calculation results. The variations of the SCL relative intensity in different operating conditions show a similar tendency to the simulation results at a large standoff distance. However, with small standoff distances, the SCL relative intensity decreases with the decrease in the standoff distance. This is because the growth and collapses of the cavitation bubbles are limited by the small gap.

The impact loads on the treated surfaces play an important role during ultrasonic cavitation peening, since the surface properties depend on the characteristics of the impacts on the treated surface. Generally, there are three different bubble forms in a small gap. According to previous studies, it can be deduced that the optimal standoff distance should equal the maximum bubble diameter. From the model of sound pressure distribution, the energy and micro-jets on the treated surface can be calculated at the optimal standoff

distance.

In order to validate the calculated results, the surface volume changes under different treatment conditions were measured. It was shown that the experimental optimal standoff distance is slightly larger than the calculated optimal standoff distance. Due to the pits caused by cavitation bubbles, the distribution of cavitation bubbles is greatly affected. The volume change cannot obtain the impact loads in real time on the treated surface. Thus, a piezoelectric sensor with a titanium covered surface which was designed by myself was utilized to measure the impact loads. The number of impact peaks was counted and analyzed under different treatment conditions. The power spectrum was also analyzed. It was found that stronger impacts are obtained at higher driving current and in the range of standoff distance from 0.6 mm to 0.8 mm. Finally, the working efficiency was studied. Due to the higher attenuation caused by a higher driving current, the efficiency at a higher driving current is lower than that at a smaller driving current.

To identify the different phases during ultrasonic cavitation peening, the aluminum alloy 5005 specimens were treated with an ultrasound frequency at about 23 kHz. The difference of mass loss and volume change before and after treatment was measured. Both increase as the driving current and the process time increase. From the measurement results, the plastic deformation was deduced. The results show that a higher driving current leads to a higher plastic deformation rate on the treated specimens and shortens the incubation period. The micro-structures are studied as well. It is deduced that there are three different phases: the plastic deformation, the generation of cracks and the grain loss. The ultrasonic cavitation on the treated surface should end before the crack generation starts. The roughness increases with an increase in the process time. Higher driving currents cause higher surface roughness but the surface roughness is compared to low during incubation period. The maximum micro-hardness is achieved at the end of the incubation period. The average micro-hardness of the four maximum hardnesses spans from HV 50 to HV 76, which represents an increase of 52%. The increase in surface micro-hardness of the treated specimens is due to the fact that a hardening layer is formed during the incubation period. After the incubation period, considerable erosion occurs on the treated surface, which results in the degradation of the surface properties. Therefore, the surface micro-hardness decreases with the increase in the process time.

The investigations in this thesis show the high potential of ultrasonic cavitation peening. With the achieved results, the process parameters can be chosen in an optimal way so that the beneficial properties of this process can be used for surface treatments without the disadvantage of substantial energy loss and much surface erosion.

8.2 Outlook

Further questions are derived from the results of this work, some of which are briefly outlined below.

Multi-bubble analysis

During cavitation peening, the standoff distances between the horn tip end and the surface of peening surface are generally less than 1 mm. The generated cavitation bubbles constitute a huge number of tiny bubbles and some bubble clusters of different sizes. These characteristics change with the variations in the standoff distance and vibration amplitude. For this analysis, a high-speed camera could be used to record the dynamics of bubbles on a treated surface. Then, the statistics and recognizing of cavitation bubbles could eventually be inducted.

Further investigation on sound field modeling

In this thesis, the bubbly liquid in the small gaps are considered to be homogeneous. However, due to the attenuation of sound wave propagation and the sound near-field effect, the distribution of the sound field is nonuniform, which leads to the inhomogeneous distribution of cavitation bubbles. Therefore, the distribution and intensity of the sound field changes with the change in the cavitation bubbles until a new stable state is achieved. In further investigations, the sound field modeling can be even more accurate taking into consideration the aforementioned conditions.

Appendix

A Measurement of hardness

In order to calculate the micro-hardness, the contact depth h_c is firstly calculated by equation A.1.

$$h_c = h_{\max} - 0.75 \frac{F_{\max}}{S} \quad (\text{A.1})$$

The projected contact area A under load is calculated using equation A.2.

$$A = 24.5h_c^2 \quad (\text{A.2})$$

The micro-hardness H is calculated by maximum indentation force and the projected contact area as shown in:

$$H = \frac{F_{\max}}{A}. \quad (\text{A.3})$$

Bibliography

- [1] A., Klumpp ; J., Hoffmeister ; V., Schulze: Mechanical Surface Treatments. In: *InProc. ICSP 16* (2014), Nr. 2, S. 12–24
- [2] GAO, Yibo ; WU, Benxin ; LIU, Ze ; ZHOU, Yun ; SHEN, Ninggang ; DING, Hongtao: Ultrasonic cavitation peening of stainless steel and nickel alloy. In: *Journal of Manufacturing Science and Engineering* 136 (2014), Nr. 1, S. 014502
- [3] BJERKNES, VFK: Fields of Force (Columbia UP, New York, 1906). In: *Google Scholar*
- [4] DORNFELD, David ; YUAN, Chris ; DIAZ, Nancy ; ZHANG, Teresa ; VIJAYARAGHAVAN, Athulan: Introduction to green manufacturing. In: *Green Manufacturing*. Springer, 2013, S. 1–23
- [5] VASU, Anoop: Influence of Curved Geometries on the Fatigue Life of Laser Peened Components. (2014)
- [6] GAO, Y-K ; YIN, Y-F ; YAO, M: Effects of shot peening on fatigue properties of 0Cr13Ni8Mo2Al steel. In: *Materials science and technology* 19 (2003), Nr. 3, S. 372–374
- [7] TOLGA BOZDANA, A: On the mechanical surface enhancement techniques in aerospace industry—a review of technology. In: *Aircraft Engineering and Aerospace Technology* 77 (2005), Nr. 4, S. 279–292
- [8] TAO, NR ; SUI, ML ; LU, J ; LUA, K: Surface nanocrystallization of iron induced by ultrasonic shot peening. In: *Nanostructured Materials* 11 (1999), Nr. 4, S. 433–440
- [9] BLEICHER, Friedrich ; LECHNER, Christoph ; HABERSOHN, Christoph ; KOZESCHNIK, Ernst ; ADJASSOHO, Beatrix ; KAMINSKI, Heinz: Mechanism of surface modification using machine hammer peening technology. In: *CIRP annals-manufacturing technology* 61 (2012), Nr. 1, S. 375–378
- [10] YANG, J-M ; HER, YC ; HAN, Nanlin ; CLAUER, Alan: Laser shock peening on fatigue behavior of 2024-T3 Al alloy with fastener holes and stopholes. In: *Materials Science and Engineering: A* 298 (2001), Nr. 1-2, S. 296–299
- [11] HASHIMOTO, Tadafumi ; OSAWA, Yusuke ; ITOH, Shinsuke ; MOCHIZUKI, Masahito ; NISHIMOTO, Kazutoshi: Long-term stability of residual stress improvement by water jet peening considering working processes. In: *Journal of pressure vessel technology* 135 (2013), Nr. 3, S. 031601

- [12] ZHAO, Fu ; BERNSTEIN, William Z. ; NAIK, Gautam ; CHENG, Gary J.: Environmental assessment of laser assisted manufacturing: case studies on laser shock peening and laser assisted turning. In: *Journal of Cleaner Production* 18 (2010), Nr. 13, S. 1311–1319
- [13] RAJESH, N ; VEERARAGHAVAN, S ; BABU, N R.: A novel approach for modelling of water jet peening. In: *International Journal of Machine Tools and Manufacture* 44 (2004), Nr. 7-8, S. 855–863
- [14] QIN, M ; JU, DY ; OBA, R: Improvement on the process capability of water cavitation peening by aeration. In: *Surface and coatings technology* 200 (2006), Nr. 18-19, S. 5364–5369
- [15] YILDIRIM, Halid C. ; MARQUIS, Gary B.: Fatigue strength improvement factors for high strength steel welded joints treated by high frequency mechanical impact. In: *International Journal of Fatigue* 44 (2012), S. 168–176
- [16] SRIRAMAN, MR ; VASUDEVAN, R: Influence of ultrasonic cavitation on surface residual stresses in AISI 304 stainless steel. In: *Journal of materials science* 33 (1998), Nr. 11, S. 2899–2904
- [17] TOH, CK: The use of ultrasonic cavitation peening to improve micro-burr-free surfaces. In: *The International Journal of Advanced Manufacturing Technology* 31 (2007), Nr. 7-8, S. 688–693
- [18] KIM, Ki-Han ; CHAHINE, Georges ; FRANC, Jean-Pierre ; KARIMI, Ayat: *Advanced experimental and numerical techniques for cavitation erosion prediction*. Bd. 106. Springer, 2014
- [19] RAYLEIGH, L: *On the pressure developed in a liquid during the collapse of a spherical cavity: Philosophical Magazine Series 6*, 34, 94–98. 1917
- [20] VOGEL, A ; LAUTERBORN, W: Acoustic transient generation by laser-produced cavitation bubbles near solid boundaries. In: *The Journal of the Acoustical Society of America* 84 (1988), Nr. 2, S. 719–731
- [21] BRENNEN, Christopher E.: *Cavitation and bubble dynamics*. Cambridge University Press, 2013
- [22] FRANC, Jean-Pierre ; MICHEL, Jean-Marie: *Fundamentals of cavitation*. Bd. 76. Springer Science & Business Media, 2006
- [23] KUTTRUFF, Heinrich: *Ultrasonics: Fundamentals and applications*. Springer Science & Business Media, 2012
- [24] PHILIPP, A ; LAUTERBORN, W: Cavitation erosion by single laser-produced bubbles. In: *Journal of Fluid Mechanics* 361 (1998), S. 75–116
- [25] NOLTINGK, B E. ; NEPPIRAS, Eo A.: Cavitation produced by ultrasonics. In: *Proceedings of the Physical Society. Section B* 63 (1950), Nr. 9, S. 674

- [26] KELLER, Joseph B. ; KOLODNER, Ignace I.: Damping of underwater explosion bubble oscillations. In: *Journal of applied physics* 27 (1956), Nr. 10, S. 1152–1161
- [27] PLESSET, Milton S. ; CHAPMAN, Richard B.: Collapse of an initially spherical vapour cavity in the neighbourhood of a solid boundary. In: *Journal of Fluid Mechanics* 47 (1971), Nr. 2, S. 283–290
- [28] HARRISON, Mark: An experimental study of single bubble cavitation noise. In: *The Journal of the Acoustical Society of America* 24 (1952), Nr. 6, S. 776–782
- [29] OHL, C-D ; PHILIPP, A ; LAUTERBORN, W: Cavitation bubble collapse studied at 20 million frames per second. In: *Annalen der Physik* 507 (1995), Nr. 1, S. 26–34
- [30] PECHA, R ; GOMPF, B: Microimplosions: cavitation collapse and shock wave emission on a nanosecond time scale. In: *Physical review letters* 84 (2000), Nr. 6, S. 1328
- [31] BRUJAN, EA ; IKEDA, T ; MATSUMOTO, Y: On the pressure of cavitation bubbles. In: *Experimental Thermal and Fluid Science* 32 (2008), Nr. 5, S. 1188–1191
- [32] GEERS, Thomas L. ; LAGUMBAY, Randy S. ; VASILYEV, Oleg V.: Acoustic-wave effects in violent bubble collapse. In: *Journal of Applied Physics* 112 (2012), Nr. 5, S. 054910
- [33] LI, Shuai ; LI, Yun-bo ; ZHANG, A-man: Numerical analysis of the bubble jet impact on a rigid wall. In: *Applied Ocean Research* 50 (2015), S. 227–236
- [34] KORNFELD, M ; SUVOROV, L: On the destructive action of cavitation. In: *Journal of Applied Physics* 15 (1944), Nr. 6, S. 495–506
- [35] NAUDE, Charl F. ; ELLIS, Albert T.: On the mechanism of cavitation damage by nonhemispherical cavities collapsing in contact with a solid boundary. In: *Journal of Basic Engineering* 83 (1961), Nr. 4, S. 648–656
- [36] BENJAMIN, T B. ; ELLIS, Ao T.: The collapse of cavitation bubbles and the pressures thereby produced against solid boundaries. In: *Philosophical Transactions for the Royal Society of London. Series A, Mathematical and Physical Sciences* (1966), S. 221–240
- [37] TZANAKIS, I ; HADFIELD, M ; HENSHAW, I: Observations of acoustically generated cavitation bubbles within typical fluids applied to a scroll expander lubrication system. In: *Experimental Thermal and Fluid Science* 35 (2011), Nr. 8, S. 1544–1554
- [38] TONG, RP ; SCHIFFERS, WP ; SHAW, SJ ; BLAKE, JR ; EMMONY, DC: The role of splashing in the collapse of a laser-generated cavity near a rigid boundary. In: *Journal of Fluid Mechanics* 380 (1999), S. 339–361
- [39] AVILA, Silvestre Roberto G. ; SONG, Chaolong ; OHL, Claus-Dieter: Fast transient microjets induced by hemispherical cavitation bubbles. In: *Journal of Fluid Mechanics* 767 (2015), S. 31–51

- [40] OBRESCHKOW, Danaïl ; TINGUELY, Marc ; DORSAZ, Nicolas ; KOBEL, Philipp ; DE BOSSET, Aurel ; FARHAT, Mohamed: Universal scaling law for jets of collapsing bubbles. In: *Physical review letters* 107 (2011), Nr. 20, S. 204501
- [41] TOMITA, Y ; SHIMA, A: Mechanisms of impulsive pressure generation and damage pit formation by bubble collapse. In: *Journal of Fluid Mechanics* 169 (1986), S. 535–564
- [42] WANG, Qianxi: Multi-oscillations of a bubble in a compressible liquid near a rigid boundary. In: *Journal of Fluid Mechanics* 745 (2014), S. 509–536
- [43] WANG, Qianxi ; LIU, Wenke ; ZHANG, AM ; SUI, Yi: Bubble dynamics in a compressible liquid in contact with a rigid boundary. In: *Interface focus* 5 (2015), Nr. 5, S. 20150048
- [44] HANSSON, I ; MORCH, KA: The dynamics of cavity clusters in ultrasonic (vibratory) cavitation erosion. In: *Journal of Applied Physics* 51 (1980), Nr. 9, S. 4651–4658
- [45] HANSSON, I ; KEDRINSKII, V ; MORCH, KA: On the dynamics of cavity clusters. In: *Journal of Physics D: Applied Physics* 15 (1982), Nr. 9, S. 1725
- [46] REISMAN, GE ; WANG, Y-C ; BRENNEN, Christopher E.: Observations of shock waves in cloud cavitation. In: *Journal of Fluid Mechanics* 355 (1998), S. 255–283
- [47] BRUJAN, Emil-Alexandru ; MATSUMOTO, Yoichiro: Shock wave emission from a hemispherical cloud of bubbles in non-Newtonian fluids. In: *Journal of Non-Newtonian Fluid Mechanics* 204 (2014), S. 32–37
- [48] BRUJAN, EA ; IKEDA, T ; YOSHINAKA, K ; MATSUMOTO, Y: The final stage of the collapse of a cloud of bubbles close to a rigid boundary. In: *Ultrasonics sonochemistry* 18 (2011), Nr. 1, S. 59–64
- [49] SHIMA, A ; SATO, Y: The behavior of a bubble between narrow parallel plates. In: *Zeitschrift für angewandte Mathematik und Physik ZAMP* 31 (1980), Nr. 6, S. 691–704
- [50] UEKI, Hiroshi ; KIMOTO, Hideo ; MOMOSE, Kazunari: Behavior of a spark-induced bubble between parallel walls. In: *Bulletin of JSME* 27 (1984), Nr. 229, S. 1358–1365
- [51] KUCHERENKO, VV ; SHAMKO, VV: Dynamics of electric-explosion cavities between two solid parallel walls. In: *Journal of Applied Mechanics and Technical Physics* 27 (1986), Nr. 1, S. 112–115
- [52] ISHIDA, Hideshi ; NUNTADUSIT, Chayut ; KIMOTO, Hideo ; NAKAGAWA, Takashi ; YAMAMOTO, Takayoshi: Cavitation bubble behavior near solid boundaries. In: <http://resolver.caltech.edu/cav2001:sessionA5.003> (2001)
- [53] ILINSKII, Yurii A. ; ZABOLOTSKAYA, Evgenia A. ; HAY, Todd A. ; HAMILTON, Mark F.: Models of cylindrical bubble pulsation. In: *The Journal of the Acoustical Society of America* 132 (2012), Nr. 3, S. 1346–1357

- [54] SEKI, Hiroki ; FUJITA, Keisuke ; OGASAWARA, Toshiyuki ; TAKAHIRA, Hiroyuki: Numerical Simulations of Growth and Collapse of a Bubble Between Two Parallel Walls. In: *ASME/JSME/KSME 2015 Joint Fluids Engineering Conference* American Society of Mechanical Engineers, 2015, S. V02AT05A004–V02AT05A004
- [55] AZAM, Fahad I. ; KARRI, Badarinath ; OHL, Siew-Wan ; KLASEBOER, Evert ; KHOO, Boo C.: Dynamics of an oscillating bubble in a narrow gap. In: *Physical Review E* 88 (2013), Nr. 4, S. 043006
- [56] XIONG, S ; TANDIONO, T ; OHL, CD ; LIU, AQ: Study of nano/micro jets generated by laser-induced bubbles in thin films. In: *Micro Electro Mechanical Systems (MEMS), 2013 IEEE 26th International Conference on IEEE*, 2013, S. 213–216
- [57] OGASAWARA, T ; TSUBOTA, N ; SEKI, H ; SHIGAKI, Y ; TAKAHIRA, H: Experimental and numerical investigations of the bubble collapse at the center between rigid walls. In: *Journal of Physics: Conference Series* Bd. 656 IOP Publishing, 2015, S. 012031
- [58] BLAKE JR, FG: Bjerknes forces in stationary sound fields. In: *The Journal of the Acoustical Society of America* 21 (1949), Nr. 5, S. 551–551
- [59] SUTKAR, Vinayak S. ; GOGATE, Parag R.: Design aspects of sonochemical reactors: techniques for understanding cavitation activity distribution and effect of operating parameters. In: *Chemical Engineering Journal* 155 (2009), Nr. 1-2, S. 26–36
- [60] FRANC, Jean-Pierre ; RIONDET, Michel ; KARIMI, Ayat ; CHAHINE, Georges L.: Impact load measurements in an erosive cavitating flow. In: *Journal of Fluids Engineering* 133 (2011), Nr. 12, S. 121301
- [61] SOYAMA, Hitoshi ; SEKINE, Yuichi ; SAITO, Kenichi: Evaluation of the enhanced cavitation impact energy using a PVDF transducer with an acrylic resin backing. In: *Measurement* 44 (2011), Nr. 7, S. 1279–1283
- [62] HATTORI, Shuji ; HIROSE, Takuya ; SUGIYAMA, Kenichi: Prediction method for cavitation erosion based on measurement of bubble collapse impact loads. In: *Wear* 269 (2010), Nr. 7-8, S. 507–514
- [63] WOLFRUM, B ; KURZ, T ; METTIN, R ; LAUTERBORN, W: Shock wave induced interaction of microbubbles and boundaries. In: *Physics of Fluids* 15 (2003), Nr. 10, S. 2916–2922
- [64] BRUJAN, Emil-Alexandru ; MATSUMOTO, Yoichiro: Collapse of micrometer-sized cavitation bubbles near a rigid boundary. In: *Microfluidics and nanofluidics* 13 (2012), Nr. 6, S. 957–966
- [65] JOHNSEN, Eric ; COLONIUS, Tim: Numerical simulations of non-spherical bubble collapse. In: *Journal of fluid mechanics* 629 (2009), S. 231–262
- [66] ROY, Samir C. ; FRANC, Jean-Pierre ; FIVEL, Marc: Cavitation erosion: using the target material as a pressure sensor. In: *Journal of Applied Physics* 118 (2015), Nr. 16, S. 164905

- [67] PRICE, Gareth J. ; HARRIS, Naomi K. ; STEWART, Alison J.: Direct observation of cavitation fields at 23 and 515 kHz. In: *Ultrasonics sonochemistry* 17 (2010), Nr. 1, S. 30–33
- [68] MERÉNYI, Gábor ; LIND, Johan ; ERIKSEN, Trygve E.: Luminol chemiluminescence: chemistry, excitation, emitter. In: *Journal of Bioluminescence and Chemiluminescence* 5 (1990), Nr. 1, S. 53–56
- [69] WEI, Zongsu ; KOSTERMAN, James A. ; XIAO, Ruiyang ; PEE, Gim-Yang ; CAI, Meiqiang ; WEAVERS, Linda K.: Designing and characterizing a multi-stepped ultrasonic horn for enhanced sonochemical performance. In: *Ultrasonics sonochemistry* 27 (2015), S. 325–333
- [70] YASUDA, Keiji ; TORII, Tatsuya ; YASUI, Kyuichi ; IIDA, Yasuo ; TUZIUTI, Toru ; NAKAMURA, Masaaki ; ASAKURA, Yoshiyuki: Enhancement of sonochemical reaction of terephthalate ion by superposition of ultrasonic fields of various frequencies. In: *Ultrasonics sonochemistry* 14 (2007), Nr. 6, S. 699–704
- [71] SUZUKI, Tomoya ; YASUI, Kyuichi ; YASUDA, Keiji ; IIDA, Yasuo ; TUZIUTI, Toru ; TORII, Tatsuya ; NAKAMURA, Masaaki: Effect of dual frequency on sonochemical reaction rates. In: *Research on chemical intermediates* 30 (2004), Nr. 7-8, S. 703–711
- [72] HATANAKA, Shin-ichi ; MITOME, Hideto ; YASUI, Kyuichi ; HAYASHI, Shigeo: Multibubble sonoluminescence enhancement by fluid flow. In: *Ultrasonics* 44 (2006), S. e435–e438
- [73] ASHOKKUMAR, Muthupandian ; MULVANEY, Paul ; GRIESER, Franz: The effect of pH on multibubble sonoluminescence from aqueous solutions containing simple organic weak acids and bases. In: *Journal of the American Chemical Society* 121 (1999), Nr. 32, S. 7355–7359
- [74] KAWAHARA, Junya ; WATANABE, Masao ; KOBAYASHI, Kazumichi: How do bubbles reduce the speed of sound in a bubbly liquid in a duct? In: *Mechanical Engineering Letters* 1 (2015), S. 15–00464
- [75] DÄHNKE, Sascha ; KEIL, Frerich J.: Modeling of three-dimensional linear pressure fields in sonochemical reactors with homogeneous and inhomogeneous density distributions of cavitation bubbles. In: *Industrial & engineering chemistry research* 37 (1998), Nr. 3, S. 848–864
- [76] COMMANDER, Kerry W. ; PROSPERETTI, Andrea: Linear pressure waves in bubbly liquids: Comparison between theory and experiments. In: *The Journal of the Acoustical Society of America* 85 (1989), Nr. 2, S. 732–746
- [77] FUSTER, Daniel ; COLONIUS, Tim: Modelling bubble clusters in compressible liquids. In: *Journal of Fluid Mechanics* 688 (2011), S. 352–389

- [78] TRONCO GASPARINI, Reynaldo ; SILVEIRA NANTES BUTTON, Vera L.: Development of a MATLAB Environment Software for Simulation of Ultrasonic Field. In: *Revista Ingeniería Biomédica* 7 (2013), Nr. 13, S. 57–67
- [79] SHCHUKIN, Dmitry G. ; SKORB, Ekaterina ; BELOVA, Valentina ; MÖHWALD, Helmut: Ultrasonic cavitation at solid surfaces. In: *Advanced Materials* 23 (2011), Nr. 17, S. 1922–1934
- [80] AHMED, SM ; HOKKIRIGAWA, K ; ITO, Y ; OBA, R: Scanning electron microscopy observation on the incubation period of vibratory cavitation erosion. In: *Wear* 142 (1991), Nr. 2, S. 303–314
- [81] ROY, Samir C.: Modeling and analysis of material behavior during cavitation erosion. In: *Diss.* (2015)
- [82] ASTM, G: 32-09: Standard test method for cavitation erosion using vibratory apparatus. In: *Annual book of ASTM standards, ASTM, Philadelphia, PA* (2009)
- [83] SHAW, SJ ; JIN, e Y. ; SCHIFFERS, WP ; EMMONY, DC: The interaction of a single laser-generated cavity in water with a solid surface. In: *The Journal of the Acoustical Society of America* 99 (1996), Nr. 5, S. 2811–2824
- [84] FRANC, Jean-Pierre: Incubation time and cavitation erosion rate of work-hardening materials. In: *Journal of Fluids Engineering* 131 (2009), Nr. 2, S. 021303
- [85] KRELLA, Alicja: Influence of cavitation intensity on X6CrNiTi18-10 stainless steel performance in the incubation period. In: *Wear* 258 (2005), Nr. 11-12, S. 1723–1731
- [86] TAKAHASHI, Norio ; KUGIMIYA, Takanori ; SEKI, Toshiyuki ; TERAOKA, Ken ; KUNOH, Takahiko ; MIZUNO, Masao: Application of Ultrasonic Cavitation to Metal Working and Surface Treatment of Mild Steel: Solid-Mechanics, Strength of Materials. In: *JSME international journal* 30 (1987), Nr. 266, S. 1229–1236
- [87] MATHIAS, M ; GÖCKE, A ; POHL, M: The residual stress, texture and surface changes in steel induced by cavitation. In: *Wear* 150 (1991), Nr. 1-2, S. 11–20
- [88] KIM, Seong-Jong ; JEONG, Jae-Yong ; LEE, Seung-Jun: Effects of temperature and amplitude on damage behavior of Al alloy by ultrasonic vibration cavitation. In: *Science of Advanced Materials* 6 (2014), Nr. 10, S. 2185–2190
- [89] HORSCH, Ch ; SCHULZE, V ; LÖHE, D: Deburring and surface conditioning of micro milled structures by micro peening and ultrasonic wet peening. In: *Microsystem technologies* 12 (2006), Nr. 7, S. 691–696
- [90] KIENZLER, A ; SCHULZE, V ; LÖHE, D: Surface conditioning by ultrasonic wet peening. In: *Conference Proceedings: ICSP-10, 2008*
- [91] SASAKI, Tomohiro ; HASEGAWA, Shun ; NAKAGAWA, Masayuki ; YOSHIDA, Sanichiro: Water Cavitation Peening by Ultrasonic Vibration for Improvement of Fatigue Strength of Stainless Steel Sheet. In: *Residual Stress, Thermomechanics & In-*

- frared Imaging, Hybrid Techniques and Inverse Problems, Volume 8.* Springer, 2014, S. 221–227
- [92] JANKA, Styková ; MILOŠ, Müller ; JAN, Hujer: The improvement of the surface hardness of stainless steel and aluminium alloy by ultrasonic cavitation peening. In: *EPJ Web of Conferences* Bd. 143 EDP Sciences, 2017, S. 02119
- [93] SOYAMA, HITOSHI: Key factors and applications of cavitation peening. In: *International Journal of Peening Science and Technology* 1 (2017), Nr. 1
- [94] JUNG, Sunghwan ; PRABHU, Murugesan ; LEE, Hyungyil: Peening the tip of a notch using ultrasonic cavitation. In: *Ultrasonics* 82 (2018), S. 322–326
- [95] JUNG, Sunghwan ; PRABHU, Murugesan ; LEE, Hyungyil: Peening narrow nozzles of reactor pressure vessels using ultrasonic cavitation. In: *Journal of Mechanical Science and Technology* 31 (2017), Nr. 11, S. 5279–5283
- [96] JAMSHIDI, Rashid ; POHL, Birte ; PEUKER, Urs A. ; BRENNER, Gunther: Numerical investigation of sonochemical reactors considering the effect of inhomogeneous bubble clouds on ultrasonic wave propagation. In: *Chemical engineering journal* 189 (2012), S. 364–375
- [97] DÄHNKE, Sascha: Modellierung sonochemischer Prozesse : Berechnung von Schallfeldern und Kavitationsblasenverteilungen. In: *Diss.* (1999)
- [98] DAHNKE, SW ; KEIL, FJ: Modeling of linear pressure fields in sonochemical reactors considering an inhomogeneous density distribution of cavitation bubbles. In: *Chemical Engineering Science* 54 (1999), Nr. 13-14, S. 2865–2872
- [99] ILLE, Igor ; TWIEFEL, Jens: Model-based feedback control of an ultrasonic transducer for ultrasonic assisted turning using a novel digital controller. In: *Physics Procedia* 70 (2015), S. 63–67
- [100] LITTMANN, Walter ; HEMSEL, Tobias ; KAUCZOR, Christopher ; WALLASCHEK, Jörg ; SINHA, M: Load-adaptive phase-controller for resonant driven piezoelectric devices. In: *World Congress Ultrasonics, Paris* Bd. 48, 2003, S. 64
- [101] TWIEFEL, Jens ; KLUBAL, Martin ; PAIZ, Carlos ; MOJRZISCH, Sebastian ; KRÜGER, Holger: Digital signal processing for an adaptive phase-locked loop controller. In: *Modeling, Signal Processing, and Control for Smart Structures 2008* Bd. 6926 International Society for Optics and Photonics, 2008, S. 69260A
- [102] HATANAKA, Shin-ichi ; YASUI, Kyuichi ; TUZIUTI, Toru ; KOZUKA, Teruyuki ; MITOME, Hideto: Quenching mechanism of multibubble sonoluminescence at excessive sound pressure. In: *Japanese Journal of Applied Physics* 40 (2001), Nr. 5S, S. 3856
- [103] HATANAKA, Shin-ichi ; YASUI, Kyuichi ; KOZUKA, Teruyuki ; TUZIUTI, Toru ; MITOME, Hideto: Influence of bubble clustering on multibubble sonoluminescence. In: *Ultrasonics* 40 (2002), Nr. 1-8, S. 655–660

- [104] BAI, Fushi ; SAALBACH, Kai-Alexander ; LONG, Yangyang ; TWIEFEL, Jens ; WALLASCHEK, Jörg: Capability evaluation of ultrasonic cavitation peening at different standoff distances. In: *Ultrasonics* 84 (2018), S. 38–44
- [105] HU, Aijun ; JIAO, Shuting ; ZHENG, Jie ; LI, Li ; FAN, Yanshu ; CHEN, Lin ; ZHANG, Zhihua: Ultrasonic frequency effect on corn starch and its cavitation. In: *LWT-Food Science and Technology* 60 (2015), Nr. 2, S. 941–947
- [106] WANG, Yi-Chun ; CHEN, Yu-Wen: Application of piezoelectric PVDF film to the measurement of impulsive forces generated by cavitation bubble collapse near a solid boundary. In: *Experimental thermal and Fluid science* 32 (2007), Nr. 2, S. 403–414
- [107] MIHATSCH, Michael S. ; SCHMIDT, Steffen J. ; ADAMS, Nikolaus A.: Cavitation erosion prediction based on analysis of flow dynamics and impact load spectra. In: *Physics of Fluids* 27 (2015), Nr. 10, S. 103302
- [108] HUMPHREY, Victor F.: Nonlinear propagation in ultrasonic fields: measurements, modelling and harmonic imaging. In: *Ultrasonics* 38 (2000), Nr. 1-8, S. 267–272
- [109] BAI, Fushi ; SAALBACH, Kai-Alexander ; WANG, Liang ; WANG, Xiaogeng ; TWIEFEL, Jens: Impact of time on ultrasonic cavitation peening via detection of surface plastic deformation. In: *Ultrasonics* 84 (2018), S. 350–355
- [110] LAPOVOK, Rimma ; MCKENZIE, PWJ ; THOMSON, PF ; SEMIATIN, SL: Processing and properties of ultrafine-grain aluminum alloy 5005 sheet. In: *Journal of materials science* 42 (2007), Nr. 5, S. 1649–1659
- [111] FATJO, Gonzalo Garcia-Atance: Surface response of ceramics subjected to erosive wear. In: *Diss.* (2010)

Curriculum Vitae

Personal data

Name	Fushi Bai
Birthday	04.05.1986
Place of birth	Gansu
Nationality	China

Career history

09/2005-06/2009	Bachelor in mechanical engineering in Sichuan University
07/2009-08/2011	Assistant engineer Changan automobile Co., Ltd
09/2011-07/2014	Master in mechanical engineering in Sichuan University
from 10/2014	Research assistant at Institute of Dynamics and Vibration Research in Leibniz University Hannover